



Technische Universität München

TUM School of Medicine and Health

***In ovo* modeling of tumor morphogenesis, stromal remodeling, and metastatic dissemination in pancreatic ductal adenocarcinoma**

Raphela Aranie Ranjan

Vollständiger Abdruck der von der TUM School of Medicine and Health der Technischen Universität München zur Erlangung eines

Doctor of Philosophy (Ph.D.)

genehmigten Dissertation.

Vorsitz: Prof. Dr. Henning Wackerhage

Betreuer: Prof. Dr. Maximilian Reichert

Prüfer der Dissertation:

1. Priv.-Doz. Dr. Roman Nawroth

2. Prof. Dr. Dieter Saur

Die Dissertation wurde am 08.01.2024 bei der TUM School of Medicine and Health der Technischen Universität München eingereicht und durch die TUM School of Medicine and Health am 13.03.2024 angenommen.

Table of contents

| | |
|---|-----------|
| 1. Introduction | 1 |
| 1.1 Pancreatic ductal adenocarcinoma | 1 |
| 1.1.1 Risk factors for PDAC | 1 |
| 1.1.2 Carcinogenesis of PDAC | 2 |
| 1.1.3 Molecular subtypes of PDAC | 4 |
| 1.1.4 Tumor microenvironment of PDAC | 6 |
| 1.1.5 Cancer-associated fibroblasts in PDAC | 7 |
| 1.2 Model systems to study PDAC | 8 |
| 1.2.1 <i>In vitro</i> models | 9 |
| 1.2.2 <i>In vivo</i> models | 10 |
| 1.2.3 Chick embryo chorioallantoic membrane model | 11 |
| 1.2.4 <i>In ovo</i> and <i>ex ovo</i> CAM models | 12 |
| 1.2.5 CAM model in cancer research | 13 |
| 2. Aims of the study | 17 |
| 3. Materials | 18 |
| 3.1 Equipments | 18 |
| 3.2 Consumables | 20 |
| 3.3 Chemicals and reagents | 23 |
| 3.4 Buffers and Solutions | 26 |
| 3.5 Antibodies | 26 |
| 3.6 Commercial kits | 27 |
| 3.7 Cell culture media and composition | 29 |
| 3.8 Cell lines and sources | 30 |
| Table 8: Cell lines used in the study | 30 |
| 3.9 Software | 31 |
| 4. Methods | 32 |

| | | |
|-------|---|----|
| 4.1 | Culture, authentication, and cryopreservation of 2D cell lines | 32 |
| 4.1.1 | Culture and authentication of 2D cell lines | 32 |
| 4.1.2 | Counting and seeding 2D cells for experiments | 32 |
| 4.1.3 | Cryopreservation and thawing of 2D cell lines | 33 |
| 4.2 | Isolation, culture, quality control, and cryopreservation of PDOs | 34 |
| 4.2.1 | Isolation of PDOs | 34 |
| 4.2.2 | Culture and expansion of PDOs | 35 |
| 4.2.3 | Quality control for <i>KRAS</i> mutation statuses of PDOs | 35 |
| 4.2.4 | Counting and seeding PDOs for experiments..... | 36 |
| 4.2.5 | Cryopreservation and thawing of PDOs..... | 37 |
| 4.2.6 | Generation of human 2D cell lines from organoids, culture, and cryopreservation..... | 37 |
| 4.3 | Test for mycoplasma contamination | 38 |
| 4.4 | Proliferation assay | 39 |
| 4.4.1 | Proliferation assay for 2D cells | 39 |
| 4.4.2 | Proliferation assay for 3D organoids..... | 40 |
| 4.5 | Scratch assay to determine <i>in vitro</i> migration potential | 40 |
| 4.6 | Imaging to morphologically characterize 2D cells and 3D organoids | 41 |
| 4.6.1 | Phase contrast microscopy imaging to morphologically characterize 2D cells and 3D organoids..... | 41 |
| 4.6.2 | Immunofluorescence staining for Phalloidin and confocal microscopy to morphologically characterize 2D cells and PDOs..... | 41 |
| 4.7 | Transcriptomic analysis..... | 42 |
| 4.7.1 | RNA isolation from murine 2D cells..... | 42 |
| 4.7.2 | RNA isolation from PDOs..... | 43 |
| 4.7.3 | Library Preparation and RNA Sequencing..... | 43 |
| 4.7.4 | RNA sequencing data analysis | 44 |

| | | |
|-----------|---|-----------|
| 4.7.5 | Molecular subtyping of murine and PDO lines | 44 |
| 4.8 | Whole exome sequencing..... | 45 |
| 4.8.1 | Genomic DNA isolation | 45 |
| 4.8.2 | Library preparation and whole-exome sequencing..... | 45 |
| 4.9 | Chick embryo chorioallantoic membrane (CAM) xenograft model experiments | 46 |
| 4.9.1 | Preparing the CAM for transplantation | 46 |
| 4.9.2 | Preparation of 2D murine PDAC cells for transplantation..... | 46 |
| 4.9.3 | Preparation of PDOs for transplantation | 47 |
| 4.9.4 | Transplantation on the CAM..... | 47 |
| 4.9.5 | Harvest of the primary tumor and chick embryo organs | 48 |
| 4.10 | Histological analysis of primary tumors..... | 48 |
| 4.10.1 | Tissue fixation and sectioning | 48 |
| 4.10.2 | Hematoxylin and eosin staining | 48 |
| 4.10.3 | Immunohistochemical staining..... | 49 |
| 4.10.4 | Immunofluorescence staining..... | 50 |
| 4.10.5 | Sirius red staining..... | 50 |
| 4.10.6 | Hyaluronan-binding protein staining..... | 51 |
| 4.11 | Species-specific qPCR to determine metastases in chick embryo organs | 52 |
| 4.11.1 | Genomic DNA isolation from chick embryo organs | 52 |
| 4.11.2 | Human-specific <i>Alu</i> qPCR to determine PDO metastasis in the chick embryo organs. | 52 |
| 4.11.3 | <i>Bl</i> qPCR to determine the metastasis of murine cells in the chick embryo organs | 53 |
| 4.12 | Statistical analysis | 54 |
| 5. | Results..... | 56 |
| 5.1 | Establishment of CAM model to study PDAC subtypes..... | 56 |
| 5.1.1 | Morphological characterization of KPC mouse-derived cell lines..... | 56 |

| | | |
|-----------|---|------------|
| 5.1.2 | Transcriptomic Characterization of KPC mouse-derived cell lines | 58 |
| 5.1.3 | Establishment of the CAM workflow using KPC mouse-derived cell lines representing distinct PDAC subtypes..... | 59 |
| 5.1.4 | Tumor take rates of KPC mouse-derived cell lines in the CAM model..... | 60 |
| 5.2 | Characterization of selected cancer hallmarks in PDAC using the CAM model | 60 |
| 5.2.1 | Characterization of the primary tumor histology of the CAM xenografts | 60 |
| 5.2.2 | Characterization of tumor proliferation of KPC mouse cell lines-derived CAM xenografts | 64 |
| 5.2.3 | Evaluation of metastatic dissemination of KPC mouse cell lines using the CAM model. | 66 |
| 5.2.4 | Characterization of the stroma in CAM xenografts..... | 69 |
| 5.3 | Establishment of CAM as a patient-derived xenograft (PDX) model..... | 78 |
| 5.3.1 | Morphological characterization of the selected PDOs | 78 |
| 5.3.2 | Mutation profile of the PDOs..... | 81 |
| 5.3.3 | Transcriptomic characterization of the PDO lines | 82 |
| 5.3.4 | Establishment of the CAM workflow as an alternative PDX model using PDOs..... | 83 |
| 5.3.5 | Tumor take rates of PDO lines in the CAM model..... | 85 |
| 5.4 | Characterization of selected cancer hallmarks in PDAC using the CAM PDX model | 86 |
| 5.4.1 | Characterization of primary tumor histology of PDOs-derived CAM xenografts | 86 |
| 5.4.2 | Characterization of tumor proliferation in PDOs-derived CAM xenografts | 89 |
| 5.4.3 | Evaluation of metastatic dissemination of the PDOs using the CAM model..... | 91 |
| 5.4.4 | Characterization of the stroma in CAM xenografts..... | 95 |
| 6. | Discussion..... | 103 |
| 6.1 | Establishment of the CAM model and the workflow | 104 |
| 6.2 | Characterization of selected cancer hallmarks in PDAC using the endogenous mouse cells-derived CAM model..... | 105 |

| | | |
|------------|---|------------|
| 6.3 | Characterization of selected cancer hallmarks in PDAC using the CAM PDX model | 109 |
| 7. | Conclusion and Future Perspectives..... | 113 |
| 8. | Acknowledgment | 114 |
| | Publications, presentations, and awards | 115 |
| 8.1 | Publications | 115 |
| 8.2 | Oral presentations..... | 115 |
| 8.3 | Poster presentations..... | 115 |
| 8.4 | Awards..... | 116 |
| 9. | List of figures | 117 |
| 10. | List of tables | 119 |
| 11. | References | 120 |

Abbreviations

| | |
|--------------------|---|
| °C | Degree Celsius |
| 2D | Two-dimensional |
| 3D | Three-dimensional |
| α-SMA | Alpha-smooth muscle actin |
| ADEX | Aberrantly differentiated endocrine exocrine |
| ATP | Adenosine triphosphate |
| BPE | Bovine pituitary extract |
| BSA | Bovine serum albumin |
| CAF | Cancer-associated fibroblasts |
| CAM | Chick embryo chorioallantoic membrane |
| <i>CDH10</i> | Cadherin-10 |
| <i>CDKN2A</i> | Cyclin-dependent kinase inhibitor 2A |
| cDNA | Complementary deoxyribonucleic acid |
| CK19 | Cytokeratin 19 |
| | Clustered regularly interspaced short palindromic repeats-CRISPR associated |
| CRISPR-Cas | Nuclease |
| DAB | - 3,3'-diaminobenzidine |
| ddH ₂ O | Double-distilled water |
| DMEM | Dulbecco's modified Eagle medium |
| DMSO | Dimethylsulfoxide |
| DNA | Deoxyribonucleic acid |
| PBS | Dulbecco's phosphate-buffered saline |
| ECM | Extracellular matrix |
| EDD | Embryonic development day |
| EDTA | Ethylenediaminetetraacetic acid |
| EMT | Epithelial-mesenchymal transition |
| ERK | Extracellular signal-related kinase |

| | |
|----------------|---|
| EtOH | Ethanol |
| EUS-FNAs | Endoscopic ultrasound-guided Fine Needle Aspirations |
| FBS | Fetal bovine serum |
| FFPE | Formalin-fixed paraffin-embedded |
| FGF | Fibroblast growth factor |
| FNA | Fine-needle aspiration |
| GEMM | Genetically engineered mouse models |
| GFP | Green fluorescent protein |
| <i>GLI3</i> | GLI Family Zinc Finger 3) |
| H&E | Hematoxylin/eosin |
| HIF-1 α | Hypoxia-inducible factor 1 α |
| iCAF | Inflammatory cancer-associated fibroblast |
| IF | Immunofluorescence |
| IHC | Immunohistochemistry |
| IL-6 | Interleukin 6 |
| IPMN | Intraductal papillary mucinous neoplasm |
| ITS | Insulin/human transferring/selenous acid and linoleic acid |
| KMT2D | Histone-lysine N-methyltransferase 2D |
| <i>KRAS</i> | Kirsten rat sarcoma viral oncogene homolog |
| KRT81 | Keratin 81 |
| <i>LRP1B</i> | LDL Receptor Related Protein 1B |
| MAPK | Mitogen-activated protein kinase |
| MMP | Matrix metalloproteinase |
| <i>MUC 16</i> | Mucin 16 |
| myCAF | Myofibroblastic cancer-associated fibroblast |
| mTOR | Mammalian target of rapamycin |
| MTT | 3-(4,5-dimethyl-2-thiazolyl)-2,5-diphenyl-tetrazolium bromide |

| | |
|----------------|---|
| PanIN | Pancreatic intraepithelial neoplasia |
| PBS | Phosphate-buffered saline |
| PDAC | Pancreatic ductal adenocarcinoma |
| PDO | Patient-derived organoid |
| PDGFR α | Platelet-derived growth factor receptor A |
| PDX | Patient-derived xenograft |
| PFA | Paraformaldehyde |
| PI3K | Phosphoinositide 3-kinase |
| P/S | Penicillin/streptomycin |
| PSC | Pancreatic stellate cell |
| PurIST | Purity independent subtyping of tumors |
| RNA | Ribonucleic acid |
| RNA-seq | RNA sequencing |
| RT | Room temperature |
| RT-qPCR | Real-time quantitative polymerase chain reaction |
| RPM | Revolutions per Minute |
| <i>RYR2</i> | Ryanodine receptor 2 |
| SEM | Standard error of mean |
| SMAD4 | Mothers against decapentaplegic homolog 4 |
| SPF | Specific pathogen-free |
| <i>SYNE1</i> | Spectrin Repeat Containing Nuclear Envelope Protein 1 |
| TGF- β | Transforming Growth Factor beta |
| TME | Tumor microenvironment |
| <i>TTN</i> | Titin |
| <i>TP53</i> | Tumor Protein p53 |

Abstract

Pancreatic ductal adenocarcinoma (PDAC) is expected to be the second most common cause of cancer-related death in the United States by 2040. Despite extensive progress in understanding the genetic and molecular mechanisms of the disease, clinical outcomes have not improved in the last decade, demanding the search for novel prognostic markers and therapeutic strategies. For such studies, scalable, cost-effective model systems that mimic complex tumor biology and have predictive value in the clinic are required. The chorioallantoic membrane (CAM) assay has been used as an alternative to classical *in vivo* models for several cancer types; however, it has not been well-exploited in PDAC research.

In this study, we aimed to employ the CAM assay to study PDAC biology using murine PDAC cells and patient-derived organoids (PDOs). We were able to successfully develop CAM xenografts of phenotypically diverse murine PDAC cell lines representing distinct PDAC subtypes, and, in addition, we determined conditions for PDO engraftment on CAM. Tumors were established efficiently in only 5 days, displaying a remarkable interaction with the host stroma and recapitulating the histomorphological features of parental tumors. We further characterized stromal recruitment and extracellular matrix deposition, focusing on fibrillar collagen and hyaluronan deposition, and correlated the reprogramming of the host stroma by tumor cells with metastatic dissemination. Importantly, the detection of metastases of murine cells and PDOs by species-specific DNA detection is highly reproducible and indicates heterogeneous metastatic capabilities.

In summary, this study showed that CAM is an alternative, reliable *in vivo* model to functionally study the biology of PDAC subtypes. In addition, our findings showed that CAM, as an alternative and reliable patient-derived xenograft model, provides a scalable and personalized oncology platform to functionally study PDAC tumor biology.

Zusammenfassung

Es wird erwartet, dass das duktale Adenokarzinom der Bauchspeicheldrüse (PDAC) bis 2040 die zweithäufigste krebbsbedingte Todesursache in den Vereinigten Staaten sein wird. Trotz großer Fortschritte beim Verständnis der genetischen und molekularen Mechanismen der Krankheit haben sich die klinischen Ergebnisse in den letzten zehn Jahren nicht verbessert, was die Suche nach neuen prognostischen Markern und therapeutischen Strategien erforderlich macht. Für solche Studien werden skalierbare, kosteneffiziente Modellsysteme benötigt, die die komplexe Tumorbiologie nachahmen und einen Vorhersagewert für die Klinik haben.

Der Test mit der Chorioallantoismembran (CAM) wurde als Alternative zu klassischen In-vivo-Modellen für verschiedene Krebsarten verwendet; in der PDAC-Forschung wurde er jedoch noch nicht ausreichend genutzt.

In dieser Studie wollten wir den CAM-Assay zur Untersuchung der PDAC-Biologie mit PDAC-Zellen von Mäusen und von Patienten stammenden Organoiden (PDOs) einsetzen. Wir waren in der Lage, erfolgreich CAM Xenotransplantate von phänotypisch unterschiedlichen murinen PDAC-Zelllinien zu entwickeln, die verschiedene PDAC-Subtypen repräsentieren, und wir haben darüber hinaus die Bedingungen für das PDO-Engraftment auf CAM bestimmt. Die Tumore wurden effizient in nur 5 Tagen etabliert, zeigten eine bemerkenswerte Interaktion mit dem Wirtsstroma und rekapitulierten die histomorphologischen Merkmale der Elterntumore. Wir haben die stromale Rekrutierung und die Ablagerung von extrazellulärer Matrix weiter charakterisiert, wobei wir uns auf die Ablagerung von fibrillärem Kollagen und Hyaluronsäure konzentrierten, und die Umprogrammierung des Wirtsstromas durch Tumorzellen mit der metastatischen Ausbreitung in Verbindung gebracht. Wichtig ist, dass der Nachweis von Metastasen von Mäusezellen und PDOs durch speziesspezifische DNA-Detektion sehr reproduzierbar ist und auf heterogene Metastasierungsfähigkeiten hinweist.

Zusammenfassend zeigte diese Studie, dass CAM ein alternatives, zuverlässiges In-vivo-Modell zur funktionellen Untersuchung der Biologie von PDAC-Subtypen ist. Darüber hinaus haben unsere Ergebnisse gezeigt, dass CAM als alternatives und zuverlässiges, von Patienten stammendes Xenotransplantatmodell eine skalierbare und personalisierte onkologische Plattform zur funktionellen Untersuchung der PDAC-Tumorbiologie darstellt.

1. Introduction

1.1 Pancreatic ductal adenocarcinoma

Pancreatic ductal adenocarcinoma (PDAC), a malignancy arising from the exocrine part of the pancreas, accounts for over 90% of all pancreatic cancers (McGuigan et al., 2018). The incidence of PDAC is increasing by 0.5% to 1.0% (Park et al., 2021). Even though the five-year survival rate has improved from 6% to 10% during the past five years, it is still expected to be the second most common cause of cancer-related deaths in the United States by the year 2040 (Rahib et al., 2021; Yao et al., 2020). Despite extensive efforts to understand the molecular and genetic mechanisms underlying disease progression, early diagnosis and comprehensive therapies remain elusive. Owing to the long asymptomatic phase of the disease, most patients are diagnosed at an advanced stage, with half of all patients having already developed distant metastases at diagnosis (Orth et al., 2019). Only 20% of cases are eligible for surgical resection, the only potentially curative treatment, and most cases are limited to palliative treatment options (Takikawa et al., 2022). The standard of care chemotherapy regimens, including nab-paclitaxel gemcitabine combination or FOLFIRINOX (5-fluorouracil, leucovorin, irinotecan, and oxaliplatin), offer only limited therapeutic efficacy (Digiacoia et al., 2021).

1.1.1 Risk factors for PDAC

Risk factors for PDAC are categorized as modifiable and non-modifiable. Modifiable risk factors for PDAC include obesity, alcohol consumption, and smoking (Connor et al., 2022). Obesity and diabetes not only increase the risk of PDAC but also accelerate tumor progression by inducing carbonyl stress (Menini et al., 2021). Excessive alcohol consumption is associated with a 30% increased risk of PDAC (Pang et al., 2019). Several epidemiological studies suggest that cigarette smoking leads to a faster progression of PDAC (S. Zhang et al., 2017). Well-proven non-modifiable risk factors for PDAC include age, sex, ethnicity, blood group, genetic factors, chronic pancreatitis, and diabetes mellitus. The risk for PDAC increases with age, with 71 years being the median age at which the disease is diagnosed in the US (Midha et al., 2016). Although the incidence rates among men and women differ depending on geographical location, the overall incidence of PDAC is slightly higher in men than women (Peduzzi et

al., 2022). Studies focusing on the impact of ethnicity on PDAC incidence suggest that African Americans have the highest incidence, followed by whites, Hispanics, and Asians (B. Z. Huang et al., 2019). An association between the ABO blood group and PDAC has been reported in several epidemiological studies. Individuals in blood groups A, B, and AB have a higher rate than those in the O blood group (Midha et al., 2016). At least 5-10% of patients with PDAC have a history of familial predisposition (Simoes et al., 2017). Germline mutations in *BRCA1*, *BRCA2*, *CDKN2*, *ATM*, *PRSS1*, *STK11*, *APC*, and *PALB2* are commonly observed in individuals with a hereditary risk of PDAC (Simoes et al., 2017). Additionally, inherited cancer syndromes such as Peutz-Jeghers syndrome, hereditary pancreatitis, familial atypical multiple mole melanoma syndrome, Lynch syndrome, familial adenomatous polyposis, hereditary breast and ovarian cancer syndrome, and ataxia telangiectasia impose hereditary risk for PDAC (Diaz et al., 2019). Persistent inflammation and continuous exposure to carcinogens associated with chronic pancreatitis lead to the development of PDAC (Alhobayb et al., 2021).

1.1.2 Carcinogenesis of PDAC

Two decades ago, Hruban et al. proposed a stepwise progression model for PDAC, which showed that the accumulation of genetic alterations over many years leads to a higher degree of precursor dysplasia results in PDAC (Figure 1) (Hruban et al., 2000). Several studies have identified that PDAC originates from both ductal and acinar cells as a result of similar oncogenic mutations (Ferreira et al., 2017). The expression of oncogenic *KRAS* and homozygous deletion of *Trp 53* or *Fwb7* in ductal cells lead to non-mucinous lesions and result in PDAC (Flowers et al., 2021). Acinar cells give rise to PDAC by undergoing a transdifferentiation into a duct-like phenotype in the presence of oncogenic *KRAS* mutations together with an inflammatory environment, a process known as acinar ductal metaplasia (ADM) (Li et al., 2022). ADM becomes irreversible and eventually leads to pancreatic intraepithelial neoplasia (PanIN), histologically characterized as non-invasive microscopic lesions located in the smaller pancreatic ducts (Storz, 2017). PanIN further progresses from PanIN-1 (PanIN-1A or PanIN-1B), PanIN-2, and PanIN-3, with increasing epithelial atypia, eventually leading to invasive PDAC accompanied by increased desmoplasia (Figure 1) (Pittman et al., 2017). The progression of PanIN to

PDAC is paralleled by the stepwise accumulation of genetic aberrations, such as inactivating mutations in *CDKN2A*, *TP53*, and *SMAD4* (Kleeff et al., 2016). In addition to genetic mutations, several other abnormalities, such as telomere shortening, chromosomal instability, subsequent copy number variations, chromothripsis, and epigenetic deregulation, such as aberrations in DNA methylation and histone post-translational modification, also accelerate PanIN to PDAC progression (Figure 1) (Fischer et al., 2018). Along with PanIN, there are three other types of precursor lesions that contribute to the origin and progression of PDAC: intraductal papillary mucinous neoplasia (IPMN), pancreatic mucinous cystic neoplasm (MCN), and intraductal tubular papillary neoplasm (ITPN) (Ferreira et al., 2017). A recently described punctuated evolution progression model suggests that simultaneous inactivation of PDAC driver genes results in rapid tumor development and metastatic dissemination rather than gradual progression correlating to the sudden onset of late-stage disease accompanied by metastasis (Connor & Gallinger, 2022).

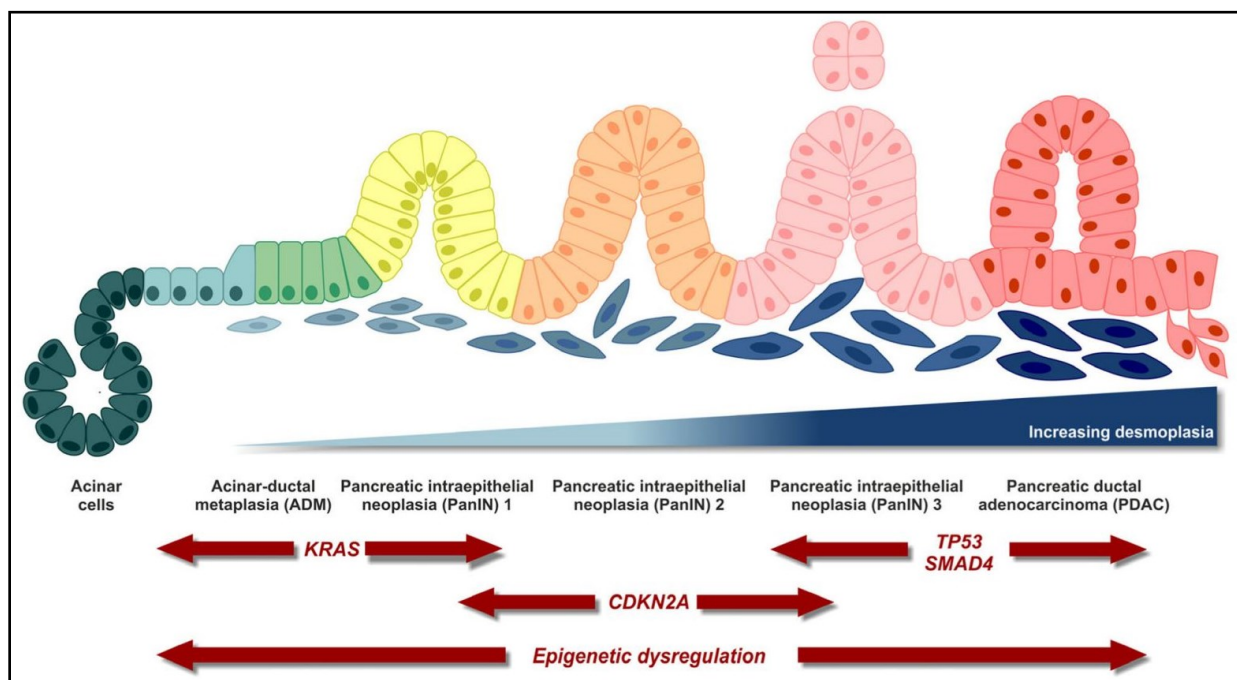


Figure 1: Stepwise progression model of PDAC.

In the presence of oncogenic *KRAS* mutations, acinar cells undergo ADM. ADM develops into three stages: PanIN, PanIN-1, PanIN-2, and PanIN-3, and finally into invasive PDAC with increased desmoplasia upon accumulation of inactivating mutations in *CDKN2A*, *TP53*, and *SMAD4*. Several other abnormalities, such as telomere shortening, chromosomal instability, subsequent copy number variations, and chromothripsis, accompany this stepwise progression of PDAC. In addition, epigenetic deregulation, such as aberrations in DNA methylation and histone post-translational modifications, also accelerates the progression of PanIN to PDAC (Orth et al., 2019).

1.1.3 Molecular subtypes of PDAC

Genomic studies suggest that PDAC progresses through a common mutational pathway involving four major genes: *KRAS*, *TP53*, *CDKN2A*, and *SMAD4*, which contradicts the clinical heterogeneity observed in PDAC patients (Pompella et al., 2020). Early attempts at clinically relevant PDAC stratification were based on a single genetic marker (Biankin et al., 2009). For example, the loss of *SMAD4* expression and overexpression of *S100A2*, associated with poor prognosis, are clinically promising and still under investigation (Biankin et al., 2009; Dreyer et al., 2020). Subsequently, structural variations in the genome were used to stratify PDAC into four subtypes: stable, locally rearranged, scattered, and unstable (Waddell et al., 2015). However, only the locally rearranged and unstable subtypes appear clinically relevant (Waddell et al., 2015). Focal amplifications in *ERBB2*, *MET*, *CDK6*, *PIK3CA*, and *PIK3R3* in locally rearranged subtypes can be therapeutically targeted (Waddell et al., 2015). The unstable subtype is potentially susceptible to therapeutics, such as platinum and poly (ADP-ribose) polymerase (PARP) inhibitors, due to defects in the DNA damage response (Waddell et al., 2015).

Recent genomic and transcriptomic studies have stratified PDAC into clinically relevant molecular subtypes to guide clinical decisions. Based on transcriptomic analysis, Collisson et al. first defined three PDAC subtypes: classical, quasi-mesenchymal, and exocrine-like (Collisson et al., 2011). Tumors with higher expression of adhesion-associated and epithelial genes and a higher expression of *KRAS* and *GATA6* are characterized as classical subtypes. The quasi-mesenchymal subtype shows higher expression of mesenchyme-associated genes, whereas the exocrine-like subtype is associated with a higher expression of tumor cell-derived digestive enzyme genes (Collisson et al., 2011). They further demonstrated the high tumor grade and poor survival associated with the quasi-mesenchymal subtype compared with the other two subtypes (Collisson et al., 2011). Regarding therapeutic relevance, the quasi-mesenchymal subtype is highly sensitive to gemcitabine, whereas the classical subtype is more sensitive to erlotinib (Collisson et al., 2011).

By virtual microdissection of PDAC gene expression microarray data from primary tumor, metastatic, and normal samples, Moffitt et al. stratified PDAC into tumor-specific subtypes, namely basal-like, classical, and stroma-specific subtypes, namely normal and activated. The basal-like subtype is

associated with poor clinical outcomes but is more sensitive to adjuvant therapy than the classical subtype. The classical subtype, along with activated stroma, is associated with worse survival compared to that with normal stroma. In contrast, survival in the basal-like subtype is not influenced by the stromal subtypes (Moffitt et al., 2015). Bailey et al. stratified PDAC into four subtypes with significantly different prognoses: squamous, associated with poor prognosis, immunogenicity, pancreatic progenitor, and aberrantly differentiated exocrine (ADEX) (Bailey et al., 2016). Bailey's classification is based on the clustering of transcriptomic data from PDAC samples of different histopathological subtypes with more than 40% tumor cellularity to balance stromal gene expression (Bailey et al., 2016). However, classical subtypes by Collisson and Moffitt overlap with the pancreatic progenitor subtypes by Bailey (Torres et al., 2018). Likewise, there is a significant overlap between the Collisson quasi-mesenchymal, Moffitt basal, and Bailey squamous subtypes and the Collisson exocrine-like and Bailey ADEX subtypes (Torres & Grippo, 2018).

By integrating genomic, transcriptomic, and proteomic profiling of 150 PDAC samples, including those with low tumor cellularity, The Cancer Genome Atlas (TCGA) consortium reproduced the classical and basal-like classification. It showed that the immunogenic, exocrine, and ADEX subtypes are associated with low tumor cellularity samples reflecting gene expression from non-tumor cells (Cancer Genome Atlas Research Network. Electronic address et al., 2017). Puleo et al. proposed two classification systems based on the genomic profiling of 300 formalin-fixed paraffin-embedded PDAC samples (Puleo et al., 2018). Transcriptomic analysis exclusively in samples with high cellularity identified two subtypes, classical and basal-like, which overlap with previous studies (Puleo et al., 2018). The classical subtype is further distinguished into immune classical and pure classical subtypes, depending on immune infiltration (Puleo et al., 2018). When samples with low cellularity were included, they identified the second classification system that stratifies the stroma into activated and desmoplastic, characterized by high expression of α SMA, SPARC, and FAP and structural and vascularized stroma components, respectively, in both classical and basal-like subtypes (Puleo et al., 2018). Recently, Chan-Seng-Yue et al. stratified PDAC into five subtypes, namely basal-like A and B, hybrid, classical A, and B, by performing whole-genome and transcriptome analysis of tumor components enriched by laser

capture from 314 primary and metastatic PDAC patients. Classical subtypes A and B show higher *GATA6* amplification and complete *SMAD4* loss, whereas basal-like A and B tumors show increased *TP53* mutations and complete *CDKN2* loss. Although the basal-like subtype is associated with a worse prognosis and response to standard chemotherapy, patients with basal-like B and hybrid subtypes present with resectable disease. Importantly, this study highlights intra-tumoral molecular heterogeneity by showing the co-existence of basal-like and classical subtypes in the same tumor (Chan-Seng-Yue et al., 2020).

1.1.4 Tumor microenvironment of PDAC

Pronounced tumor microenvironment (TME), which makes up 90% of the tumor tissue, is a histological hallmark of PDAC (Hessmann et al., 2020). The TME of PDAC is a diverse and complex milieu of cellular and acellular components (K. Wang et al., 2020). The cellular components of PDAC TME are immune cells, cancer-associated fibroblasts (CAFs), endothelial cells, and neurons (Hosein et al., 2020). Myeloid cells, such as macrophages and neutrophils, are the most abundant cell types in the PDAC TME, whereas only 2% of the cellular compartment comprises CAFs (Sperb et al., 2020). The acellular components of TME include the extracellular matrix (ECM) components, cytokines, chemokines, and growth factors produced by the constant communication between the cancer cells and stromal cells (Truong et al., 2021), which in turn orchestrate a complex signaling network to facilitate the tumor stroma cross talk (Truong & Pauklin, 2021). The constant communication of tumor cells with the TME sculpts the molecular identity of the tumor as well as the clinical outcome (Herting et al., 2021).

Early studies suggested that TME solely promotes PDAC progression by creating a physical barrier around the tumor cells, resulting in hypovascularization that subsequently leads to the limited exposure of the tumor cells to chemotherapeutics and poor immune cell infiltration (Hessmann et al., 2020). However, on the contrary, recent studies suggest TME exerts protective effects as well (Ando et al., 2022). Evidently, Ozdemir et al. and Rhim et al. found that complete depletion of stroma leads to more aggressive tumors with decreased overall survival (Ozdemir et al., 2014; Rhim et al., 2014). Thus, TME is not just a static entity, and its composition and functional role are constantly changing depending on the tumor stage and variables for different components of TME (Ho et al., 2020).

1.1.5 Cancer-associated fibroblasts in PDAC

CAFs are one of the most abundant and active components of the PDAC TME and mainly produce the desmoplastic stroma, which modulates the disease progression and treatment response in PDAC (Sperb et al., 2020). CAFs are heterogeneous regarding origins, molecular characteristics, spatial confinement, and functions (Vaish et al., 2021). CAFs originate from a diverse range of stromal cell progenitors, including pancreatic stellate cells (PSCs), mesenchymal stem cells (MSCs), bone marrow-derived mesenchymal stem cells (BD-MSCs), and quiescent resident fibroblasts, through multiple pathways of activation such as sonic hedgehog (SHH), TGF- β , TNF- α , and interleukins 1, 6, and 10 (von Ahrens et al., 2017).

CAFs exhibit diverse functions that could either promote or limit tumor growth (T. Zhang et al., 2022). These multidirectional roles of CAFs are reflected in the contradicting results of multiple preclinical and clinical studies in which some reported tumor suppressive effects. In contrast, others reported reduced patient survival upon CAF depletion (Ozdemir et al., 2014). These contradicting observations suggest the existence of a heterogeneous population of CAFs. Öhlund et al. reported that CAFs in PDAC exhibit either a myofibroblast (myCAF) or an inflammatory (iCAF) phenotype (Ohlund et al., 2017). In addition to pan-CAF markers such as COL1A1/2 (collagen I alpha 1/2), DCN (decorin), PDPN (podoplanin), FAP (fibroblast activation protein), and VIM (vimentin), myCAFs show high expression of alpha-smooth muscle actin (α -SMA) and low expression of interleukin-6 (IL-6) and other inflammatory interleukins such as IL-11 and LIF (leukemia inhibitory factor) (Murphy et al., 2021). Meanwhile, iCAFs exhibit lower expression of α -SMA and high expression of IL-6, IL-11, and LIF (Wandmacher et al., 2021). MyCAFs are mainly involved in producing ECM components such as different types of collagen, glycoproteins, proteoglycans, and hyaluronic acid (HA) (Vaish et al., 2021). iCAFs produce the inflammatory cytokines LIF and IL-6 in response to paracrine signals from tumor cells and promote immune evasion, as well as chemo-resistance, leading to poor clinical outcomes (Shinkawa et al., 2022). By single-cell RNA sequencing (scRNA seq) of both murine and human PDAC tumors, Elyada et al. recently identified a new CAF subpopulation, namely antigen-presenting CAFs (apCAFs), expressing genes associated with the MHC class II family, including H2-Aa, and H2-Ab1, and CD25, as well as

various pro-tumorigenic and pro-inflammatory genes such as SAA3 (serum amyloid A3) and SLPI (secretory leukocyte protease inhibitor) (Elyada et al., 2019). apCAFs activate CD4⁺ T cells through MHC class II and the CD74 variant chain (Elyada et al., 2019). The absence of co-stimulatory molecules such as CD80, CD86, and CD40 indicates their inability to function as classical antigen-presenting cells (Elyada et al., 2019). The tumor suppressive role of apCAFs by inducing regulatory T cells (Tregs) has been reported recently (H. Huang et al., 2022). Apart from functional differences, these CAF subpopulations, especially myCAFs and iCAFs, also exhibit spatial distinctions, where the former is located close to the tumor cells and the latter is located far away from the tumor cells (Ohlund et al., 2017). CAFs switch their phenotypes in the presence of specific spatial or biochemical cues, indicating their high degree of plasticity (Boyd et al., 2022). For example, TGF- β converts iCAF into the myCAF phenotype by reducing the expression of IL-1 via JAK/STAT pathway antagonism (Biffi et al., 2019). Also, it has been shown that by changing the culture conditions, apCAFs could be converted to myCAFs (Sperb et al., 2020). The interaction of CAFs with tumor cells and other components of the TME is very dynamic and complex due to the heterogeneous and plastic nature of CAFs (Feldmann et al., 2021). Therefore, understanding the transcriptional and microenvironmental drivers that influence the CAF phenotype and their functional role in all stages of PDAC tumorigenesis might pave the way for effective stroma remodeling therapies to increase the clinical outcome.

1.2 Model systems to study PDAC

The availability of different experimental model systems, ranging from *in vitro* to *in vivo* models, helps to understand the genetic and molecular mechanisms of PDAC and to review the molecular and therapeutic aspects of PDAC. Various *in vitro* and *in vivo* models have been used to model PDAC. *In vitro* models include two-dimensional (2D) cell culture and three-dimensional (3D) organoid culture systems, whereas *in vivo* models include genetically engineered mouse models (GEMMs) and xenograft models.

1.2.1 *In vitro* models

In vitro models, including human and murine 2D cell lines, have contributed to many PDAC studies. Cell culture models are cost and time-efficient, easy to maintain and manipulate, and highly reproducible. In addition, 2D cells can be implanted into immunodeficient mouse models to develop xenograft models. As they can be easily cultured in large quantities, they are useful in large-scale genetic screens. Due to the loss of genetic heterogeneity and genetic and phenotypic drift in 2D cell culture models, they fail to recapitulate the primary tumor (Garcia et al., 2020). In addition, 2D cell lines have limited potential to evaluate therapeutic efficacy due to the lack of a TME component, which fails to recapitulate the complexity of the PDAC (Suri et al., 2020).

In contrast to monolayer 2D cell culture models, 3D models are grown in liquid, embedded in or on a matrix, mainly Matrigel and collagen, or by using a microfluidic platform to mimic the 3D architecture of the primary tumor. Established 2D cell lines embedded in collagen or Matrigel self-organize to generate spheroids that mimic cell-cell, cell-microenvironment, and cell-matrix interactions observed *in vivo* (Gundel et al., 2021). Compared to 2D models, spheroids preserve tumor cell interactions and polarity, thereby recapitulating the primary tumor. Since spheroids are generated from 2D cell lines, their clinical relevance is limited by concerns over the drawbacks of 2D cell lines. Organoids are a popular 3D model system derived from embryonic stem cells, induced pluripotent stem cells, somatic stem cells, or tumor cells. Unlike spheroids, which are developed from established cell lines, organoids are developed from primary cells. Organoids resemble the molecular features of the original tumor since they preserve the tumor heterogeneity and cell polarity and interact with the ECM (Miquel et al., 2021; Randriamanantsoa et al., 2022). Upon orthotopic transplantation in mice, organoids can mimic the PDAC progression from PanIN to invasive adenocarcinoma (Yao et al., 2020). Like 2D models, the organoid model system is amenable to various biochemical and drug screens. Several studies have shown that the molecular and therapeutic profiling of PDOs enables the prediction of clinical outcomes in a personalized manner (Tiriach et al., 2018; Vlachogiannis et al., 2018). Due to the lack of vasculature and immune microenvironment, organoids fail to fully replicate the human PDAC (Xu et al., 2022). Although 3D *in vitro* models provide an artificial extracellular matrix (ECM) to mimic the TME, an

issue that is often faced when using standard 3D models is that they create false interactions between the cells and their matrix or they have an overly simplistic model of a tumor (Barbosa et al., 2021). Hence, *in vitro* experimental models have reduced physiological relevance and do not recapitulate human cancers; *in vivo* models are of choice to study the complexity of cancer.

1.2.2 *In vivo* models

Genetically engineered mouse models (GEMMs) are the most commonly used *in vivo* models that have provided a powerful tool to model PDAC by developing tumors that recapitulate the human PDAC. KC mice were the first GEMMs developed using the Cre/LoxP strategy to express *KRAS*^{G12D} conditionally in pancreatic progenitor cells, resulting in PanINs progressing to invasive and metastatic PDAC (Hingorani et al., 2003). To overcome the long latency period associated with tumorigenesis in this model, the LSL-*KRAS*^{G12D}; LSL-Trp53^{R172H}; PDX-1-Cre (KPC) mouse models have been developed by introducing a R172H mutation in *TP53* in addition to the G12D mutation in *KRAS* (Hingorani et al., 2005). Targeting the tumor suppressor genes dysregulated in PDAC, such as *CDKN2A* and *SMAD4*, more GEMMs are developed in the mutant LSL-*KRAS*^{G12D} background to exploit the influence of these driver genes in PDAC progression (Mallya et al., 2021). Conditional loss of *CDKN2* resulted in the rapid development of PanINs, decreased tumor latency, a more undifferentiated tumor, and metastatic dissemination to the liver and lungs. In contrast, conditional loss of *SMAD4* interestingly resulted in the formation of cystic-type lesions similar to those in humans (Mallya et al., 2021). Despite the useful applications of GEMMs, their development and maintenance are labor-intensive, time-consuming, and costly, making them unsuitable for large-scale genetic or drug screens. In addition, specialized imaging techniques are required to monitor the tumor progression (Yu et al., 2021). In addition to GEMMs, several xenografts have been developed to study PDAC. Xenograft models are developed by orthotopically or heterotopically implanting 2D cell lines, organoids, and patient-derived tissues from primary tumor biopsy or resection in immunodeficient mice (Bleijns et al., 2019). Compared to *in vitro* models, xenograft models mimic the disease complexity better, making them suitable for evaluating the efficacy of pharmacological interventions (C. F. Wang et al., 2019). Xenografts could be either cell line-derived (CDX) or patient-derived (PDX), where the former has the same limitations associated with its

2D cell lines of origin, such as loss of tumor heterogeneity and genetic drift, resulting in poor correlation with the primary tumor histology (Garcia et al., 2020).

On the other hand, PDX models better recapitulate human PDAC since it is derived from directly implanting the tissue from a primary tumor (Pion et al., 2022). Hence, PDX models are more efficient in personalized medicine. However, PDX models are usually resource-intensive since they require a significant amount of starting tissue (Pham et al., 2021). Immunodeficient mice are mostly used for PDX development, which is labor-intensive and time-consuming (Goto, 2020). Most of the time, this timeline makes precision medicine studies unrealistic since the goal is to evaluate therapeutic efficacy in real time to assist in clinical decision-making.

Due to genetic and phenotypic drifts, *in vitro* 2D and 3D cell culture models cannot recapitulate the heterogeneity and complexity of PDAC (Gundel et al., 2021). The traditional *in vivo* mouse models are expensive, labor-intensive, and time-consuming. In addition, due to their complexity, there is a lack of concordance between preclinical and clinical studies of PDAC (Ehlen et al., 2020). Hence, novel, cost-effective models that similarly mimic tumor biology, providing faster information on the activity of anticancer therapies, could make an important contribution to the advancement of personalized medicine.

1.2.3 Chick embryo chorioallantoic membrane model

The chick embryo chorioallantoic membrane (CAM) model is a highly vascularized extra-embryonic membrane that develops similarly to the allantois in mammals as it extends extra-embryonically from the ventral wall of the endodermal hindgut and fuses with the chorion during chick embryonic development day 4 (EDD 4) (Figure 2) (Ribatti, 2016). It consists of three layers: ectoderm arising from the chorion, fused somatic mesoderm arising from the chorion, and splanchnic mesoderm arising from the allantois (Maina, 2017). CAM has a rich vascular system with arteries, capillaries, and veins (Moreno-Jimenez et al., 2016). Until EDD 8, it develops a dense vessel system connected to the embryonic circulation and becomes fully differentiated by EDD 14 (Makanya et al., 2016). In the developing chick embryo, CAM serves as a respiratory organ by participating in gas exchange and as a waste reservoir for storing embryonic excrements (Halgrain et al., 2022; Ribatti et al., 2021). In addition,

it transports electrolytes and mobilizes calcium from the eggshell to the chick embryo to initiate bone mineralization, thereby participating in the osteogenesis of the developing chick embryo (Halgrain et al., 2022; Ribatti et al., 2021).

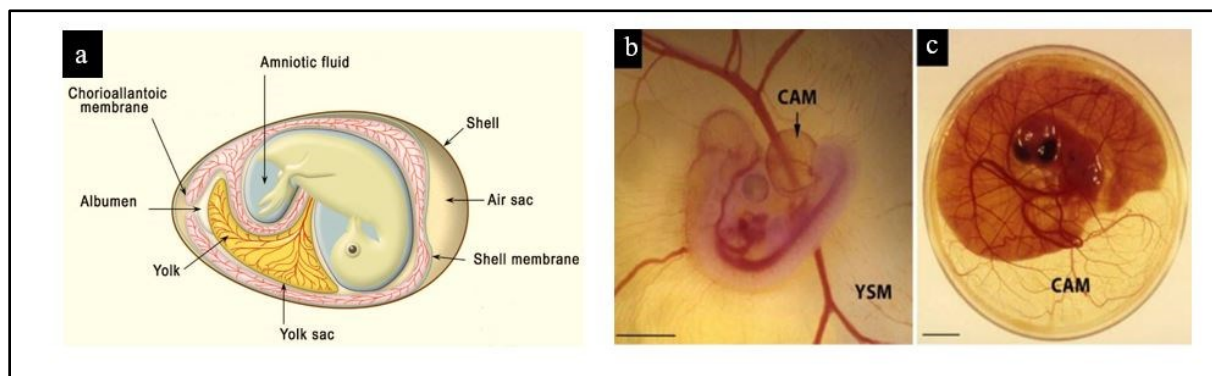


Figure 2: Formation and growth of CAM during chick embryo development.

a) Fertilized chicken egg. The shell membrane is the outermost membrane in contact with the eggshell. CAM develops extra-embryonically from the developing chick embryo and eventually covers the embryo and attaches to the shell membrane as it grows. b) Embryo at EDD 4. CAM develops in the hindgut. The yolk sac membrane (YSM) in the background is also vascularized. c) Embryo at EDD 12 in a 10 cm Petri dish. CAM is significantly larger and exceeds the area covered by the yolk (Dombre et al., 2017; Nowak-Sliwinska et al., 2014).

1.2.4 *In ovo* and *ex ovo* CAM models

The CAM model can be either *in ovo* by the dropped membrane technique or *ex ovo* (Nowak-Sliwinska et al., 2014). The *in ovo* dropped membrane technique is commonly used, in which the eggs are usually placed in an incubator that provides 65% humidity and 37 °C temperature for the development of the CAM. Embryos are left inside the eggshell during their development and for the duration of the assay. *In ovo* CAM model is initiated by making a small prick on the eggshell between EDD3 and EDD4. On EDD 7, a small window is opened on the shell. The window is then sealed, and incubation continues until the day of transplantation (Figure 3) (Ribatti, 2016). The *ex-ovo* CAM involves rupturing the egg and transferring the embryo and its extra-embryonic membranes to a petri dish or a weighing boat at EDD 3. The petri dish is sealed, and incubation continues until the day of transplantation (Figure 3). The *in ovo* approach enables experimentation through a window opened on the eggshell, and it offers an almost natural physiological environment for the developing chick embryo (Butler et al., 2022; Ribatti, 2016).

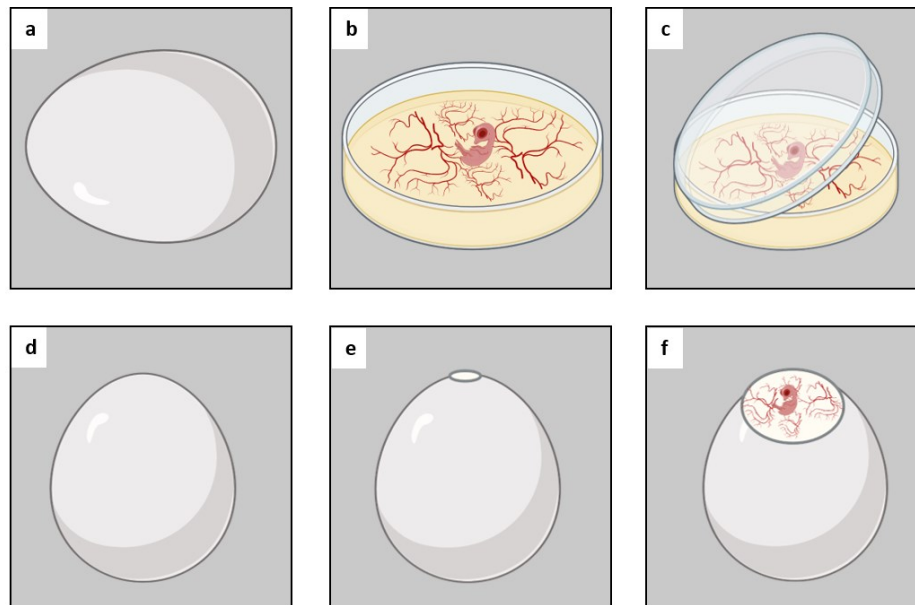


Figure 3: *In ovo* and *ex ovo* CAM models.

(a-c) The *ex ovo* CAM model. a) The eggs are gently cracked, b) The egg contents are transferred into a petri dish. c) Then, the eggs are sealed with the petri dish lid. (d-f) The *in ovo* CAM model. (d, e) A small prick is made on the eggshell. f) A window was made on the eggshell and sealed with tape.

The *ex ovo* approach offers ample observation and manipulation space, allowing the testing of several samples in a single CAM (Garcia-Gareta et al., 2020). However, the *ex ovo* method is often associated with a low survival rate due to the frequent rupture of the yolk membrane during the experiment (Naik et al., 2018).

1.2.5 CAM model in cancer research

CAM is highly vascularized and rich in type IV collagen and laminin, similar to the human basement membrane, due to which it provides an excellent natural substrate for all types of cancer cells, supporting the growth of vascularized three-dimensional tumors (Ribatti et al., 2021). Studies have reported that when solid biopsy specimens, tumor cell suspensions, or tumor cell lines are transplanted onto the CAM between EDD 6 and EDD 9, the tumors become visible and supplied with vessels of CAM origin within two to five days (Heitmeir et al., 2022; LC et al., 2018; Mapanao et al., 2021). Tumor growth on the CAM can be monitored either longitudinally by several imaging techniques such as magnetic resonance imaging (MRI), bioluminescence imaging, and ultrasonography, or by simply measuring tumor size after harvest (Eckrich et al., 2020; Javed et al., 2022; Rupp et al., 2022; Waschkes et al., 2020).

Moreover, CAM tumors can be harvested, formalin-fixed, and paraffin-embedded for histological studies (Chu et al., 2022; Ribatti et al., 2021). The histomorphology of the tumors can be easily studied using hematoxylin and eosin (H&E) staining and immunohistochemistry (IHC) (L. Chen et al., 2021; Pion et al., 2022). H&E-stained CAM xenografts allow the evaluation of the characteristics of tumor growth and proliferation, such as cell density and cellular phenotype (Chu et al., 2022; Miebach et al., 2022).

CAM has been mainly used to study tumor angiogenesis and antiangiogenic therapeutics to combat tumor progression due to its high vascularity (Merckx et al., 2020). A gelatin sponge-chorioallantoic membrane assay has been developed by directly applying the substances onto the CAM using a gelatin sponge as a carrier to study the angiogenesis-associated effects of potential therapeutic agents (Faihs et al., 2022). In the H&E-stained CAM xenografts, chick embryo vessels can be easily differentiated by their nucleated erythrocytes, due to which angiogenesis can be evaluated (LC et al., 2018). Several methods and tools have been developed to utilize the vascular network of the CAM to investigate and quantify tumor angiogenesis, such as microvascular density counts and microcomputed tomography (CT) imaging (Ames et al., 2016).

The CAM model is useful to determine either the spontaneous metastasis of cells transplanted on the CAM surface or the experimental metastasis of intravenously injected tumor cells in the chorioallantoic vein (Leupold et al., 2021). Grafted tumor cells invade through the basement membrane of the chorionic epithelium and intravasate into the vascular network in the underlying mesenchyme (Ribatti, 2016). More than 80% of the cells that intravasate into the microcirculation successfully extravasate and metastasize to distant organs of the developing chick embryo within 3-5 days of transplantation (Chu et al., 2022; Ribatti et al., 2021). By intravital imaging, the morphological changes of the cancer cells arrested in the CAM microcirculation, tumor cell motility, and migration can be observed (Pawlikowska et al., 2020). Furthermore, quantitative polymerase chain reaction (qPCR) amplification of human-specific *Alu* sequences of human tumor cells is used for semiquantitative detection of disseminating cells arrested in chick embryo organs (Ribatti et al., 2021).

CAM is advantageous over the most commonly used murine models in several aspects. The development of murine xenograft models involves mostly invasive procedures, causing pain for the animals (Moreno-Jimenez et al., 2016). The animals are subjected to pain by the growth of tumor mass, which is often associated with ulcers (Welm et al., 2021). Hence, the use of rodents to model cancer is of major ethical concern due to the pain and stress the animals have to experience (Sarogni et al., 2022). According to the 3R principle of the ethical guidelines regarding animal experiments, every effort must be made to replace them with non-sentient animals, to reduce the number of animals used, and to refine the animal experiments in a way that the animals experience minimum pain and distress (Doke et al., 2015). In this regard, the CAM xenograft model is preferable since it is not innervated and allows experiments that are not associated with the pain of the embryo (Ribatti, 2016).

Moreover, embryos and fetuses are not mentioned in the German Animal Rights Law (https://www.gesetze-im-internet.de/tierschg/_BJNR012770972.html). In the official gazette of the European Union 1986, Art. 2a, they are not defined as animals (<https://eur-lex.europa.eu/legal-content/DE>). According to the actual Directive 2010/63/EU of the European Parliament and the Council, experiments with avian embryos are considered “no animal” experiments until hatching (<http://data.europa.eu/eli/dir/2010/63/oj>). Since, the chick embryo’s immune system is non-functional until about two weeks of embryonic development; they are naturally immunodeficient and accept transplantation from various tissues and species without specific or nonspecific immune responses (Leupold et al., 2021). However, T cells and B cells can be first detected at EDD 11 and EDD 12, respectively. By day 18, chick embryos are completely immunocompetent, where T cells regulate antibody-mediated immunity and B cells regulate cell-mediated immunity. Another prominent advantage of the CAM model is its ease of use and low cost (Barnett et al., 2022). The egg is self-sufficient, and its normal development at 37 °C and 60-70% humidity ensures the consistent viability of the chick embryos without artificial support media or complex culture requirements (Komatsu et al., 2019). Compared to conventional rodent models, where tumor growth takes between 3 and 6 weeks, CAM is faster, in which microtumors become visible between 2 and 5 days of transplantation (Rupp et al., 2022). In contrast to standard mouse models, most cancer cells arrested in the chick embryo

microcirculation survive without significant cell damage, and a large number of them eventually complete extravasation to reach the distant organs of the developing chick embryo (Miebach et al., 2022; Rupp et al., 2022). Considering the multifaceted use of CAM due to its ability to recapitulate all the stages of tumorigenesis, including growth, TME remodeling, angiogenesis, invasion, and metastatic dissemination, it has been used as a platform for an array of molecular, biological, histopathological, and pharmacological studies of various cancer entities, including PDAC (Chu et al., 2022; Ranjan et al., 2023; Rovithi et al., 2017).

The CAM model has been developed mostly by using established cell lines such as BxPC-3 and PANC-1 to study PDAC (Fahmy et al., 2016). Long-term maintenance of these cell lines in culture is associated with phenotypic and genetic drifts. Rovithi et al. developed the CAM model to study PDAC by using primary human 2D cells, aiming to overcome the limitations associated with established cell lines (Rovithi et al., 2017). Compared to primary 2D cells, organoids better recapitulate the molecular, genetic, and therapeutic profiles of the parental tumors (Bleijs et al., 2019; Tiriach et al., 2018). Hence, combining organoid technology with CAM assays will be a novel tool to study PDAC on a personalized platform that closely resembles patient tumors.

Several transcriptomic studies have shown that PDAC can be categorized into 3 major subtypes: classical, quasi-mesenchymal, and basal-like, which are associated with clinical outcomes (Bailey et al., 2016; Chan-Seng-Yue et al., 2020; Collisson et al., 2019; Puleo et al., 2018). Though the CAM model has been used to functionally study the molecular subtypes in several other cancer entities, systematic functional characterization of PDAC subtypes has not been done using the CAM model (Chu et al., 2022; Hu et al., 2019; Ranjan et al., 2023).

Even though CAM has been used as a metastatic model in several other cancer entities, previous studies in PDAC using CAM mainly focused on the evaluation of tumor growth and proliferation (Fahmy et al., 2016; Rovithi et al., 2017). In addition to metastasis, the characterization of the stroma in CAM xenografts will enable the study of tumor-mediated stromal remodeling and its functional role in PDAC progression. Hence, the establishment of a CAM model to functionally study PDAC in a personalized manner will be a great addition to existing model systems that help to understand disease progression.

2. Aims of the study

CAM has been used as a reliable *in vivo* model to study several cancers due to its advantages, such as time and cost efficiency and scalability. However, it has not been well exploited to model PDAC. Hence, the major aim of the project was to establish CAM as a reliable model to study PDAC and its complex biology. Considering the PDAC subtypes and clinical outcomes associated with them, our first aim was to establish the CAM model to study distinct subtypes of PDAC. For this purpose, transcriptomically characterized endogenous murine cell lines representing classical, quasi-mesenchymal, and basal-like PDAC subtypes were transplanted on CAM. In addition, we aimed to combine patient-derived organoid (PDO) technology with the CAM assay to establish a patient-derived xenograft (PDX) CAM model. For this purpose, transcriptomically subtyped PDOs were transplanted onto the CAM.

After the successful establishment of the CAM model using murine cells and PDOs, we aimed to perform functional characterization of important cancer hallmarks such as tumor proliferation and metastatic dissemination for each PDAC subtype. In addition, by using the CAM PDX model, we aimed to evaluate the tumorigenic and metastatic potential of the PDOs *in vivo*.

Further, we aimed to use the CAM model to study tumor cell-mediated stromal recruitment and remodeling, focusing mainly on the CAFs, a functionally prominent cellular component of the tumor microenvironment. For this purpose, we characterized tumor cell-mediated CAF recruitment in murine cells and PDO-derived CAM xenografts. In addition, we aimed to investigate tumor cell-mediated stromal remodeling, focusing on major ECM components of the desmoplastic stroma such as fibrillar collagen and hyaluronan, produced mainly by myCAF, and their functional roles in PDAC progression using the CAM model.

3. Materials

3.1 Equipments

Table 1: Equipments used in the study

| Equipments | Manufacturer |
|--|--|
| Analytical balance A 1200 S | Sartorius AG, Göttingen |
| Analytical balance BP 610 | Sartorius AG, Göttingen |
| Autoclave 2540 EL | Tuttnauer Europe B.V., Breda, The Netherlands |
| Biometra Compact Agarose Gel Electrophoresis | Analytik Jena, Jena |
| Centrifuge Avanti® J25 | Beckman Coulter GmbH, Krefeld |
| Centrifuge Rotina 46R | Andreas Hettich GmbH & Co. KG, Tuttlingen |
| Centrifuge Rotina 380 | Andreas Hettich GmbH & Co. KG, Tuttlingen |
| CO2 incubator, HERA cell 240 | Thermo Fisher Scientific, Inc., Waltham, MA, USA |
| Dissection equipments | ChiroMed, Grosshändler in Hirschaid, Bayern, Germany |
| Electrophoresis Power Supply Model 100/500 | Bio-Rad Laboratories GmbH, Munich |
| Electrophoresis Power Supply Model | Model Life Technologies, Waltham, MA, USA |
| Electrophoresis power supply Power Pac 200 | Bio-Rad Laboratories GmbH, Munich |
| FLUOstar OPTIMA microplate reader | BMG Labtech GmbH, Ortenberg |
| Gel Doc™ XR+ system | Bio-Rad Laboratories GmbH, Munich |
| Gentle MACS™ Dissociator | Miltenyi Biotec B.V. & Co. KG, Bergisch Gladbach |

| | |
|---|--|
| Glassware, Schott Duran® | Schott AG, Mainz |
| HERAsafe® biological safety cabinet | Thermo Fisher Scientific, Inc., Waltham, MA, USA |
| HERA THERM incubator | Thermo Scientific, Waltham, USA |
| Ice machine AF 20 | Scotsman, Milan, Italy |
| Incubator shaker Thermoshake | C. Gerhardt GmbH & Co. KG, Königswinter |
| KnF LABOPORT® series laboratory vacuum pump | KnF Neuberger, Trenton (NJ), USA |
| Laminar flow type: HS 18/2 | Heraeus Instruments, Hanau |
| Leica TCS SP8 Confocal Microscope | Leica, Wetzlar |
| Magnetic stirrer, Ikamag® RCT | IKA® Werke GmbH & Co. KG, Staufen |
| Microcentrifuge 5415 D | Eppendorf AG, Hamburg |
| Microcentrifuge 5417 R | Eppendorf AG, Hamburg |
| Microwave | Siemens AG, Munich |
| Minicentrifuge MCF-2360 | LMS Consult GmbH & Co. KG, Brigachtal |
| Multipette® stream | Eppendorf AG, Hamburg |
| Nanodrop | Thermo Fisher Scientific, Waltham, MA, USA |
| pH meter, FiveEasy | Mettler-Toledo, Greifensee, Switzerland |
| Pipettes Reference®, Research® | Eppendorf AG, Hamburg |
| Pipetus® | Hirschmann Laborgeräte GmbH & Co. KG, Eberstadt |

| | |
|-----------------------------------|--|
| Rotary Microtome Microm (HM355S) | Thermo Fisher Scientific, Inc., Waltham, MA, USA |
| Spectrophotometer NanoDrop 1000 | Thermo Fisher Scientific, Inc., Waltham, MA, USA |
| StepOnePlus™ real-time PCR system | Thermo Fisher Scientific, Inc., Waltham, MA, USA |
| Thermocycle FlexCycler | Analytik Jena, Jena |
| Vortex Genius 3 | IKA® Werke GmbH & Co. KG, Staufen |
| Water bath 1003 | GFL (Gesellschaft für Labortechnik) mbH, Burgwedel |

3.2 Consumables

Table 2: Consumables used in the study

| Consumables | Manufacturer |
|---|---|
| Cellstar Aspiration Pipette, 2 ml | Greiner Bio-One, Kremsmünster, AU |
| Cellstar cell culture flask, 75 cm ² | Greiner Bio-One, Kremsmünster, AU |
| Cell scrapers, 16 cm | Sarstedt AG & Co., Nürnbrecht |
| Cellstar Stripette, 5 ml | Greiner Bio-One, Kremsmünster, AU |
| Cellstar Stripette, 10 ml | Greiner Bio-One, Kremsmünster, AU |
| Cellstar Stripette, 25 ml | Greiner Bio-One, Kremsmünster, AU |
| Cellstar Tubes, 15 ml, 50 ml | Greiner Bio-One, Kremsmünster, AU |
| Cellulose-acetate filter | Sartorius Stedim Biotech GmbH, Göttingen, Germany |

| | |
|--|--|
| Combitips BioPur®, 0.5 mL, 1 mL, 5 mL, 10 mL | Eppendorf AG, Hamburg |
| Conical tubes, 15 mL | Greiner Bio-One GmbH, Frickenhausen |
| Conical tubes, 50 mL | Greiner Bio-One GmbH, Frickenhausen |
| Corning® Sterile 100 x 20mm Tissue Culture Dish | Corning, Inc., Costar, New York, USA |
| Coverslips | Menzel-Gläser, Braunschweig, Germany |
| CryoPure tubes | Sarstedt AG & Co., Nümbrecht |
| Disposable scalpels | Feather Safety Razor Co., Ltd., Osaka, Japan |
| EASYstrainer, 100µm | Greiner Bio-One, Kremsmünster, AU |
| Embedding cassettes | Carl Roth GmbH & Co. KG, Germany |
| Falcon Tissue Culture Plate, 24-well | Corning Inc., NY, USA |
| Filter tips: 0.1-10 µl, super slim | nerbe Plus, Winsen/Lohe, Germany |
| Filter tips: 10-100 µl | nerbe Plus, Winsen/Lohe, Germany |
| Filter tips: 100-1000 µl | nerbe Plus, Winsen/Lohe, Germany |
| Filter tips: 0-20 µl | nerbe Plus, Winsen/Lohe, Germany |
| Filter tips: 0-200 µl | nerbe Plus, Winsen/Lohe, Germany |
| Gloves Roti protect NITRIL, powder-free | Roth, Karlsruhe, Germany |
| Greiner Bio-One™ Non-Vented Polystyrene Petri Dishes | Greiner Bio-One GmbH, Deutschland |
| Gentle MACS M tubes | Miltenyi Biotec, Bergisch Gladbach, Germany |
| Ibidi µ-Slide 2 well, 8 well | Ibidi GmbH, Gräfelfing |

| | |
|---|---|
| ImmEdge® Hydrophobic Barrier PAP Pen | Vector Laboratories, Inc., USA |
| MicroAmp® optical 96-well reaction plate | Applied Biosystems, Inc., Carlsbad, CA, USA |
| MicroAmp Optical Adhesive Film | Thermo Fischer, Waltham, MA, USA |
| Micro Slides, frosted end | Assistent, Sondheim vor der Rhön |
| Parafilm® | Merck, Darmstadt |
| Pasteur pipettes | Hirschmann Laborgeräte GmbH & Co. KG, Eberstadt |
| PCR reaction tubes | Brand GmbH & Co. KG, Wertheim; Eppendorf AG, Hamburg |
| PCR plates, 96-well | Brand GmbH & Co. KG, Wertheim, Germany |
| Reaction tubes: 0.5 mL, 1.5 mL, and 2 mL | Eppendorf AG, Hamburg |
| Safe seal pipette tips, professional | Biozym Scientific GmbH, Hessisch Oldenburg |
| Safe-lock reaction tubes: BioPur® | Biozym Scientific GmbH, Hessisch Oldenburg |
| Safe-lock reaction tubes: BioPur® | Eppendorf AG, Hamburg |
| Sample beaker with screw cap | Carl Roth GmbH & Co. KG, Germany |
| Silk tape | 3M Medica Zwnl.d.3M Deutschl.GmbH |
| Single-use needles: Sterican® 27 gauge | B. Braun Melsungen AG, Melsungen |
| Single-use syringes Omnifix® | B. Braun Melsungen AG, Melsungen |
| SteriFlip Vacuum Filtration System 0.22µm | Merck Millipore, Burlington, USA |
| Tissue culture plate, 6, 12, 96 well | BD Bioscience, Heidelberg |

3.3 Chemicals and reagents

Table 3: Consumables and reagents used in the study

| Chemicals and reagents | Manufacturer |
|---|--|
| 2-Mercaptoethanol, 98% | Sigma-Aldrich Chemie GmbH, Munich |
| 2-Propanol (isopropanol) | Carl Roth GmbH & Co. |
| 3,3,5-Triiodo-L-thyronine 3-(4,5-dimethyl-2-thiazolyl)- 2,5-diphenyltetrazolium bromide (MTT) | Sigma-Aldrich Chemie GmbH, Munich |
| A83-01 | STEMCELL Technologies, Vancouver, Canada |
| Acetic Acid, 2N | Carl Roth GmbH + Co. KG, Karlsruhe |
| ACK lysis buffer | Thermo Fisher Scientific, Inc., Waltham, USA |
| Agarose | Sigma-Aldrich Chemie GmbH, Munich |
| Ammonium persulfate (APS) | Sigma-Aldrich Chemie GmbH, Munich |
| Antigen-unmasking solution | Vector Laboratories, Inc., Burlingame, USA |
| Aqua-Poly/Mounting | Polysciences Inc., Pennsylvania, USA |
| Bovine Pituitary Extract | Sigma-Aldrich Chemie GmbH, Munich |
| Bovine serum albumin, fraction V | Sigma-Aldrich Chemie GmbH, Munich |
| Cell Recovery Solution | Corning, Inc., NY, USA |
| Cholera toxin | Sigma-Aldrich Chemie GmbH, Munich |
| Collagenase Type II | Invitrogen GmbH, Karlsruhe |
| Corning® Matrigel® Growth Factor Reduced Basement Membrane Matrix | Corning, Inc., New York, USA |

| | |
|---|---|
| DAPI | Sigma-Aldrich Chemie GmbH, Munich |
| Dexamethasone | Sigma-Aldrich Chemie GmbH, Munich |
| D-Glucose | Sigma-Aldrich Chemie GmbH, Munich |
| Dimethyl sulfoxide (DMSO) | Carl Roth GmbH & Co. KG, Karlsruhe |
| Donkey serum | Biozol Diagnostica Vertrieb GmbH, Eching |
| Dulbecco's modified eagle medium (DMEM), with L-glutamine and high glucose | Invitrogen GmbH, Karlsruhe |
| DMEM low glucose | Invitrogen GmbH, Karlsruhe |
| DMEM/F-12 | Invitrogen GmbH, Karlsruhe |
| Eosin | Waldeck GmbH & Co. KG, Münster |
| Ethanol (70%, 80%, 96%, 100%) | Merck KGaA, Darmstadt |
| Fast Green FCF | Carl Roth GmbH & Co. KG, Karlsruhe |
| Fetal Bovine Serum (FBS) | Invitrogen GmbH, Karlsruhe |
| Formaldehyde Solution, 4% phosphate buffered (histology grade) | PanReac AppliChem ITW Reagents, Darmstadt, Germany |
| Glycin Pufferan® | Carl Roth GmbH & Co. KG, Karlsruhe |
| Hematoxylin | Merck KGaA, Darmstadt |
| Hydrochloric acid (HCl) | Merck KGaA, Darmstadt |
| ITS+ premix | Corning Inc., NY, USA |
| Magnesium chloride | Carl Roth GmbH & Co. KG, Karlsruhe |
| Methanol | Merck KGaA, Darmstadt |
| Milk powder | Carl Roth GmbH & Co. KG, Karlsruhe |

| | |
|---|--|
| NaOH Solution, 1N | Carl Roth GmbH & Co. KG, Karlsruhe |
| Nicotinamide | Sigma-Aldrich Chemie GmbH, Munich |
| Nuclear Fast Red | Sigma-Aldrich Chemie GmbH, Munich |
| Nu-Serum IV | Corning Inc., NY, USA |
| Penicillin/Streptomycin | Thermo Fisher Scientific, Inc., Waltham, USA |
| Pertex Mounting Media | Histolab, Askim, Norway |
| Phosphate buffered saline (PBS), powder, 1X | Sigma Aldrich, St. Louis, USA |
| Picric acid | Sigma Aldrich, St. Louis, USA |
| Primocin | InvivoGen, San Diego, USA |
| Recovery™ Cell Culture Freezing Medium | Thermo Fisher Scientific, Inc., Waltham, USA |
| RNase Zap™ | Sigma-Aldrich Chemie GmbH, Munich |
| ROCK inhibitor Y-27632 | Cayman Chemical, Ann Arbor, USA |
| Roswell Park Memorial Institute (RPMI) medium | Thermo Fisher Scientific, Inc., Waltham, USA |
| Roti® Histofix 4% | Carl Roth GmbH & Co. KG, Karlsruhe |
| Roti® Histol | Carl Roth GmbH & Co. KG, Karlsruhe |
| Sterile Water | Braun Melsungen AG, Melsungen |
| Triton® X-100 | Merck KGaA, Darmstadt |
| Trypan Blue Stain 0.4% | Invitrogen GmbH, Karlsruhe |
| Trypsin-EDTA 0.5% (10x) | Thermo Fisher Scientific, Inc., Waltham, USA |
| Tween® 20 | Carl Roth GmbH & Co. KG, Karlsruhe |

3.4 Buffers and Solutions

Table 4: Buffers and solutions used in the study

| Buffers and solutions | Composition |
|---|---|
| 1X phosphate buffered saline (PBS) | 1X pack of PBS (Sigma-Aldrich) in 1L MilliQ water 8 g of NaCl 0.2 g of KCl 1.44 g of Na ₂ HPO ₄ 0.24 g of KH ₂ PO ₄ |
| 50 x Tris acetate EDTA (TAE) buffer, pH 8.5 | 2 M Tris, 50 mM EDTA, and 5.71% Acetic Acid |
| Sirius red solution | 1.3% picric acid in H ₂ O 1 g/L Fast Green FCF 1 g/L Nuclear Fast Red |

3.5 Antibodies

Table 5: Antibodies used in the study

| Antibodies | Dilution | Catalog Number | Manufacturer |
|------------------------------------|----------|----------------|-----------------------------------|
| Alpha-smooth muscle actin antibody | 1:500 | F3777 | Sigma-Aldrich Chemie GmbH, Munich |
| Cytokeratin 19 | 1:500 | ab52625 | Abcam, Cambridge, UK |
| Hyaluronan-Binding protein | 2 µg/ml | Custom protein | R&D Systems®, Inc., USA |
| Ki67 | 1:250 | ab16667 | Abcam, Cambridge, UK |

| | | | |
|---|-------|---------|---|
| Phalloidin-Atto 647 | 1:250 | 65906 | Sigma-Aldrich Chemie GmbH, Munich |
| Vimentin | 1:200 | AMF-17b | Developmental Studies Hybridoma Bank, University of Iowa, Dept. of Biology, USA |
| Donkey anti-goat Alexa Fluor™ 488 | 1:250 | A-11055 | Thermo Fisher Scientific, Inc., Waltham, USA |
| Donkey anti-mouse Alexa Fluor™ 488 | 1:250 | A-21202 | Thermo Fisher Scientific, Inc., Waltham, USA |
| Donkey anti-rabbit Alexa Fluor™ 594 | 1:250 | A-21207 | Thermo Fisher Scientific, Inc., Waltham, USA |
| Goat anti-FITC | 1:250 | ab19224 | |
| Goat Anti-Mouse IgG Antibody (H+L), Biotinylated | 1:250 | BA-9200 | Vector Laboratories, Inc., USA |
| Goat Anti-Rabbit IgG Antibody (H+L), Biotinylated | 1:250 | BA-1000 | Vector Laboratories, Inc., USA |

3.6 Commercial kits

Table 6: Commercial kits used in the study

| Commercial kits | Catalog Number | Manufacturer |
|----------------------------|----------------|--|
| Avidin/Biotin Blocking Kit | SP-2001 | Vector Laboratories, Inc., Burlingame, CA, USA |

| | | |
|--|-------------|--|
| 3,3'-Diaminobenzidine (DAB) peroxidase substrate kit | SK-4100 | Vector Laboratories, Inc., Burlingame, CA, USA |
| CellTiter-Glo Luminescent Cell Viability Assay | G7573 | Promega GmbH, Walldorf |
| Nextera XT kit | FC-131-1096 | Illumina, San Diego, USA |
| NucleoSpin® Tissue | 740952250 | Macherey Nagel, Rue Gutenberg, Hœrdt, Frankreich |
| QIAamp® DNA Mini Kit | 56304 | Qiagen GmbH, Hilden |
| QIAshredder | 79656 | Qiagen GmbH, Hilden |
| RNase-free DNase | 79254 | Qiagen GmbH, Hilden |
| RNeasy Micro Plus Kit | 74034 | Qiagen GmbH, Hilden |
| RNeasy mini kit | 74004 | Qiagen GmbH, Hilden |
| SensiFast™ cDNA Synthesis Kit | BIO-65053 | Bioline, Meridian Life Science, Inc., USA |
| SensiFast™ SYBR® Hi-ROX Kit | BIO-92005 | Bioline, Meridian Life Science, Inc., USA |
| Vectastain® Elite ABC kit | PK-6100 | Vector Laboratories, Inc., Burlingame, CA, USA |
| Vectashield® mounting medium for fluorescence | H-1000-10 | Vector Laboratories, Inc., Burlingame, CA, USA |

3.7 Cell culture media and composition

Table 7: Cell culture media and composition used in the study

| Media | Composition |
|---------------------------------------|---|
| Digestion media for patient biopsy | DMEM/F12 with L-Glutamine and high Glucose 6 mg/mL Collagenase Type II |
| Freezing media for human tumor cells | 90% FBS 10% DMSO |
| Freezing media for murine tumor cells | 90% FBS 10% DMSO |
| Human tumor cell media | RPMI 10% FBS 1% Penicillin/Streptomycin |
| Murine tumor cell media | DMEM 10% FBS 1% Penicillin/Streptomycin |
| Patient-derived organoid media | DMEM/F12 5% Nu-Serum IV 1% Penicillin/Streptomycin 25 µg/mL of Bovine pituitary extract 0.5% ITS+ premix 100 ng/mL Cholera toxin, 5 nM 3,3,5-Triiodo-L-thyronine 1 µM Dexamethasone 5 mg/mL Glucose |

| | |
|--|--|
| | 10 mM Nicotinamide 100 µg/mL Primocin 0.5 µM A83-01 10% R-Spondin (self-produced) 100 ng/mL Neuregulin |
|--|--|

3.8 Cell lines and sources

Table 8: Cell lines used in the study

| Cell lines | Source |
|------------|--|
| 9366 | Kindly provided by Prof. Dr. Dieter Saur, Technical University of Munich, Germany |
| 12548 | Kindly provided by Prof. Dr. Dieter Saur, Technical University of Munich, Germany |
| R405 | Kindly provided by Prof. Dr. Dieter Saur, Technical University of Munich, Germany |
| B188 | Organoid core facility |
| B250 | Organoid core facility |
| B290 | Organoid core facility |
| B339 | Organoid core facility |

3.9 Software

Table 9: Software used in the study

| Software | Source |
|----------------------------------|--|
| Adobe Photoshop 7.0 | Adobe Systems Software Ireland Limited, Dublin, Ireland |
| Aperio ImageScope v12.4.3.7001 | Leica Microsystems CMS GmbH, Germany |
| Aperio VERSA v1.04.125 | Leica Microsystems CMS GmbH, Germany |
| Fiji v1.53c | National Institutes of Health, Stapleton, NY, USA |
| GraphPad Prism 9 | La Jolla, CA, USA |
| Leica Application Suite X v3.6.1 | Leica Microsystems CMS GmbH, Germany |
| Microsoft Office | Microsoft Corporation, Redmont, WA, USA |
| R Studio 4.0.02, 4.0.04 | R Studio, PBC, Boston, USA |
| StepOne™ v2.3 | Applied Biosystems, Inc., Carlsbad, CA, USA |

4. Methods

4.1 Culture, authentication, and cryopreservation of 2D cell lines

4.1.1 Culture and authentication of 2D cell lines

In this study, primary murine PDAC cell lines and patient-derived 2D cell lines were used. Primary murine PDAC cell lines were isolated and established from tumor-bearing endogenous mouse models and gifted by the group of Prof. Dr. Dieter Saur. For authentication, cells were genotyped and compared with the genotype of the endogenous murine models from which the cell lines were established. The cells were cultured in a DMEM-high glucose medium containing 10% FBS and 5% PenStrep under sterile conditions. Cell culture was performed under sterile laminar air hoods and grown in an incubator at 37 °C and 5% CO₂. Cells were replenished with a complete growth medium every two days. Upon reaching 80-90% confluency, the cells were split and further cultured. To split the confluent cells, the spent medium was aspirated, and cells were washed with 1X sterile PBS. Sterile 1X Trypsin-EDTA was added to the cells and incubated for 3-5 minutes at 37 °C and 5% CO₂. After incubation, the cells were detached, and the enzymatic activity of sterile Trypsin-EDTA was stopped by adding a complete growth medium. Detached cells were resuspended in the complete growth medium and then transferred into a sterile 15 ml falcon tube. To remove Trypsin-EDTA, the cell suspension was centrifuged at 1000 rpm for 5 minutes at 4 °C. The supernatant was discarded, and the cell pellet was resuspended in the complete growth medium. A fraction of the resuspended cells were transferred into a new tissue culture flask containing fresh medium for further subculturing according to the appropriate splitting ratio determined for each cell line. The complete growth medium was replenished every two days. The generation and culture of patient-derived 2D cell lines were described in 4.2.6.

4.1.2 Counting and seeding 2D cells for experiments

Cells were detached from the tissue culture flasks once 80-90% confluency was reached, as described above in 4.1.1. After dissociating the cells, viable cells were counted, and the required cells were seeded for experiments. The Trypan blue dye exclusion method was used to differentiate between viable and

non-viable cells. Trypan blue is a diazo dye that is negatively charged and does not interact with cells unless the cell membrane is damaged. Since the cell membrane of viable cells is intact, it excludes the trypan blue dye. In contrast, the cell membrane of a dead cell is damaged. Hence, it takes up the Trypan blue dye and is stained in a distinctive blue color that can easily be observed under a microscope. The cell pellet was diluted in a complete growth medium, and viable cells were counted using the Trypan blue dye exclusion method. The cell suspension was further diluted with Trypan blue, and from this diluted Trypan blue-cell suspension, 10 μ l was pipetted into a Neubauer counting chamber, covered with the coverslip. Viable cells in the four big corner squares of the Neubauer chamber were counted under 10X magnification using a bright field microscope. The number of cells in 1 ml of cell suspension was calculated using the following formula:

$$\text{Number of cells/ml} = \frac{\text{Total number of cells}}{4} * \text{Dilution factor} * 10^4$$

According to the experiment, the required number of cells were seeded and further cultured, as described above in 4.1.1.

4.1.3 Cryopreservation and thawing of 2D cell lines

Expanded cells at early passages were cryopreserved for future use. For cryopreservation, cells were dissociated from tissue culture flasks using 1X Trypsin-EDTA, as mentioned above. After centrifuging the cell suspension to remove trypsin, the cell pellet was resuspended in a freezing medium of FBS and DMSO in a 9:1 ratio and transferred into cryovials. Cells were frozen using a freezing container and stored at -80 °C for 1-2 days before transferring to liquid nitrogen. To thaw the cells, cryogenic vials with cell culture stocks were taken from liquid nitrogen tanks and quickly thawed in a 37 °C water bath. The cell suspension from the cryogenic vial was then transferred into a 15 ml sterile falcon containing pre-warmed complete growth medium and centrifuged at 1000 rpm for 5 minutes at RT to remove the freezing medium. After centrifugation, the supernatant was aspirated, and the cell pellet was resuspended in a fresh, complete-growth medium and transferred to a new tissue culture flask. When the cells reached 80-90% of confluency, they were subcultured as described above.

4.2 Isolation, culture, quality control, and cryopreservation of PDOs

4.2.1 Isolation of PDOs

To establish PDOs, informed written consents were given by all the patients who were enrolled in the study according to the Helsinki Declaration and approved by the local ethics committee of the Technical University of Munich, Klinikum rechts der Isar Project 207/15, 1946/07, 330/19, 181/17S, and 80/17S). Using the information system of the hospital, clinical data of the patients, such as age at the time of diagnosis, sex, tumor markers CA-19-9 and CEA, tumor formula, type of chemotherapy (neoadjuvant, adjuvant), and chemotherapeutic regime (FOLFIRINOX), were obtained. Clinical evaluation of the tumor size, lymph node status, and metastasis was performed on baseline CT before starting the treatment and in follow-up examinations.

PDOs were generated from endoscopic ultrasound-guided fine needle aspirations/biopsies (EUS-FNA/B) and surgical resections. An additional needle pass was performed to generate EUS-FNA/B samples for PDO isolation. Samples were received on ice, and the isolation process was started under sterile conditions shortly after receiving the sample.

The biopsy was transferred to a sterile Petri dish and minced into small pieces. Minced pieces of EUS-FNA/B samples were transferred to a 15 ml falcon filled with 5 ml of 1X PBS and centrifuged at 1000 rpm at 4 °C for 5 minutes. Since biopsies from surgical resections require an additional digestion step, the minced pieces were transferred to a 15 ml falcon containing 5 ml of digestion media. Digestion was performed for 1-2 hours by rotating the falcon containing the sample in digestion media using a rotating mixer. After digestion, centrifugation was done at 1000 rpm at 4 °C for 5 minutes, and the supernatant was aspirated. Followed by centrifugation, red blood cell lysis was performed for both EUS-FNA/B and surgical biopsies by incubating the tissue pellets in 2 ml of ACK lysis buffer for 3-10 minutes at RT. The supernatant was discarded, and the pellet was washed with 1X PBS by centrifuging at 1000 rpm at 4 °C for 5 minutes. Once again, the supernatant was discarded, and further digestion was performed by incubating the tissue pellets in TrypLE for 3-5 minutes at 37 °C. To neutralize the activity of TrypLE, complete RPMI media was added to the pellet and centrifuged at 1000 rpm at 4 °C for 5 minutes. The supernatant was aspirated, and the cell pellet was resuspended in Matrigel. 50 µl of Matrigel-cell

suspension was plated in each well of a 24-well plate. The number of wells for plating the PDOs was determined by the pellet size. To allow the polymerization of the Matrigel the plate was incubated at RT for 10 minutes and then at 37 °C for 10 minutes. Afterwards, 500 µl of pre-warmed PDO medium was added to each well containing the PDOs in the Matrigel dome.

4.2.2 Culture and expansion of PDOs

Once confluency was reached, PDOs were split and further expanded. To split the organoids first, the spent media was aspirated from the wells. To dissolve the Matrigel, 250 µl of ice-cold cell recovery solution was added to each well and incubated for 5 minutes on ice. To further dissolve the Matrigel dome, 1 ml of ice-cold 1X PBS was added to each well and vigorously pipetted up and down. Organoids in the dissolved Matrigel PBS mixture were then transferred to a 15 ml falcon, incubated on ice for at least 30 minutes, and centrifuged at 1000 rpm at 4 °C for 5 minutes. The supernatant was aspirated, and the cell pellet was washed with 1X cold PBS by centrifuging at 1000 rpm at 4 °C for 5 minutes. The supernatant was aspirated, and the cell pellet was resuspended in Matrigel. In each well of a 24-well plate, 50 µl of Matrigel organoid suspension was plated. The number of wells for plating the PDOs was determined according to the pellet size and splitting ratio of each PDO line. The plate was incubated at RT for 10 minutes and then at 37 °C for 10 minutes to allow the polymerization of the Matrigel. Once the Matrigel was polymerized, 500 µl of pre-warmed PDO medium was added to each well containing the PDOs in the Matrigel dome. The PDO medium was replenished twice a week.

4.2.3 Quality control for *KRAS* mutation statuses of PDOs

The *KRAS* mutation status of the PDO lines was determined by Sanger sequencing. For this purpose, DNA was isolated from the organoids. For DNA isolation, at least two confluent wells of organoids were harvested, as described above in 4.2.2. The cell pellet was resuspended in 1 ml of 1X PBS instead of Matrigel, transferred to a 1.5 ml Eppendorf tube, and centrifuged at 5000 rpm at 4 °C for 5 minutes. The supernatant was discarded, and the cell pellet was frozen at -20 °C or immediately used for DNA isolation. DNA isolation was performed using the DNA/RNA Micro Kit according to the manufacturer's

instructions. The concentration and purity of the isolated DNA were measured using a Nanodrop Spectrophotometer. To further proceed, isolated DNA was diluted to a concentration of 100 ng/ μ l, and a PCR reaction mix was prepared according to Table 10. PCR was performed according to the protocol shown in Table 11 to amplify exons on the human *KRAS* gene that contains the G12/13 codons. PCR products were purified using Machery Nagel NucleoSpin gel and a PCR clean-up kit according to the manufacturer's instructions and sent to Eurofins (Ebersberg, Germany) for Sanger sequencing. Sanger sequencing results were analyzed using Snapgene Viewer (Version 6.0.2), and the sequences were compared with the wild-type human *KRAS* gene sequence to determine mutational status.

4.2.4 Counting and seeding PDOs for experiments

PDOs were harvested from wells where 80-90% confluency was reached, as described above in 4.2.2. To isolate single cells from PDOs after washing twice with 1X PBS, the supernatant was discarded, and 1X Trypsin-EDTA was added to the cell pellet and incubated at 37 °C for 8-10 minutes, depending on the size of the pellet. Afterward, the same procedure was followed as described in 4.1.1 to neutralize the Trypsin-EDTA activity. Cells were counted and seeded for experiments as described above in 4.1.2.

Table 10: Reaction mix for human *KRAS* amplification

| Components | Volume/ reaction |
|----------------------------------|------------------|
| Q5® High-Fidelity DNA Polymerase | 25 μ l |
| 10 μ M Forward Primer | 5 μ l |
| 10 μ M Reverse Primer | 5 μ l |
| PCR water | 9 μ l |
| DNA (100 ng/ μ l) | 1 μ l |

Table 11: PCR protocol for human *KRAS* amplification

| Steps | Temperature | Time | Number of cycles |
|----------------------|-------------|--------|------------------|
| Initial denaturation | 98 °C | 3 mins | |
| Denaturation | 98 °C | 10s | X 35 |
| Annealing | 65 °C | 20s | |
| Extension | 72 °C | 15s | |
| Final extension | 72 °C | 3 mins | |

4.2.5 Cryopreservation and thawing of PDOs

Once the *KRAS* mutation status was determined, expanded organoids were cryopreserved for future use. For this purpose, organoids were harvested from confluent wells, as described in 4.2.2. The final cell pellet was resuspended in a cell recovery freezing medium. Organoids isolated from 3-4 confluent wells resuspended in 1 ml of cell recovery freezing medium were transferred to each cryovial, frozen using a freezing container, and stored at -80 °C for 1-2 days before transferring to liquid nitrogen. Cryopreserved organoids were thawed quickly in a 37 °C water bath and transferred to a 15 ml falcon containing 1X PBS. Organoids were centrifuged at 1000 rpm at RT for 5 minutes. The supernatant was aspirated, and the cell pellet was resuspended in Matrigel. Organoids were plated and further cultured as described in 4.2.2.

4.2.6 Generation of human 2D cell lines from organoids, culture, and cryopreservation

PDAC patient-derived 2D cell lines were established under the Declaration of Helsinki and were approved by the local ethical committee of the Technical University of Munich, Klinikum rechts der Isar (330/19S, 5542/12). Before the study, written consent was obtained from the patients. 2D cell lines were generated by allowing organoids to outgrow and naturally attach at the bottom of the well-containing organoids in the Matrigel dome. Once the organoids were split, the 2D cells attached to the bottom of the well were further cultured in a complete growth medium, RPMI, supplemented with 10%

FBS and 5% PenStrep. The complete growth medium was replenished every two days. Once the fibroblast contamination was lost and the well was 80-90% confluent, cells were split and further expanded as described in 4.1.1. Expanded PDAC patient-derived 2D cells were cryopreserved and thawed as described in 4.1.3. As described above in 4.1.2, cells were counted and seeded in the required amounts for experiments.

4.3 Test for mycoplasma contamination

Both 2D cells and organoids were routinely checked for mycoplasma contamination by PCR. For this purpose, 2D cells and organoids were cultured in the respective growth medium without the antibiotic PenStrep until the medium turned yellow. 2 ml of spent medium was collected and frozen at -20 °C for future use or immediately processed. The collected supernatant was centrifuged at 250 g for 2 minutes at RT and transferred to a new Eppendorf tube. Then, the supernatant was centrifuged at 2000 g at RT for 10 minutes. The supernatant was discarded, and the DNA pellet was resuspended in 30 µL of PCR water. The pellet was heat-inactivated by heating it for 3 minutes at 95 °C. 2 µl of resuspended DNA was used as a template for the PCR, and the reaction mix was prepared according to Table 12. PCR was run according to the protocol depicted in Table 13.

To test for mycoplasma contamination, the PCR product was separated by agarose gel electrophoresis. 2% agarose gel was prepared by dissolving 6-8 g of agarose in 400 ml of 1X TAE buffer and boiling it in a microwave. The magnetic stirrer was dropped in the agarose gel solution and cooled down for 15 minutes at RT. After cooling down, StainIN green nucleic acid stain was added to the agarose gel solution according to the protocol. The agarose gel solution was poured into electrophoresis chambers, and the comb was inserted to create wells for sample loading. Once the gel was polymerized, the comb was removed, and 12 µl of the PCR product and GeneRuler™ 100 bp DNA ladder were loaded into the wells. Electrophoresis chambers were filled with 1X TAE buffer, and electrophoresis was carried out at 120 V for 1-2 hours. Visualization and documentation of the DNA bands separated on the agarose gel were done using the UVP UVsolo TS Imaging System.

Table 12: PCR reaction mix for mycoplasma contamination test

| Components | Volume/ reaction |
|--------------------|------------------|
| PCR pre-mix | 15 μ l |
| Forward Primer mix | 2 μ l |
| Reverse Primer mix | 2 μ l |
| PCR water | 9 μ l |
| DNA | 2 μ l |

Table 13: PCR protocol for mycoplasma contamination test

| Steps | Temperature | Time | Number of cycles |
|----------------------|-------------|---------|------------------|
| Initial denaturation | 95 °C | 15 mins | |
| Denaturation | 94 °C | 1 min | |
| Annealing | 60 °C | 1 min | |
| Extension | 74 °C | 1 min | X40 |
| Final extension | 72 °C | 10 mins | |

4.4 Proliferation assay

4.4.1 Proliferation assay for 2D cells

Cells were harvested from confluent flasks as described above in 4.1.1 and counted as described in 4.1.2. For each time point, cells were seeded in 6 technical replicates for each cell line, 1000 cells per well of a 96-well plate in complete DMEM high glucose media in 100 μ l of total volume per well. Proliferation was measured every day for five days. To measure the proliferation, media was discarded from the cells, and MTT reagent was added to the cells, 20 μ l/well. Then, the cells were incubated under standard cell culture conditions for 4 hours. Due to the mitochondrial metabolic activity of viable cells, MTT is

converted into formazan crystals, a purple-colored precipitate. At the end of 4 hours, the formazan crystals are solubilized for homogenous measurement by adding 200 μ l of the solubilizing agent. The solubilizing agent was prepared by mixing equal parts of absolute ethanol and DMSO. Then, the amount of formazan is detected by measuring the absorbance at 590 nm using a spectrophotometer. The proliferation rate of the cells at each time point was quantified by normalizing the absorbance to Day 0 absorbance.

4.4.2 Proliferation assay for 3D organoids

The proliferation assay for PDO lines was performed by the CellTiter-Glo® 3D Cell Viability Assay on white, clear-bottom 96-well plates. Single cells were isolated and counted from confluent wells of PDOs, as described above in 4.2.4. To avoid 2D growth, first the wells were coated with 10 μ l of 20% Matrigel diluted in 1X PBS, and the plate was incubated at 37 °C to allow the polymerization of the Matrigel coating. 1000 cells/well were seeded in 100 μ l of 10% Matrigel diluted in PDO media. Cells were seeded in six replicates for each PDO line and incubated under standard cell culture conditions until the endpoint. Before measuring, the CellTiter-Glo® reagent was prepared. For this, CellTiter-Glo® buffer and the lyophilized CellTiter-Glo® substrate were thawed to RT before use. Once thawed, the lyophilized CellTiter-Glo® substrate was reconstituted with 10 ml of CellTiter-Glo® buffer and mixed well by gently vortexing to prepare a homogeneous solution of CellTiter-Glo® reagent. To determine the viable cells, 25 μ l of CellTiter-Glo® reagent was added to each well, resulting in cell lysis and the generation of luminescence in proportion to the ATP present, directly proportionating the viable cells. The luminescence was measured every other day for ten days, and the proliferation rate of the PDO lines at each time point was quantified by normalizing the luminescence to Day 0 luminescence.

4.5 Scratch assay to determine *in vitro* migration potential

Murine 2D cells and PDO-derived 2D cells were harvested from confluent flasks as described above in 4.1.1, counted as described in 4.1.2, and seeded in triplicates in a 12-well plate with 100 000 cells per well in a total volume of 1 ml of complete DMEM high glucose and RPMI media, respectively. Cells were cultured for 24 hours under standard cell culture conditions, allowing the formation of a confluent

monolayer. Afterward, scratches of approximately similar sizes were made in each well by scraping off the cell monolayer in a straight line with a p200 pipet tip. Then, the cells were washed twice with 1 ml of complete growth media to remove the debris and smooth the edge of the scratch. Then, 1 ml of fresh media was added to the cells and incubated under standard cell culture conditions. Markings are made on the plates and used as reference points to obtain the same field during image acquisition. Then, phase contrast images of the marked areas of the scratches were acquired at 0, 4, 8, and 24 hours under 5X magnification using a Leica DM IL LED Fluo light microscope and LAS X software (version 3.5.5.19976, Leica). Afterward, acquired images were analyzed using Image J wound healing size tool plugin software to determine the closure of the scratch and the *in vitro* migration potential of the cells.

4.6 Imaging to morphologically characterize 2D cells and 3D organoids

4.6.1 Phase contrast microscopy imaging to morphologically characterize 2D cells and 3D organoids

2D cells and 3D organoids were cultured as described above in 4.1 and 4.2.2, and representative phase contrast microscopy images of the 2D cell lines and 3D organoids were taken at approximately 70-80% confluency to document the cell morphology under 4X magnification using a Leica DM IL LED Fluo light microscope and LAS X (version 3.5.5.19976, Leica).

4.6.2 Immunofluorescence staining for Phalloidin and confocal microscopy to morphologically characterize 2D cells and PDOs.

Immunofluorescence staining for F-actin, the polymerized form of actin filaments, was used to further document the cytoskeleton structure of morphologically diverse murine primary PDAC cells. Fluorescence-conjugated Phalloidin-Atto 647 antibody was used to stain the polymerized actin filaments. For this purpose, 2D cells were counted and seeded in desired amounts as described above in 4.1.2 in ibidi® μ -Slide 8-well ibiTreat cell culture plates and cultured them as described above in 4.1.1. Once the cell lines reached approximately 80-90% confluency, the cells were washed three times with 1X PBS and fixed for 10 min at RT using 4% PFA. Then, the cells were washed three times with 1X

PBS for 5 minutes to remove excess formaldehyde solution. Cells were treated with 0.15% glycine for 5 minutes to avoid background signals. Then, the cells were briefly permeabilized with 0.2% Triton X-100 in PBS for 2 minutes at RT. To remove the excess 0.2% Triton X-100 solution, cells were washed three times with 1X PBS. After washing, Phalloidin diluted to 1:250 in PBS was added to the cells and incubated at RT in the dark for an hour. The nuclei of the cells were counter-stained with DAPI (0.03 $\mu\text{L}/\text{mL}$ in PBS) for 2 minutes at RT in the dark. Then, the cells were washed three times with 1X PBS. Stained cells were kept in 1X PBS at 4 °C and protected from the light by an Alu foil covering until confocal imaging. Images were taken under 40X using the Leica TCS SP8 Confocal Microscope.

To document the morphology of the PDOs, immunofluorescence staining for F-actin was performed using fluorescence-conjugated Phalloidin-Atto 647. For this purpose, PDOs were seeded in ibidi® μ -Slide 8-well ibiTreat cell culture plates and cultured as described above in 4.2.2. Once the confluency was reached, PDOs were washed three times with 1X PBS and fixed for 15 min at RT using 4% PFA. Then, the PDOs were washed three times with 1X PBS for 5 minutes to remove excess formaldehyde solution. To avoid background signaling, PDOs were treated with 0.15% glycine for 5 minutes. Then, the PDOs were briefly permeabilized with 0.2% Triton-X 100 in PBS for 2 minutes at RT. To remove the excess 0.2% Triton X-100 solution, PDOs were washed three times with 1X PBS. Afterward, Phalloidin diluted to 1:250 in PBS was added to the PDOs and incubated at RT in the dark for an hour. The nuclei of the PDOs were counter-stained with DAPI (0.03 $\mu\text{L}/\text{mL}$ in PBS) for 2 minutes at RT in the dark. Then, the cells were washed three times with 1X PBS. Stained PDOs were kept in PBS at 4 °C and protected from the light by an Alu foil covering until confocal imaging. Images were taken under 40X using the Leica TCS SP8 Confocal Microscope.

4.7 Transcriptomic analysis

4.7.1 RNA isolation from murine 2D cells

To collect RNA from murine 2D cells, cells were seeded in a 10 cm cell culture plate and allowed to reach 80% confluency. Lysis buffer was prepared by adding 2-mercaptoethanol to RLT lysis buffer (1:100). 2-mercaptoethanol irreversibly denatures the RNases released during cell lysis. Once

confluency was reached, spent media was aspirated, and 350 μ l of RLT lysis buffer supplemented with 2-mercaptoethanol was added. Then, using a cell scraper, lysed cells were scraped off, and the lysate was collected. The collected lysates were homogenized by passing them through a 21-gauge needle attached to a syringe 5-10 times. Then, the lysates were either immediately processed or stored at -80 °C until RNA isolation. Using the RNeasy mini kit, RNA isolation was carried out according to the manufacturer's instructions. The concentration and purity of the isolated RNA samples were measured using a Nanodrop Spectrophotometer.

4.7.2 RNA isolation from PDOs

PDOs were harvested from four to six confluent wells as described above in 4.2.2, and 350 μ l of RLT lysis buffer supplemented with 2-mercaptoethanol was added to the cell pellet. Collected lysates were homogenized, and RNA isolation was carried out using the RNeasy mini kit, as described above in 4.7.1. RNA samples were measured using a Nanodrop Spectrophotometer.

4.7.3 Library Preparation and RNA Sequencing

For bulk sequencing of poly(A)-RNA, library preparation was performed as previously described (Parekh et al., 2016). Concisely, for each RNA sample, barcoded cDNA was generated using Maxima RT polymerase, an oligo-dT primer containing barcodes, unique molecular identifiers (UMI), and an adaptor. The 5' ends of the cDNAs generated were extended by using a template switch oligo (TSO). Then, the full-length cDNA was amplified with primers binding to the TSO site and the adaptor. Using the NEB UltraII FS kit, full-length cDNA was fragmented. The TruSeq adapter was ligated after end repair, and A-tailing and 3'-end fragments were amplified using primers with Illumina P5 and P7 overhangs. To achieve better cluster recognition compared to Parekh et al., P5 and P7 sites were exchanged to allow sequencing of the cDNA in read1 and barcodes and UMIs in read2. After library preparation, it was sequenced on a NextSeq 500 (Illumina) with 67 cycles for the cDNA in read1 and 16 for the barcodes and UMIs in read2.

4.7.4 RNA sequencing data analysis

Using the Drop-seq pipeline (v1.0), data was processed to generate sample- and gene-wise UMI tables (Macosko et al., 2015). According to samples, reference genomes (GRCm38 or GRCh38) were used for alignment. According to GENCODE Version M25, transcript and gene definitions were used to determine read counts per gene. For each sample, raw count data from RNA sequencing from the two technical replicates was combined by summing all counts per gene into one final raw count profile per sample. The resulting $m \times n$ count matrix (m genes, n samples) was imported into R-Studio (R version 4.0.2 (2020-06-22, open-source license)), and RNA-seq analysis was performed. Before downstream analysis, genes with total read counts < 5 across all samples (lowly expressed genes) were removed, and the remaining counts were normalized and transformed using regularized log transformation (rlog) implemented in the DESeq2 R package while considering different library sizes.

4.7.5 Molecular subtyping of murine and PDO lines

Based on the normalized RNA-seq profile for each sample, continuous classification using probabilities of class membership (Rashid et al., 2020) was determined. Using custom R code based on the gene pairs and coefficients provided by the authors, the Purity Independent Subtyping of Tumors (PurIST) single-sample classification scheme was implemented. According to the 3'prime end sequencing protocol as described above in 4.7.3, the adjustment of gene expression for total gene length was omitted. By rank transforming and rescaling first each column (cell line/PDOs) and then each row (gene) between 0 and 1, transcriptome-wide expression single-sample signatures were computed. Then, using analytic rank-based enrichment analysis (aREA) (Alvarez et al., 2016), molecular subtype classifier gene sets (Bailey et al., 2016; Chan-Seng-Yue et al., 2020; Collisson et al., 2011; Moffitt et al., 2015) were scored per sample using the pheatmap R package (Kolde, 2019). The resulting NES matrix with classifier sets in rows and individual cell lines in columns was illustrated.

4.8 Whole exome sequencing

4.8.1 Genomic DNA isolation

PDOs were harvested from four to six confluent wells as described above in 4.2.2, and DNA isolation was carried out using the AllPrep® DNA/RNA micro kit according to the manufacturer's instructions. Blood samples from the same patients were used as reference tissues. Genomic DNA from the blood samples was isolated using the AllPrep® DNA/RNA micro kit according to the manufacturer's instructions. The concentration and purity of the isolated DNA samples were measured using a Nanodrop Spectrophotometer.

4.8.2 Library preparation and whole-exome sequencing

Using the Agilent SureSelectXT Low Input Exome-Seq Human v7 kit, exome-enrichment and whole exome sequencing library preparation were carried out according to the manufacturer's instructions. Using the Illumina NovaSeq 6000 sequencer, samples were sequenced, resulting in approximately 140 Mio. 100 bp-long paired-end reads per sample. For downstream alignment and mutation calling, the GATK Best Practice suggestions were followed. Next, read trimming was performed using Trimmomatic 0.38 (LEADING:25 TRAILING:25 MINLEN:50). Afterward, BWA-MEM 0.7.17 was used to align the reads to the human reference genome (GRCh38.p7). By default, Picard 2.18.26 and GATK 4.1.0.0 were used for postprocessing (CleanSam, MarkDuplicates, and BaseRecalibrator). Using MuTect2 v4.1.0.0 (default settings), somatic mutations were called. For downstream processing, only mutations with at least two reads supporting the alternate allele and a base coverage of at least 10 in the tumor and germline were used. Using SnpEff 4.3t, based on ENSEMBL, 92 single nucleotide variants (SNVs) and insertions/deletions (Indels) ≤ 10 base pairs were annotated. To detect copy number variations, Copywriter 2.6.1.2 (default settings) was used.

4.9 Chick embryo chorioallantoic membrane (CAM) xenograft model experiments

4.9.1 Preparing the CAM for transplantation

Fertilized specific pathogen-free (SPF) chicken eggs were obtained from ValoBiomedica, Osternholz-Scharmbeck. The eggs were incubated at 37 °C and 70% - 80% humidity to activate embryogenesis. Until embryonic development day (EDD) 4, the eggs were undisturbed in the incubator. On EDD 4, the eggs were turned upside down with more rounded poles facing upwards. Since the air sac resides on the more rounded pole, turning the eggs in this way facilitates the movement of the embryo toward this more rounded pole. Then, the eggshell on the more rounded pole was disinfected by wiping it with 70% ethanol. A small piece of silk tape was placed on the eggshell at the more rounded pole of the egg, covering the tip. Afterward, a small window was made on the tip at the more rounded pole of the eggshell to allow the egg contents to drop down (Figure 4). The window on the eggshell was covered with a small piece of silk tape. The eggs were further incubated until EDD7. On EDD 7, the small piece of silk tape was removed, and the small window on the eggshell was made bigger (1-1.5 cm) by cutting it further (Figure 4). The windows were made wide enough to allow further *in ovo* manipulations. If the eggshell membrane was still attached to the CAM, it was removed carefully. For this, a drop of sterile PBS was applied to the eggshell membrane using a plastic Pasteur pipette. A small cut was made into the eggshell membrane using a sterile scalpel, allowing the PBS to flow into the space between the eggshell membrane and the CAM. Then, the eggshell membrane was removed carefully by peeling it off from the CAM using sterile forceps without disturbing the CAM vasculature. To prevent drying out and contamination of the CAM, the window was sealed again with silk tape. The eggs were further incubated until EDD 9 to allow further development of the CAM.

4.9.2 Preparation of 2D murine PDAC cells for transplantation

On EDD 9, the 2D murine PDAC cells were harvested from confluent flasks as described above in 4.1.1 and counted as described in 4.1.2. For the transplantation of each egg, 1×10^6 cells were mixed with 40 μ l of Matrigel, and a small droplet was made on the lid of a petri dish and left undisturbed at RT for 10

minutes. To allow the polymerization of the Matrigel, the droplets were incubated for 45-60 minutes under standard cell culture conditions.

4.9.3 Preparation of PDOs for transplantation

Since the aim is to transplant a determined number of 3D PDOs on CAM, single cells have to be isolated from organoids, counted, and cultured to form organoids before transplantation. Once trypsinized, the single cells from PDOs require at least 5 to 10 days in culture to form organoids, depending on the growth rates of the PDO lines. Hence, the growth rates of the PDO lines were determined as mentioned above in 4.4.2. Cells were seeded on coverslips placed in a 6-well plate and cultured in complete PDO media under standard cell culture conditions for ten days to allow the formation of 3D organoids before transplantation.

4.9.4 Transplantation on the CAM

On EDD 9, chick embryos were checked for viability, and dead chick embryos were discarded. For transplantation, murine PDAC cells were prepared, as mentioned in 4.9.2. The silk tape covering the window on the eggshell was removed, and the tumor cell Matrigel droplet was scooped carefully from the petri dish using a spatula. Then, the tumor Matrigel droplet was dropped on the CAM. Similarly, PDOs were prepared as described in 4.9.3 and dropped on the CAM. After transplantation, a window on the eggshell was taped again with silk tape, and the eggs were further incubated until EDD 14 (Figure 4).

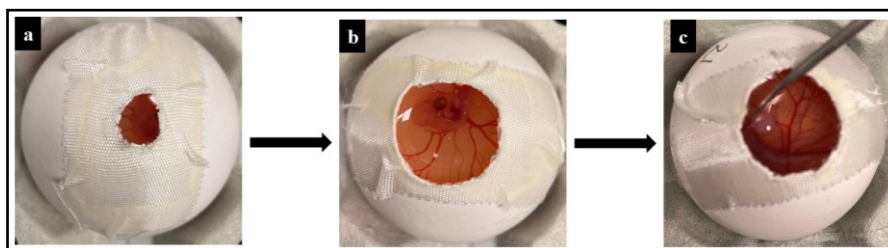


Figure 4: CAM assay workflow.

a) On EDD 4, a small window was made on the more rounded pole of the eggshell to allow the egg contents to drop. b) On EDD 7, the small window on the eggshell was made bigger (1-1.5 cm) by cutting it further. c) On EDD 9, either 2D cells as Matrigel droplets or 3D PDOs were transplanted onto the CAM, and the transplanted eggs were incubated further until EDD 14.

4.9.5 Harvest of the primary tumor and chick embryo organs

On EDD 14, the primary tumor was harvested, and the chick embryo organs were collected. To harvest the primary tumor on EDD 14, the silk tape covering the window on the eggshell was removed. The CAM surrounding the tumor was grabbed with dissection forceps and cut with scissors. The harvested primary tumor with surrounding CAM was placed in an embedding cassette and fixed using 4% PFA overnight at RT. As soon as the tumor was harvested, the eggshell was cut radially into equal halves, and the contents of the eggs were decanted in a tray. The chick embryo was killed by decapitation. The chick embryo was dissected to collect selected organs, namely the brain, heart, and liver. The collected organs were individually transferred into cryovials and snap-frozen in liquid nitrogen. Snap-frozen chick embryo organs were stored at -80 °C until further processing.

4.10 Histological analysis of primary tumors

4.10.1 Tissue fixation and sectioning

Tissues were fixed in 4% PFA overnight at RT and stored in PBS at 4 °C until dehydration. Dehydration and tissue embedding in paraffin wax performed by the Institute of Pathology, Klinikum rechts der Isar, Technical University of Munich. Paraffin blocks were stored at RT until further use. For histological analysis, a series of 2.5 µm sections were cut from each paraffin block and mounted on labeled, clean adhesive microscopy slides.

4.10.2 Hematoxylin and eosin staining

Hematoxylin and eosin staining (H&E) was mainly performed by the Institute of Pathology, Klinikum rechts der Isar, Technical University of Munich. Formalin-fixed paraffin-embedded (FFPE) tissue sections were deparaffinized in xylene twice for 5 minutes. Afterward, the sections were rehydrated in a 100%, 96%, and 80% ethanol series twice for 3 minutes to remove the xylene. Then, the sections were rehydrated by washing in tap water for 3 minutes to allow the penetration of aqueous reagents. The tissues were stained with hematoxylin for 30 seconds to stain the nuclei and immediately rinsed in running tap water for 10 minutes to remove the excess hematoxylin dye. Then, the sections were stained

with eosin to stain the cytoplasm for 20 seconds and washed again in tap water to remove the excess eosin staining. Afterward, the slides were dehydrated using 80%, 96%, and 100% ethanol series twice each for 3 minutes to remove the water. After that, the sections were incubated in xylene twice for 5 minutes to clear the tissue, rendering it completely transparent. Then, the sections were mounted using a Pertex mounting medium and dried overnight at RT. Then, the sections were scanned using the Aperio Versa 8 digital scanner, and documentation was done using the Aperio Image Scope software (v.12.3.3.5048).

4.10.3 Immunohistochemical staining

FFPE sections were deparaffinized in xylene and rehydrated through a decreasing series of ethanol and subsequently in water, as mentioned in 4.10.2. To enable the primary antibody to access the protein within the tissue, heat-mediated antigen retrieval was performed. For this purpose, the sections were immersed in a citric acid-based antigen unmasking solution and boiled in a microwave at 500 W for 3 minutes and then at 350 W for 10 minutes. Then, the sections were cooled down at RT for 20-30 minutes. Endogenous peroxidase activity of the tissues was quenched by incubating the tissue sections in 3% hydrogen peroxidase in TBST for 10 minutes at RT to reduce the non-specific signal and washed three times with 1X TBST. The tissue sections were incubated with a drop of Avidin for 15 minutes to reduce the non-specific signal due to endogenous Avidin. Afterward, the tissue sections were washed three times with 1X TBST. Then, the tissue was incubated with a drop of Biotin for 15 minutes to reduce the non-specific signal due to endogenous Biotin. Afterward, the tissue sections were washed three times with 1X TBST and blocked with 5% BSA in 1X TBST for 1 hour at RT. Then, the sections were incubated with primary antibodies diluted in 5% BSA in 1X TBST overnight at 4 °C. Then, the sections were washed three times with 1X TBST. Afterward, the tissue sections were incubated with the appropriate secondary antibody conjugated to Biotin diluted in 1X TBST at RT for 30 minutes and washed three times with 1X TBST. To detect the positive signal, Vectastain® Elite HRP-conjugated ABC reagent prepared according to the manufacturer's instructions was added to the tissue sections and incubated at RT for 30 minutes. Then, the tissue sections were washed three times with 1X TBST. Vector® DAB substrate was prepared according to the manufacturer's instructions and used to develop

the signal. Once the signal was developed, the reaction was stopped with ddH₂O. Counterstaining was done by incubating the tissue sections in Hematoxylin for 20 seconds and subsequent bluing by washing under running tap water. Then, the tissues were dehydrated and mounted, as mentioned above in 4.10.2. Then, the mounted sections were let dry overnight at RT and scanned using the Aperio Versa 8 digital scanner. Documentation and IHC quantification were performed on the digital scans of the tissue sections using the Aperio Image Scope software (v.12.3.3.5048) using the Positive Pixel Count v9 algorithm.

4.10.4 Immunofluorescence staining

FFPE sections were deparaffinized, and heat-mediated antigen retrieval was performed as described above in 4.10.3. Then, the sections were cooled down at RT for 20-30 minutes. The sections were blocked using 5% BSA in 1X TBST for 1 hour at RT to reduce the non-specific background. Then, the sections were incubated with primary antibodies diluted in 5% BSA in 1X TBST overnight at 4 °C. Afterward, the sections were washed three times with 1X TBST and incubated with the appropriate fluorescence-conjugated secondary antibody diluted in 1X TBST at RT for 2 hours. Then, the sections were washed three times with 1X TBST, and counter-staining was performed with DAPI (0.03 µL/mL in PBS) for 2 minutes at RT in the dark. Then, the tissues were washed three times with 1X TBST, and the stained sections were kept at 4 °C and protected from the light until confocal imaging. Images were taken under 40X magnification using the Leica TCS SP8 Confocal Microscope.

4.10.5 Sirius red staining

To quantify the fibrillar collagen deposition in the CAM tumors, Sirius staining was performed on tumor tissue sections. For Sirius red staining, FFPE sections were deparaffinized in xylene and rehydrated through a decreasing series of ethanol and subsequently in water, as mentioned in 4.10.2. Then, the tissue sections were immersed in Sirius red solution for 1 hour and 30 minutes at RT in the dark. Then, the tissue sections were rinsed in absolute ethanol for 5 minutes at RT. The slides were again washed in fresh absolute ethanol until the ethanol no longer turned green. After washing, the tissue sections were incubated in xylene for 15 minutes to clear the tissue, rendering it completely transparent. Then, the

sections were mounted using a Pertex mounting medium and let dry overnight at RT. Then, the slides were scanned using Aperio Versa 8 digital scanner to get an overview of the Sirius red staining on CAM xenografts. In tissues, Sirius red binds to various molecules, including fibrillar collagens. Upon binding to Sirius red, the natural birefringence of fibrillar collagen is enhanced, which can then be detected using polarized light and quantified (Lattouf et al., 2014). Hence, using a DMI8 Leica Thunder microscope, polarized imaging of Sirius red-stained slides was performed, and the birefringence was measured. Using Image J software, positive pixels in each tissue section were quantified, and the percentage of Sirius red positive area was calculated.

4.10.6 Hyaluronan-binding protein staining

Hyaluronan binding protein (HABP) staining was performed on tumor tissue sections to quantify the hyaluronan deposition in the CAM xenografts. HABP comprises a hyaluronan binding domain with the linked module from aggrecan and serves as a hyaluronan probe (Yang et al., 2019). Hence, a biotinylated recombinant HABP protein was used to detect hyaluronan in the CAM xenografts. To perform HABP staining, FFPE sections were deparaffinized, as mentioned above in 4.10.2. Endogenous peroxidase blocking was performed as mentioned above in 4.10.3 and stabilized in 1X TBST for 10 minutes. Slides were transferred to a humid chamber, and Avidin and Biotin blocking was performed, as mentioned above in 4.10.3, to reduce the non-specific signal due to endogenous Avidin and Biotin. Afterward, the tissue sections were washed three times with 1X TBST and incubated with HABP diluted to a final concentration of 2 $\mu\text{g/ml}$ in 5% BSA in 1X TBST for 2 hours and 30 minutes at RT. Afterward, the tissue sections were washed three times with 1X TBST and incubated with ABC reagent, as mentioned above in 4.10.3. Then, the tissue sections were washed three times with 1X TBST, and the signal was developed using the Vector® DAB peroxidase substrate kit as mentioned above in 4.10.3. Afterward, counter-staining was performed, and the tissue sections were dehydrated, as mentioned in 4.10.3. Then, the slides were mounted and let dry overnight at RT, as mentioned above in 4.10.3. Stained slides were scanned using the Aperio Versa 8 digital scanner. Documentation and IHC quantification were performed on the digital scans of the tissue sections using the Aperio Image Scope software (v.12.3.3.5048) using the Positive Pixel Count v9 algorithm.

4.11 Species-specific qPCR to determine metastases in chick embryo organs

For metastasis quantification, chick embryo organs, selectively the brain, heart, and liver, were collected and stored at -80 °C, as described in 4.9.5. Murine or human cells metastasizing to the chick embryo organs can be quantified by amplifying species-specific sequences by qPCR.

4.11.1 Genomic DNA isolation from chick embryo organs

To isolate DNA, chick embryo organs were thawed on ice. DNA isolation from the chick embryo brain, heart, and liver was carried out using the Macherey Nagel Nucleospin genomic DNA isolation kit according to the manufacturer's instructions. Isolated DNA was stored at -20 °C until use. The concentration and purity of the DNA were measured using a Nanodrop Spectrophotometer. Then, the isolated DNA samples were diluted with PCR water to prepare the working concentration of 20 ng/μl for each sample.

4.11.2 Human-specific *Alu* qPCR to determine PDO metastasis in the chick embryo organs

By detecting human DNA in chick embryo organs, PDO metastasis can be determined. *Alu* sequences are specific to the human genome and absent in the avian genome (Schneider et al., 2002). Hence, by amplifying the *Alu* sequences using *Alu*-specific primers, human DNA in the chick embryo organ genomic DNA can be determined. Using SensiFast™ SYBR Hi-Rox Kit according to the manufacturer's protocol, the reaction mix was prepared as mentioned in Table 14, and qPCR was performed with the StepOnePlus™ real-time PCR system according to the protocol mentioned in Table 15. SYBR Green binds only to newly synthesized double-stranded (ds) DNA, resulting in a fluorescent signal. The fluorescence intensity can be measured at the end of each qPCR cycle and used to quantify the amount of newly built ds DNA. Chicken GAPDH was used as an internal control to confirm the presence of equivalent quantities of host genomic DNA. To check for primer dimer formation, a melt curve analysis was performed. qPCR data were analyzed using the 2- $\Delta\Delta C_t$ method (Pfaffl, 2001).

Table 14: qPCR reaction mix for metastasis quantification

| Components | Volume/ reaction |
|--------------------------------------|------------------|
| SensiFast™ SYBR Hi-Rox 2X master mix | 10 µl |
| 10 µM Forward Primer | 0.8 µl |
| 10 µM Reverse Primer | 0.8 µl |
| PCR water | 3.4 µl |
| DNA | 5 µl |

Table 15: *Alu* and *chGAPDH* qPCR protocol

| Steps | Temperature | Time | Number of cycles |
|----------------------|-------------|---------|------------------|
| Initial denaturation | 95 °C | 15 mins | |
| Denaturation | 95 °C | 15s | X 40 |
| Annealing | 60 °C | 30s | |
| Extension | 72 °C | 30s | |
| Melt curve | 95 °C | 15s | |
| | 60 °C | 1 min | |
| | 95 °C | 15s | |

4.11.3 *B1* qPCR to determine the metastasis of murine cells in the chick embryo organs

The CAM model has been mostly used to study human cancer metastasis by human-specific *Alu* qPCR. Using a similar concept, murine-specific *B1* qPCR can be used to quantify murine cell metastasis in chick embryo organs. The *B1* sequence is the murine analog of *the Alu* sequence, which is specific to the primate genome but absent in the avian genome (H. Zhang et al., 2009). Hence, the efficiency of

murine *BI* qPCR to detect murine DNA was first evaluated. In addition, potential amplification in chicken DNA by *BI* sequence-specific primers was evaluated. For this purpose, murine DNA is isolated from 3 different cell lines and chick embryo brain, heart, and liver using a Macherey Nagel Nucleospin genomic DNA isolation kit according to the manufacturer's instructions. Isolated DNA was stored at -20 °C until use. The concentration and purity of the DNA were measured using a Nanodrop Spectrophotometer. Then, the isolated DNA samples were diluted with PCR water to prepare serial dilutions of murine and chick embryo DNA ranging from 20 ng/μl to 2×10^{-5} ng/μl. qPCR was performed to amplify serially diluted murine and chick embryo DNA using *BI* sequence-specific qPCR. Using SensiFast™ SYBR Hi-Rox Kit according to the manufacturer's protocol, the reaction mix was prepared as mentioned in Table 14, and qPCR was performed with the StepOnePlus™ real-time PCR system according to the protocol mentioned in Table 16. To detect the metastatic dissemination of the murine cells in CAM xenografts, *BI* qPCR was performed similarly to *Alu* qPCR as described above in 4.11.2 according to the protocol mentioned in Table 16.

4.12 Statistical analysis

All the data were obtained from at least three independent experiments, unless otherwise specified. All statistical analyses were performed using GraphPad Prism (Version 5.00). The statistical significance of the data was determined by distinct statistical tests according to the dataset and stated in the respective figure legends. A P-value of ≤ 0.05 was considered to be statistically significant. P-values and the respective symbols are denoted in Table 17.

Table 16: *BI* qPCR protocol

| Steps | Temperature | Time | Number of cycles |
|----------------------|-------------|--------|------------------|
| Initial denaturation | 95 °C | 8 mins | |
| Denaturation | 95 °C | 30s | X 40 |
| Annealing | 55 °C | 40s | |
| Extension | 72 °C | 1 min | |
| Melt curve | 95 °C | 15s | |
| | 60 °C | 1 min | |
| | 95 °C | 15s | |

Table 17: Symbols denoting p-value ranges

| P value | Symbol |
|---------|-----------------|
| * | $p \leq 0.05$ |
| ** | $p \leq 0.01$ |
| *** | $p \leq 0.001$ |
| **** | $p \leq 0.0001$ |

5. Results

5.1 Establishment of CAM model to study PDAC subtypes

The study aimed to establish the CAM model to investigate distinct subtypes of PDAC and characterize the tumor growth, metastasis, and microenvironment. For this purpose, we used phenotypically diverse fluorescent reporter-tagged endogenous KPC mouse-derived cell lines that are morphologically and transcriptomically characterized.

5.1.1 Morphological characterization of KPC mouse-derived cell lines.

In vitro morphological characterization of the KPC murine cell lines was performed using phase contrast microscopy (Figure 5). Cell line 9366 showed a polygonal epithelial morphology, whereas R405 showed a characteristic elongated mesenchymal morphology (Figure 5). In contrast, a mixed morphology with clusters of both polygonal and elongated cells was observed for cell line 12548.

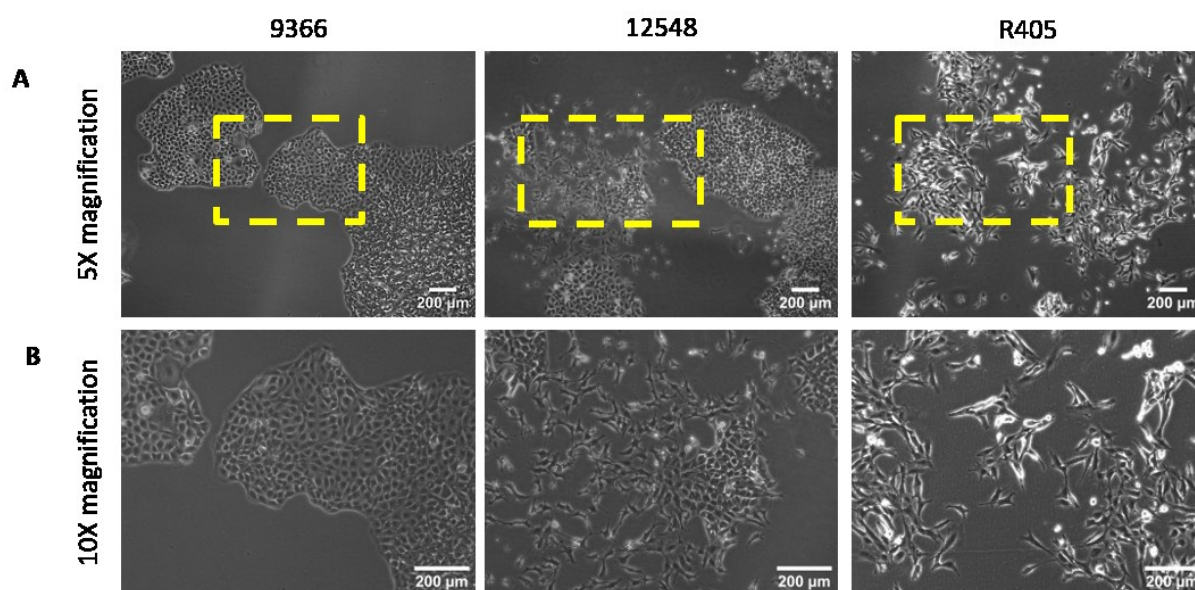


Figure 5: Morphological characterization of KPC mouse-derived cell lines by phase contrast microscopy.

Phase contrast images of the KPC mouse-derived cell lines. A) 5X magnification, B) 10X magnification of the highlighted field shows the epithelial, mixed, and mesenchymal phenotypes of the cell lines 9366, 12548, and R405, respectively.

Further morphological characterization was done through the visualization of the cytoskeleton structure of the cells by staining for F-actin filaments. In cell line 9366, F-actin was predominantly organized as

cortical bundles and maintained epithelial growth by forming the adhesion belt that links the cytoskeleton of adjacent cells (Figure 6). In contrast, in the cell line R405 F-actin filaments were organized towards the elongated edges of the cells as stress fibers. Clusters of cells with both epithelial and mesenchymal-like characteristic F-actin organizations were observed in cell line 12548. Based on the phenotypes observed by phase contrast microscopy imaging and F-actin cytoskeleton organization by immunofluorescence microscopy, the cell lines 9366, 12548, and R405 were morphologically characterized as epithelial, mixed, and mesenchymal, respectively (Figure 6).

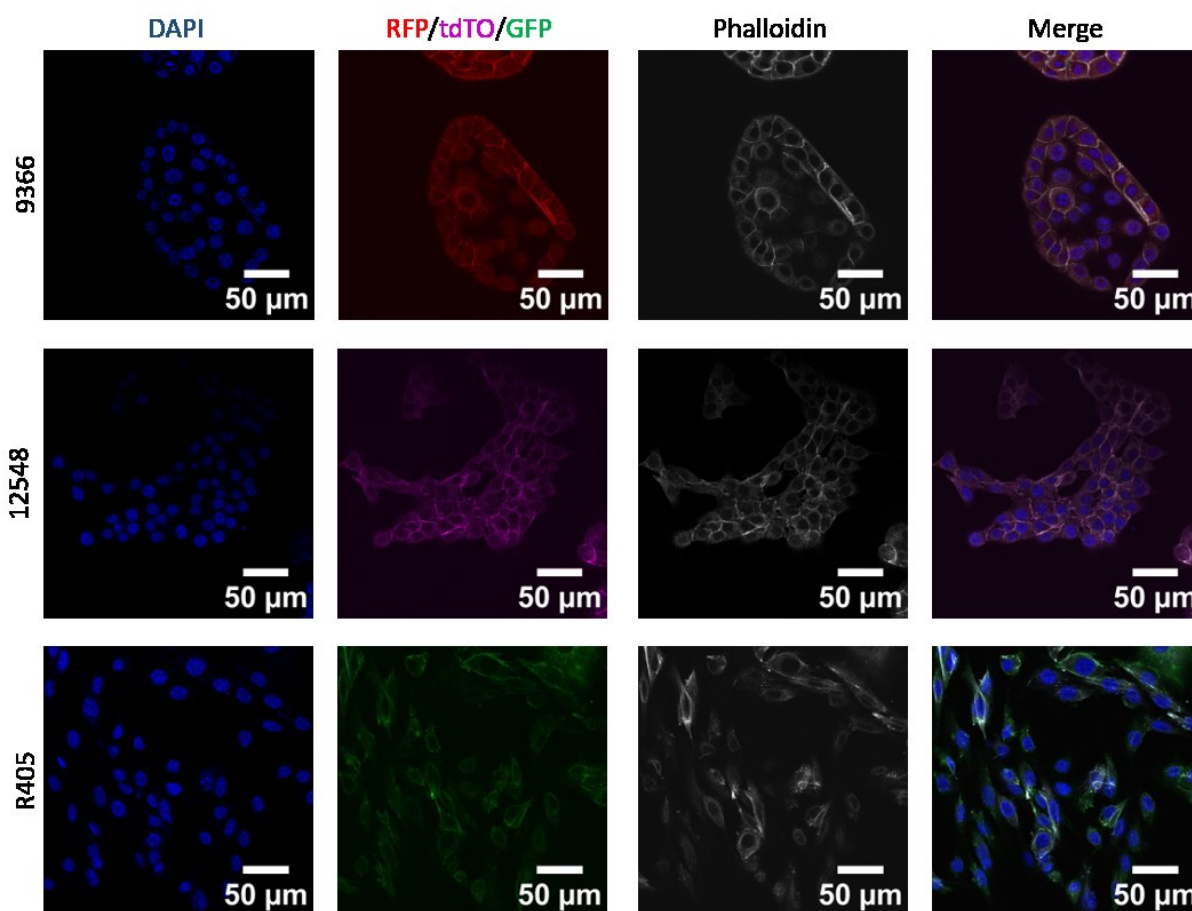


Figure 6: Morphological characterization of KPC mouse-derived cell lines by F-actin staining.

Immunofluorescence staining of F-actin in KPC mouse-derived cell lines 9366, 12548, and R405 under 40X magnification. The image panel shows the nuclei staining (DAPI), endogenous reporter of each cell line (RFP/tdTO/ GFP), F-actin staining (Phalloidin), and the merged images. Distinct F-actin organization and cytoskeleton structure corresponding to the epithelial, mixed, and mesenchymal phenotypes were observed for the cell lines 9366, 12548, and R405.

5.1.2 Transcriptomic Characterization of KPC mouse-derived cell lines

As the cell lines 9366, 12548, and R405 showed clearly distinguishable epithelial, mixed, and mesenchymal morphological features and growth patterns, respectively, the underlying molecular characteristics attributable to the well-known PDAC subtypes were investigated. For this purpose, on the bulk RNA seq data from cell lines 9366, 12548, and R405, the PurIST (purity-independent subtyping of tumors) score was applied. The PurIST score is a single sample classifier developed based on the well-known PDAC subtyping schemas (Bailey et al., 2016; Chan-Seng-Yue et al., 2020; Collisson et al., 2011; Moffitt et al., 2015), and it classifies the PDAC subtypes based on the selected eight gene pairs (TSP), each composed of basal-like (Gene A) and classical (Gene B) genes. When the PurIST single sample classifier was applied, the 9366 cell line scored highly for the classical molecular signatures of Collisson's, Moffitt's, Bailey's, and Chan-Seng-Yue's (CSY) PDAC subtyping (Figure 7). On the other hand, the cell line R405 scored highly for basal-like molecular signatures of Collisson's, Bailey's, and CSY's PDAC subtyping (Figure 7). The cell line 12548 scored positively for the classical molecular signatures of Collisson's, Bailey's, and CSY's PDAC subtyping (Figure 7). Interestingly, it scored positively for the quasi-mesenchymal molecular signatures of Collisson's and basal molecular signatures of Moffitt's and CSY's PDAC subtyping (Figure 7). Hence, cell line 12548 was transcriptomically characterized as an intermediate quasi-mesenchymal subtype.

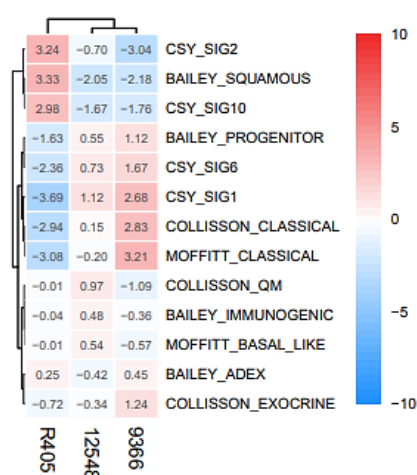


Figure 7: Transcriptomic characterization of KPC mouse-derived cell lines based on the PurIST single sample classifier.

Upon applying the PurIST single sample classifier based on the well-known PDAC subtyping schemas, the cell lines 9366, 12548, and R405 were characterized as classical, quasi-mesenchymal, and basal subtypes of PDAC.

5.1.3 Establishment of the CAM workflow using KPC mouse-derived cell lines representing distinct PDAC subtypes

Once the morphological and transcriptomic characterization of KPC mouse-derived cell lines was done, cells were transplanted onto the CAM. For successful transplantation and tumor growth, the eggs were prepared carefully. The prick made on the eggshell on EDD 4 allowed the CAM to detach from the eggshell membrane, thereby facilitating the growth of CAM. The second opening on the eggshell on EDD 7 allowed access to a larger area of CAM for transplantation. On EDD 9, when the CAM was completely grown, cells were transplanted as Matrigel droplets for each of the lines. For the cell lines 9366, 12548, and R405 representing classical, quasi-mesenchymal, and basal PDAC subtypes, respectively, the transplantation of 1×10^6 cells resulted in successful tumor engraftment five days after transplantation (EDD 14), as determined by the macroscopic tumor growth on the CAM. On EDD14, primary tumors established on the CAM were harvested together with chick embryo organs, selectively the brain, heart, and liver (Figure 8).

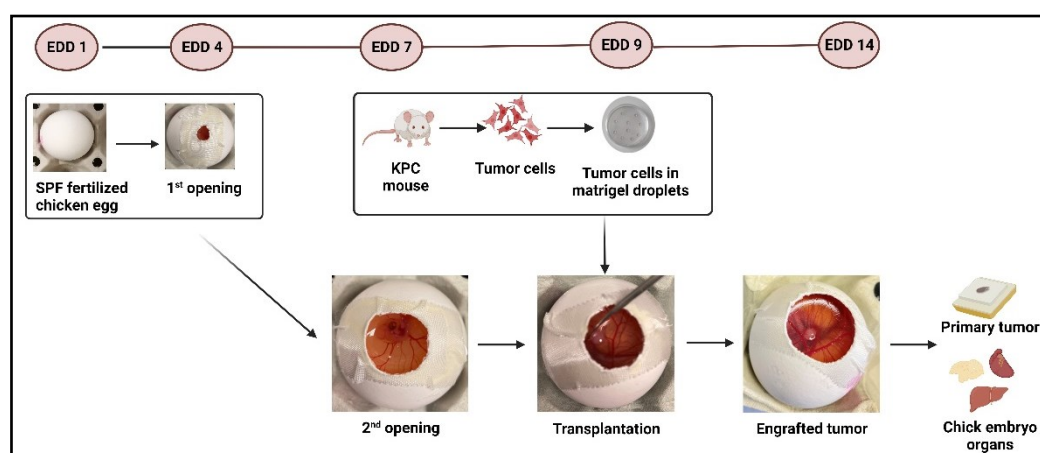


Figure 8: Establishment of the workflow using KPC mouse-derived cell lines representing distinct PDAC subtypes.

To achieve successful tumor engraftment, fertilized chicken eggs were prepared, facilitating the complete growth of CAM. For this purpose, as soon as the eggs were received, they were stored appropriately, and embryogenesis was initiated by providing 37 °C temperature and 70%-80% humidity. The first and second openings were made on EDD 4 and 7, respectively, allowing for the detachment of CAM from the eggshell membrane and growth. On EDD 9, tumor cells were prepared as Matrigel droplets and transplanted onto the CAM. Upon transplantation of 1×10^6 cells, successful engraftment was achieved for cell lines 9366, 12548, and R405 on EDD 14. Successfully engrafted primary tumors were harvested with chick embryo organs such as the brain, heart, and liver.

5.1.4 Tumor take rates of KPC mouse-derived cell lines in the CAM model

Even though the KPC mouse-derived cell lines representing each subtype of PDAC engrafted successfully on CAM to form macroscopic tumors, differences in tumor take rates were observed between the cell lines. To compare the tumor take rates on EDD 9, the total number of transplanted eggs was noted for each cell line. On EDD 14, at harvest time, the number of eggs showed successful tumor engraftment, no tumor engraftment, and non-viable eggs were noted down for each cell line. Successful engraftment of KPC mouse-derived cell lines was determined by the observation of macroscopic tumor growth on the CAM (Figure 9A). Using the formula,

$$\frac{\text{Number of successfully engrafted eggs}}{\text{Number of transplanted Eggs} - \text{Number of non viable eggs}} \times 100\%$$

tumor take rates of KPC mouse-derived cell lines on CAM were determined (Figure 9B). Cell line 9366, representing the classical PDAC subtype, showed the highest tumor take rate, followed by cell lines 12548 and R405, representing the quasi-mesenchymal and basal PDAC subtypes. A statistically significant difference in tumor take rates was observed between cell lines 9366 and R405. Cell line 12548 showed no statistically significant differences in tumor take when compared with the tumor take rates of 9366 and R405 cell lines.

5.2 Characterization of selected cancer hallmarks in PDAC using the CAM model

5.2.1 Characterization of the primary tumor histology of the CAM xenografts

To investigate the histomorphological features of the CAM xenografts, tissue sections were obtained from paraffin-embedded blocks of CAM primary tumors, and H&E staining was performed according to a standard routine protocol. H&E-stained slides were then scanned using the Aperio Versa 8 digital scanner, and images were documented using Aperio Image Scope software (v.12.3.3.5048). In the H&E-

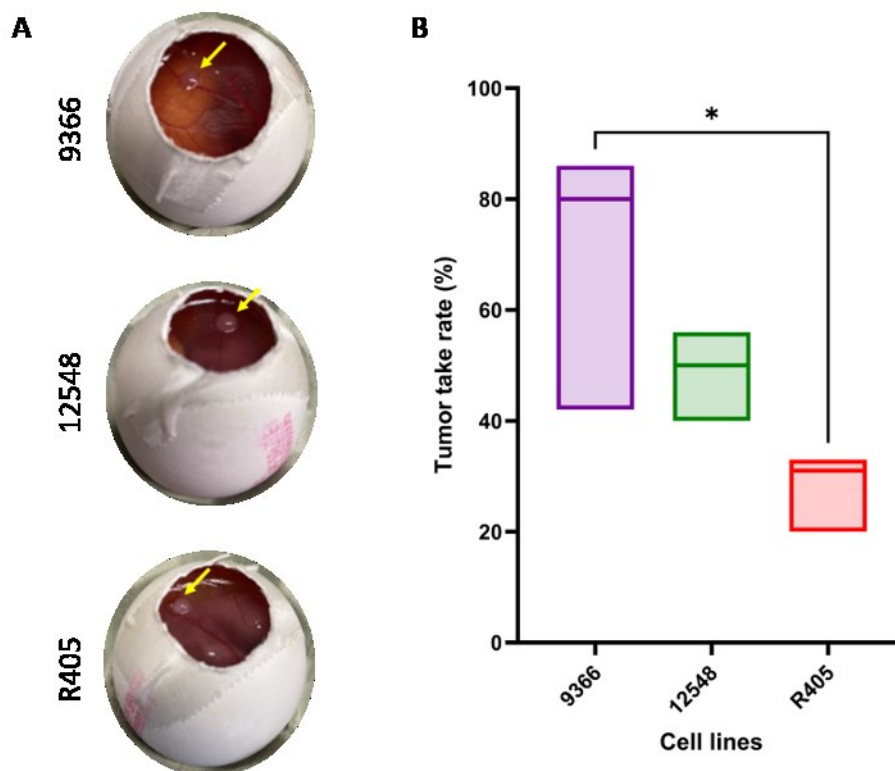


Figure 9: Tumor take rates of KPC mouse-derived cell lines on CAM.

A) Representative macroscopic tumors of the cell lines 9366, 12548, and R405 on CAM (indicated by yellow arrows), B) Tumor take rates of the cell lines 9366, 12548, and R405 on CAM. Tumor take rates were calculated by dividing the number of eggs that showed successful engraftment by the total number of viable eggs at harvest. The total number of viable eggs at the time of harvest was calculated by subtracting the non-viable eggs at the time of harvest from the total number of transplanted eggs. The data were collected from three independent experiments ($n = 3$, $N = 8$), and the Kruskal-Wallis test was performed to evaluate the statistical significance (* p -value = 0.0171).

stained sections of the CAM xenografts of the KPC mouse-derived cell lines 9366, 12548, and R405, the tumor area and CAM were easily distinguished. The tumor area appeared as a solid mass of tumor cells (indicated by orange arrows in Figure 10) embedded in the Matrigel matrix, which was used as a solid substrate for tumor cells. CAM appeared as a thin membrane surrounding the solid tumor (indicated by blue arrows in Figure 10). Blood vessels containing nucleated erythrocytes in light pink were seen both in the solid tumor area (indicated by red arrows in Figure 10) and CAM (indicated by green arrows in Figure 10).

The histomorphological features of the CAM tumors and the respective endogenous mouse tumors were compared (Figure 11). For this purpose, similar to the CAM sections, endogenous mouse tumor sections were obtained from paraffin-embedded blocks, and H&E staining was performed according to a standard

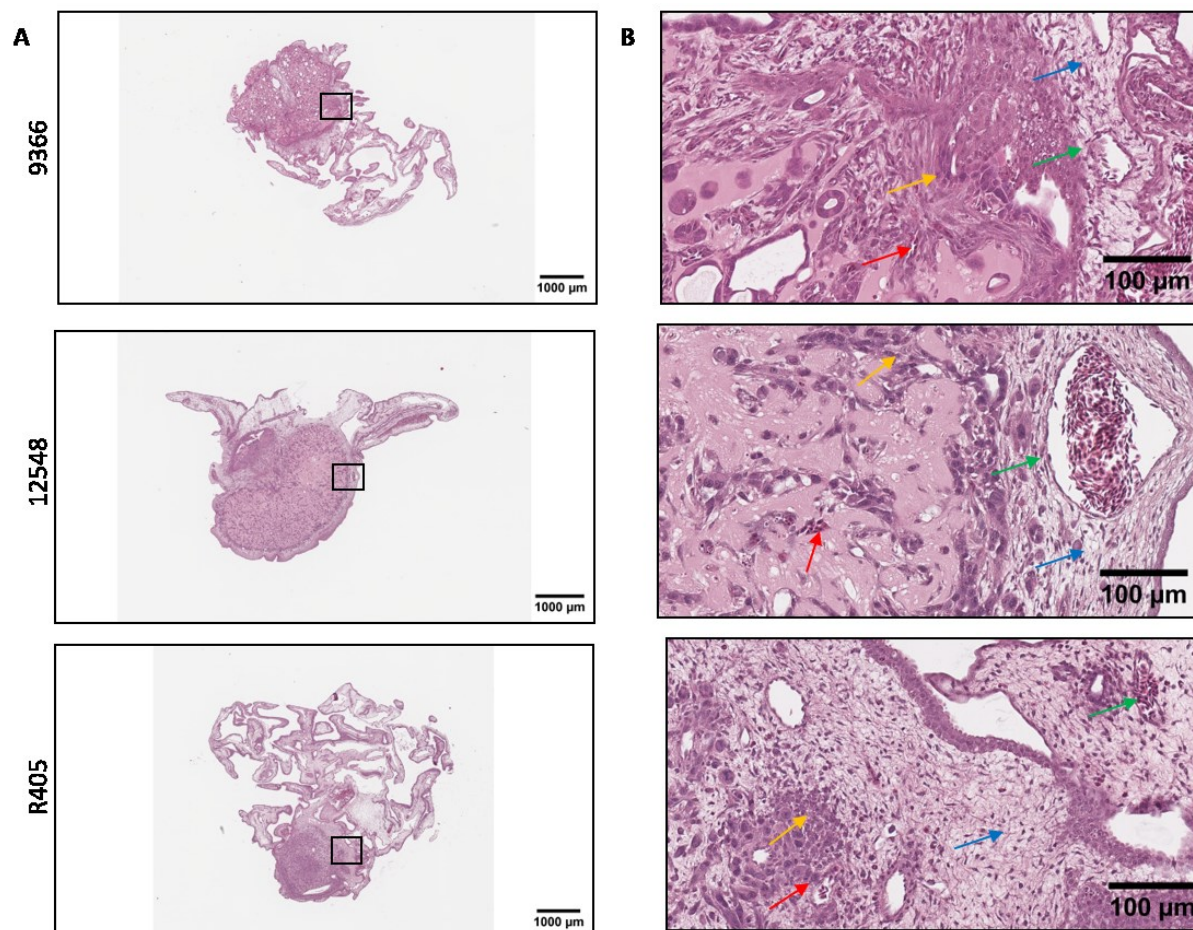


Figure 10: General histology of the CAM tumors in which the tumor area, CAM, and blood vessels within the tumor area and CAM were easily distinguished.

A) Overview of representative H&E-stained 9366, 12548, and R405 CAM tumor sections under 2X magnification, B) Representative H&E-stained 9366, 12548, and R405 CAM tumor sections under 40X magnification. The tumor area (indicated in orange arrows), CAM (indicated in blue arrows), blood vessels within the tumor area (indicated in red arrows), and CAM (indicated in green arrows) were easily distinguished in the H&E-stained CAM xenografts.

routine protocol. H&E-stained slides were then scanned using the Aperio Versa 8 digital scanner, and images were documented using Aperio Image Scope software (v.12.3.3.5048). Cell line 9366, representing the classical PDAC subtype, showed moderately differentiated ductal neoplastic growth in both CAM as well as endogenous mouse tumors. However, in 9366 CAM xenografts, minimal stromal infiltration was observed around a few ductal neoplastic changes, whereas in the endogenous mouse

tumor, extensive desmoplastic stroma was observed. The cell line 12548, representing the quasi-mesenchymal PDAC subtype, showed a mixed histomorphological feature of both moderately differentiated ductal and poorly differentiated neoplastic growths in the CAM and endogenous mouse tumors. In the CAM tumors, high stromal infiltration was observed around the poorly differentiated

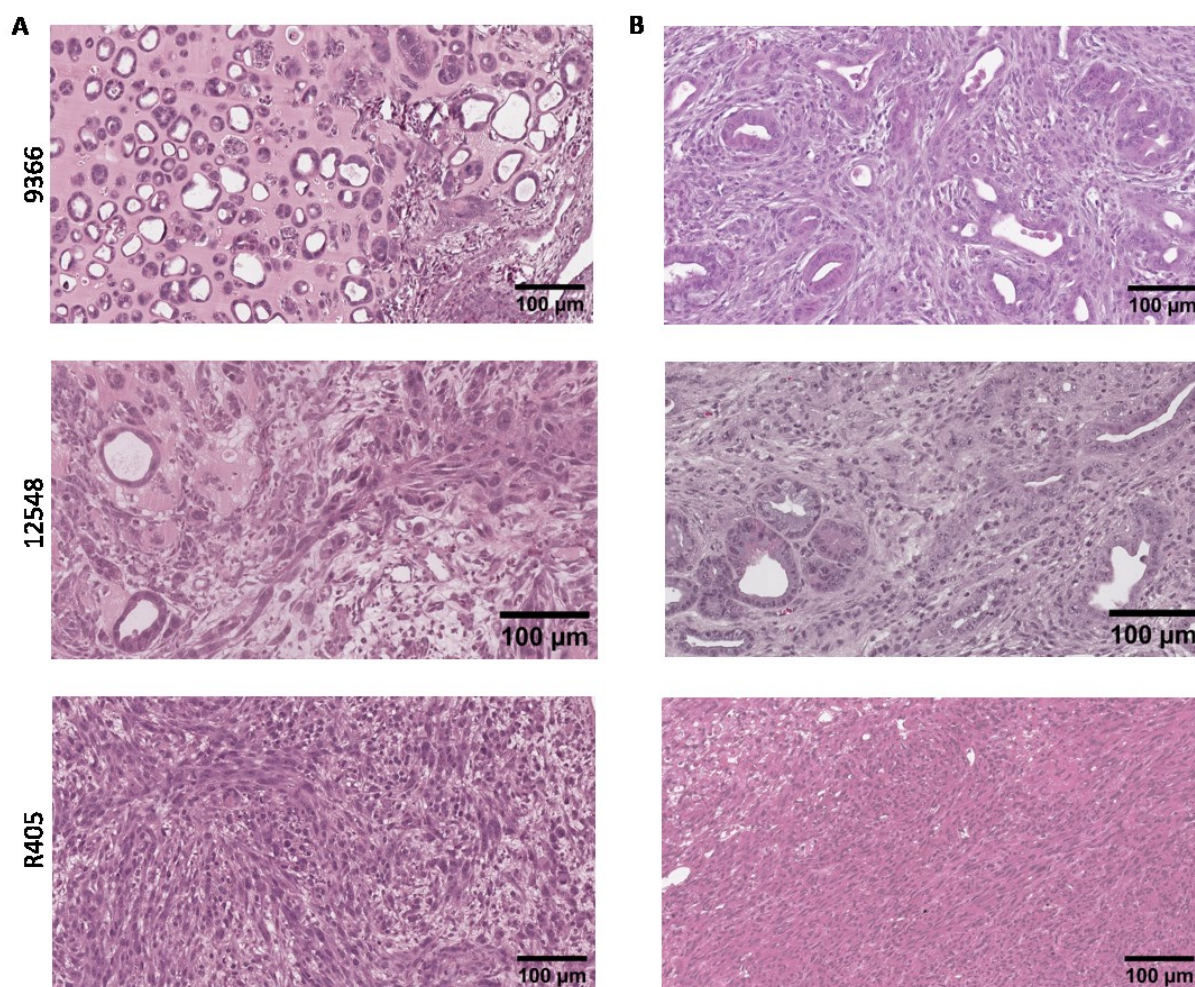


Figure 11: Comparison of the histomorphological features in CAM and endogenous mouse tumors.

A) Representative H&E stained 9366, 12548, and R405 CAM tumor sections under 40X magnification, B) Representative H&E stained 9366, 12548, and R405 endogenous mouse tumor sections under 40X magnification.

neoplastic growth, whereas moderate infiltration was observed around the moderately differentiated ductal neoplastic growth. However, in the endogenous mouse tumor, extensive desmoplastic stroma was observed. The cell line R405, representing the basal PDAC subtype, showed poorly differentiated neoplastic growth with high stromal infiltration in the CAM as well as in the endogenous mouse tumors. Characteristic histomorphological features of each PDAC subtype were observed in the CAM

xenografts of the cell lines 9366, 12548, and R405, representing the classical, quasi-mesenchymal, and basal PDAC subtypes. Also, the comparison with the histology of the respective endogenous mouse tumors for each cell line revealed similarity to a certain extent.

5.2.2 Characterization of tumor proliferation of KPC mouse cell lines-derived CAM xenografts

CAM xenograft tissue sections were obtained from paraffin-embedded blocks, and immunohistochemical staining was performed for Ki 67, a well-known marker for proliferation, to characterize *in ovo* tumor proliferation and growth (Figure 12A). Ki 67-stained slides were then scanned using the Aperio Versa 8 digital scanner and analyzed using the Aperio Image Scope software (v.12.3.3.5048).

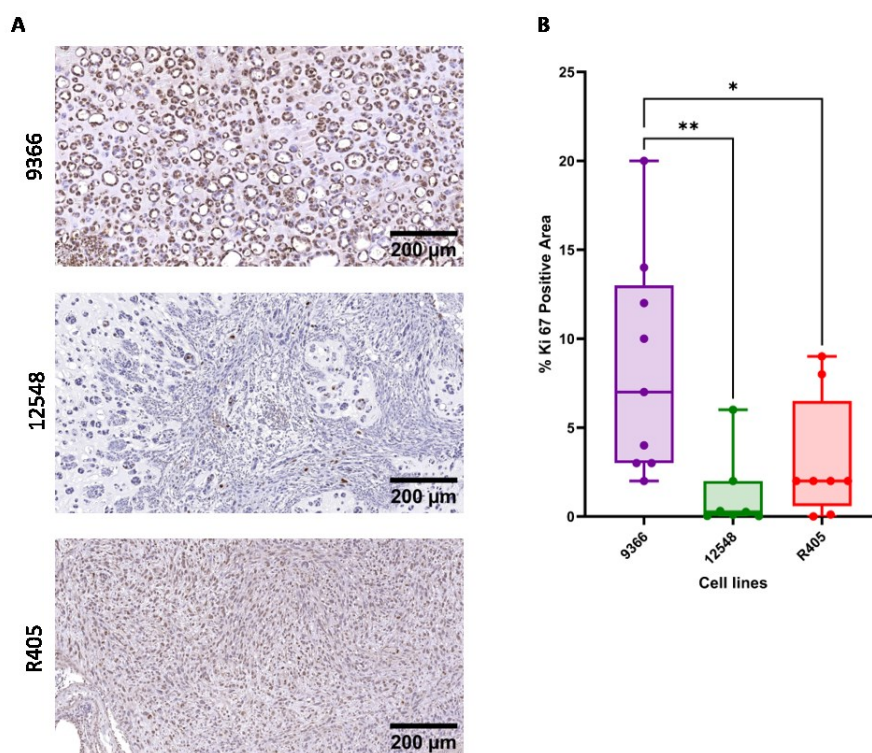


Figure 12: Characterization of tumor proliferation in CAM xenografts.

A) Representative Ki 67-stained 9366, 12548, and R405 CAM xenograft sections under 20X magnification, B) Quantification of the percentage Ki 67 positive area of 9366 (N = 9), 12548 (N = 8), and R405 (N = 8) CAM xenografts. The percentage Ki 67 positive area was calculated by dividing the Ki 67 positive pixels by the total number of pixels. The data were collected from three independent experiments (n = 3), and the Kruskal-Wallis test was performed to evaluate the statistical significance (*p-value = 0.0324, (**p-value = 0.0017).

For the analysis, the tumor area was first annotated on the digital scans of the CAM xenografts. Then, using the Positive Pixel Count v9 algorithm, Ki 67 staining was quantified. Using the formula,

$$\frac{\text{Ki 67 positive pixels}}{\text{Total pixels}} \times 100\%$$

The percentage Ki 67 positive area was calculated. According to the percentage Ki 67 positive area, cell line 9366, representing the classical PDAC subtype, showed the highest *in ovo* proliferation, which is statistically significant compared to the cell lines R405, representing the basal PDAC subtype, and 12548 representing the quasi-mesenchymal PDAC subtype (Figure 12B). No statistically significant differences in *in ovo* proliferation were observed between the cell lines 12548 and R405 (Figure 12B). MTT assay was performed to check the *in vitro* proliferation of the cell lines, and the viability was measured every 24 hours for five days. Proliferation rates were calculated by normalizing the Day 1-Day 5 absorbances to the Day 0 absorbance. In contrast to the *in ovo* proliferation, no statistically significant differences were observed in the *in vitro* proliferation of the cell lines (Figure 13).

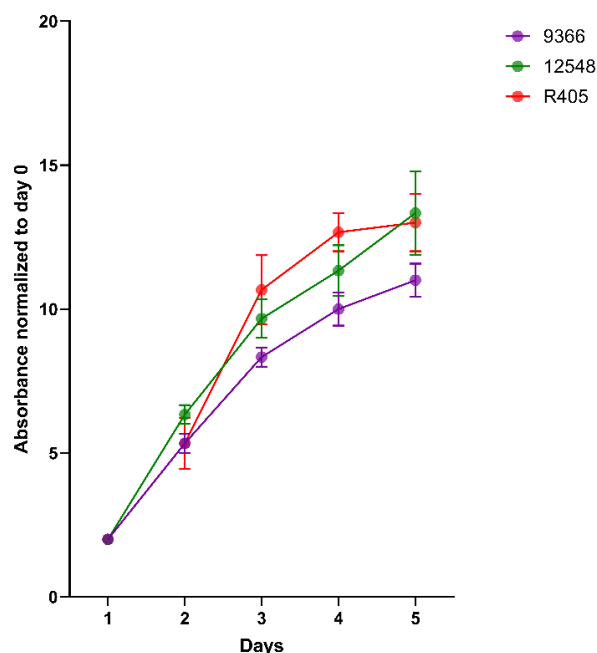


Figure 13: *In vitro* proliferation of the cell lines 9366, 12548, and R405.

In vitro proliferation was measured every 24 hours for five days and calculated by normalizing the Day 1-Day 5 absorbances to Day 0 absorbance. The data were collected from three independent experiments ($n = 3$, $N = 6$), and the Kruskal-Wallis test was performed to evaluate the statistical significance. The mean and SEM are shown in the graph.

5.2.3 Evaluation of metastatic dissemination of KPC mouse cell lines using the CAM model

Murine-specific *BI* qPCR was established to detect murine cells that metastasized to chick embryo organs. The sensitivity and efficiency of the *BI* qPCR in detecting murine DNA were evaluated by amplifying murine DNA in an increasing fold (0.0001-100 ng) by using *BI* primers. With increasing murine DNA in chick embryo organs, a steady decrease in mean CT values was observed. In addition, *BI* qPCR was sensitive enough to detect murine DNA as low as 0.0001 ng (Figure 14A). The specificity of the *BI* qPCR was evaluated by amplifying chick embryo DNA in an increasing fold (0.0001-100 ng) by using *BI* primers. In contrast to murine *BI* qPCR, with an increasing fold of chicken DNA, a steady decrease in mean CT was not observed, and a weak signal was observed only in the presence of chicken DNA as high as 100 ng (Figure 14B).

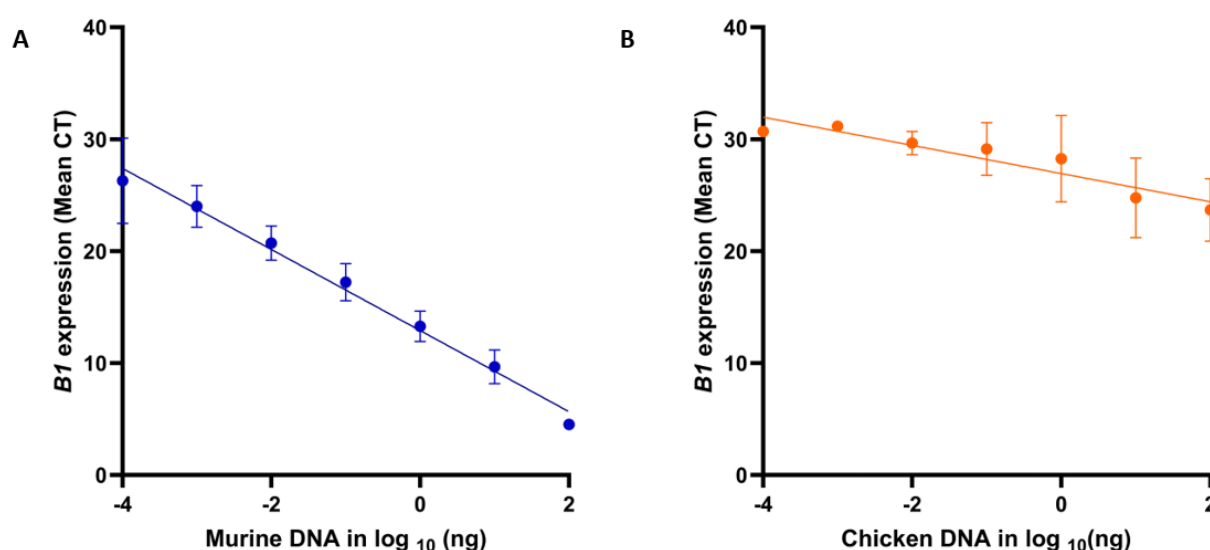


Figure 14: *BI* qPCR establishment.

A) Determination of *BI* qPCR sensitivity to detect murine DNA in chick embryo organs ($n = 3$, $N = 6$), B) Determination of *BI* qPCR specificity in detecting murine and chicken DNA. The data were collected from three independent experiments ($n = 3$, $N = 6$). The mean and SEM are shown in the graph.

To determine the metastatic potential of the cell lines 9366, 12548, and R405 by *BI* qPCR, chick embryo organs, selectively the brain, heart, and liver, were collected on EDD 14. Genomic DNA isolation and *BI* qPCR were performed to amplify the *BI* sequences in the mouse DNA that could be found in the chick embryo organs due to metastatic dissemination. The expression of the *BI* sequence was normalized to control chick embryo DNA, in which no transplantation was performed.

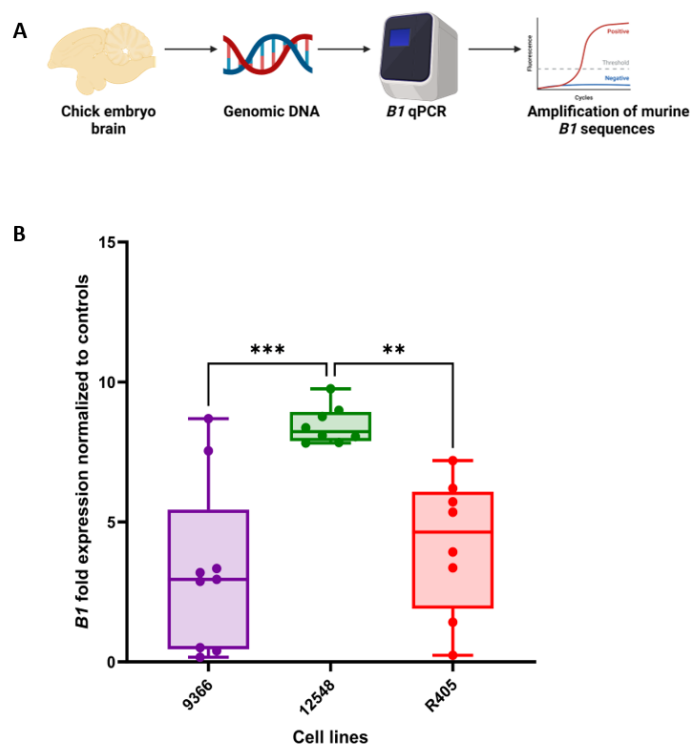


Figure 15: Metastatic dissemination in the chick embryo brain.

A) Schematic illustration of metastatic dissemination determination of the cell lines 9366, 12548, and R405 in chick embryo brain using *B1* qPCR, B) Quantification of metastatic dissemination of the cell lines 9366 (N = 9), 12548 (N = 8), and R405 (N = 8) normalized to controls. The data were collected from three independent experiments (n = 3), and the Kruskal-Wallis test was performed to evaluate the statistical significance (**p-value = 0.0039, (***)p-value = 0.0005).

Based on the amplification of *B1* sequences in chick embryo brain genomic DNA, cell line 12548, representing the quasi-mesenchymal subtype, showed the highest metastatic dissemination, which is statistically significant compared to cell lines 9366 and R405. No statistically significant difference was observed between cell lines 9366 and R405, representing the classical and basal PDAC subtypes in metastatic dissemination (Figure 15).

Based on the amplification of *B1* sequences in chick embryo heart genomic DNA, metastatic dissemination was observed for cell lines 9366, 12548, and R405. However, no statistical significance was observed in the metastatic dissemination of the cell lines in chick embryo heart (Figure 16).

Based on the amplification of *B1* sequences in chick embryo liver genomic DNA, metastatic dissemination was observed for cell lines 9366, 12548, and R405. The cell line R405, representing the basal PDAC subtype, showed the highest metastatic dissemination in the chick embryo liver. A

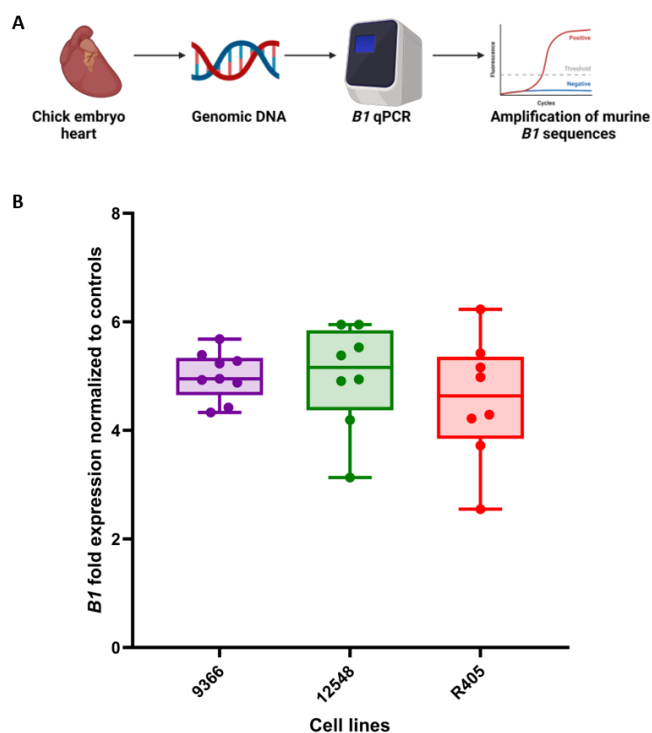


Figure 16: Metastatic dissemination in the chick embryo heart.

A) Schematic illustration of metastatic dissemination determination of the cell lines 9366, 12548, and R405 in chick embryo heart using *B1* qPCR, B) Quantification of metastatic dissemination of the cell lines 9366 (N = 9), 12548 (N = 8), and R405 (N = 8) normalized to controls. The data were collected from three independent experiments (n = 3), and the Kruskal-Wallis test was performed to evaluate the statistical significance.

statistically significant difference was observed between the cell lines 12548 and R405 in metastatic dissemination in the chick embryo liver (Figure 17).

During metastatic dissemination, the tumor cells disseminate from the primary tumor, reach the underlying CAM, and subsequently metastasize to distant organs. During this process, disseminated tumor cells migrate in a directed manner from the primary tumor toward the CAM. Hence, the *in vitro* migration potential of cell lines 9366, 12548, and R405 was analyzed by performing the scratch assay. In a confluent monolayer of the cells, a scratch was made, and the closure of the scratch was documented at 0, 4, 8, and 24 hours by imaging (Figure 18A). Cell lines 9366 and 12548 showed a collective mode of migration, as a uniform sheet of epithelial cells maintaining contact between the adjacent cells. Though cell line 12548 showed a mixed population of epithelial and mesenchymal leading cells during scratch closure, an epithelial mode of collective migration was observed. The cell line R405 demonstrated a mesenchymal mode of migration as single cells with clearly distinguishable boundaries.

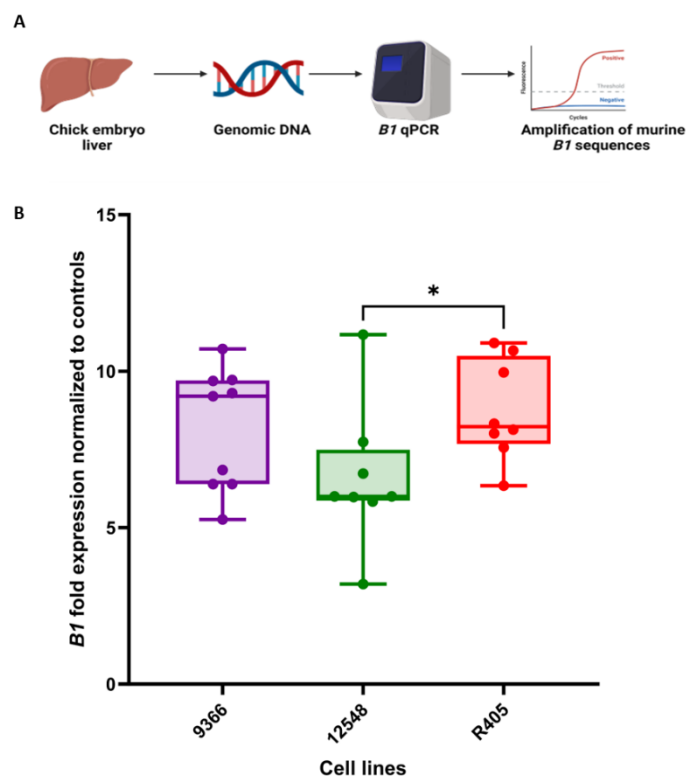


Figure 17: Metastatic dissemination in chick embryo liver.

A) Schematic illustration of metastatic dissemination determination of the cell lines 9366, 12548, and R405 in chick embryo liver using *B1* qPCR, B) Quantification of metastatic dissemination of the cell lines 9366 (N = 9), 12548 (N = 8), and R405 (N = 8) normalized to controls. The data were collected from three independent experiments (n = 3), and the Kruskal-Wallis test was performed to evaluate the statistical significance (*p-value = 0.0296).

The *in vitro* migration potential of the cell lines was quantified as a percentage of wound area on the phase contrast images obtained using Image J wound healing size tool plugin software (Figure 18B). Cell lines 12548 and R405 showed the same migratory potential, whereas cell line 9366 showed the lowest migratory potential. However, there were no significant differences observed in the *in vitro* migration potential of the cell lines.

5.2.4 Characterization of the stroma in CAM xenografts

The histological analysis of 9366, 12548, and R405 CAM xenografts using H&E-stained sections showed the infiltration of stromal cells from the CAM (Figure 19). Different degrees of infiltration were

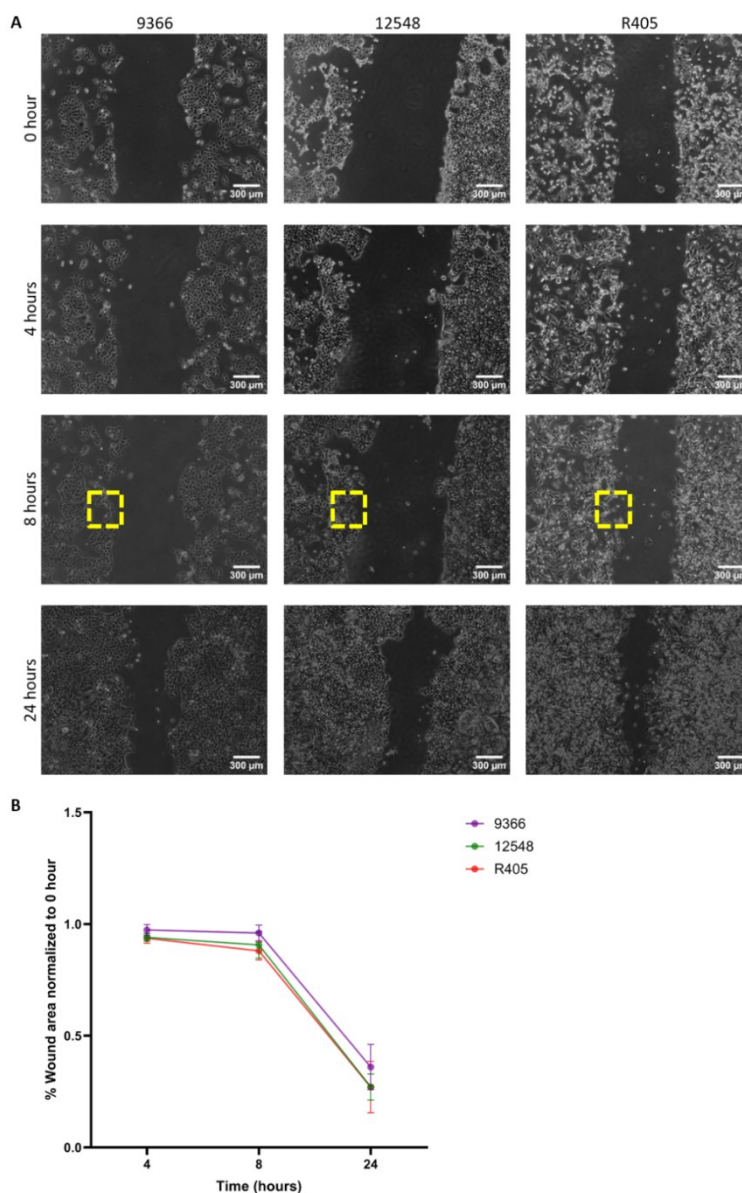


Figure 18: *In vitro* migration potential of the cell lines.

A) Representative phase contrast images of the scratches in 9366, 12548, and R405 monolayers at 0, 4, 8, and 24 hours, B) Quantification of the percentage wound area of 9366, 12548, and R405 monolayers normalized to 0 hours. The data were collected from three independent experiments ($n = 3$, $N = 6$), and the Two-way ANOVA test was performed to evaluate the statistical significance. The mean and SEM are shown in the graph.

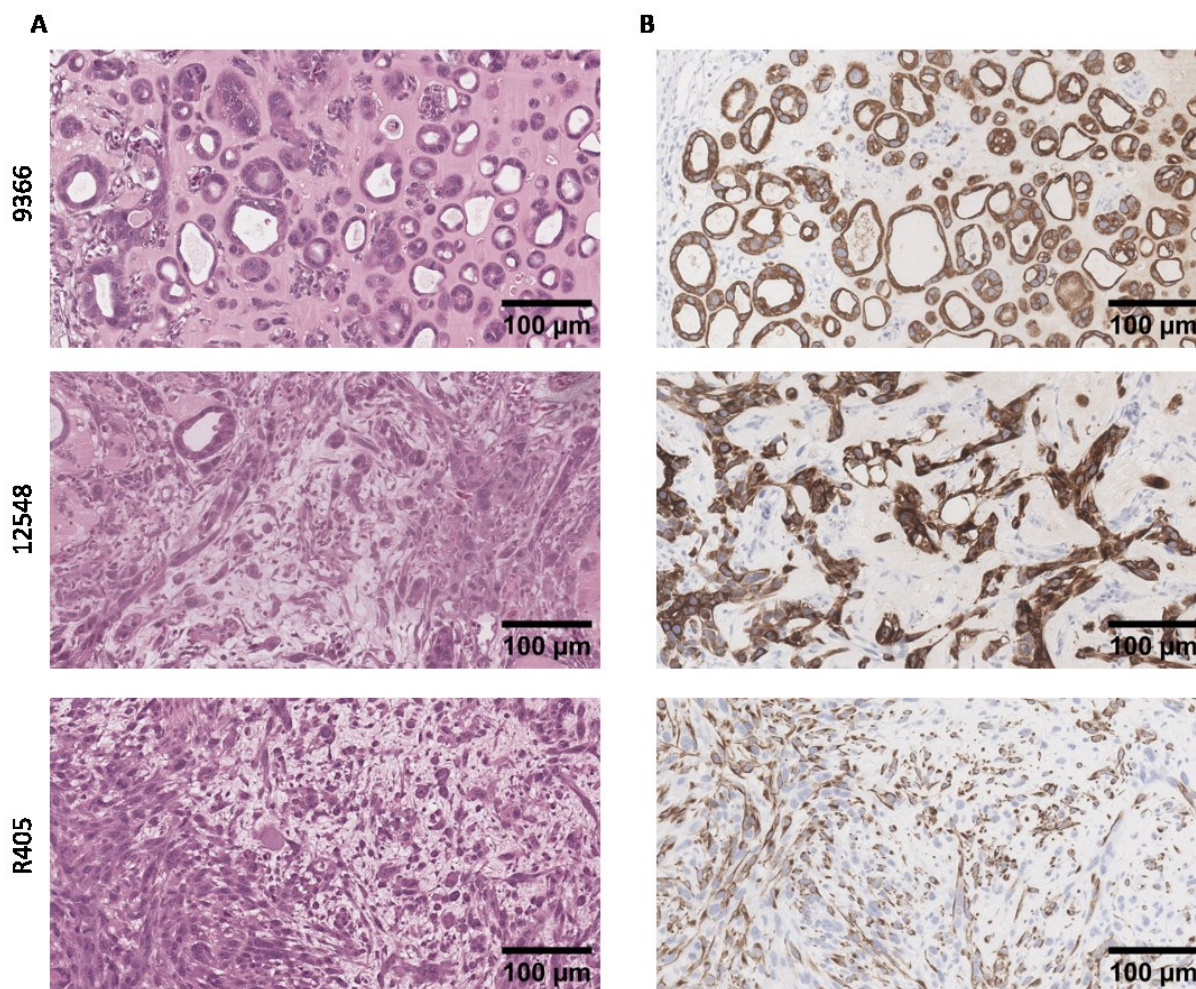


Figure 19: Stromal infiltration in CAM xenografts.

A) Representative H&E-stained 9366, 12548, and R405 CAM xenograft sections showing stromal infiltration under 40X magnification, B) Representative CK 19-stained 9366, 12548, and R405 CAM xenograft sections showing CK 19 negative stromal cells under 40X magnification.

observed in the H&E-stained CAM xenografts derived from the cell lines 9366, 12548, and R405, representing the epithelial, quasi-mesenchymal, and basal subtypes. Minimal stromal infiltration was observed in the 9366 CAM xenografts surrounding a few tumor cells growing in a ductal pattern. In the 12548 CAM xenografts, stromal infiltration was observed around the tumor cells, growing in ductal and striated patterns. In the R405 CAM xenografts, more stromal infiltration was observed along with the striated pattern of tumor growth. To confirm the stromal infiltration from the host, immunohistochemical staining for murine-specific CK 19, a PDAC marker, was performed on the CAM xenografts (Figure 19B). Tumor cells in the CAM xenografts showed positive CK 19 staining, whereas the stroma showed

negative CK 19 staining, confirming the stromal infiltration from the host. Histologically, PDAC is characterized by a desmoplastic stroma composed of several distinct cellular and ECM components. A major cellular component of the desmoplastic stroma of the PDAC is CAFs, which can be characterized by a pan-CAF marker, Vimentin (Elyada et al., 2019). Hence, the CAM xenografts from cell lines 9366, 12548, and R405 have been stained for chicken-specific Vimentin. For this purpose, CAM xenograft tissue sections were obtained from paraffin-embedded blocks of CAM primary tumors, and immunohistochemical staining for chicken-specific Vimentin was performed. Vimentin-stained CAM xenografts confirmed the presence of CAFs in the CAM xenografts from cell lines 9366, 12548, and R405 (Figure 20A).

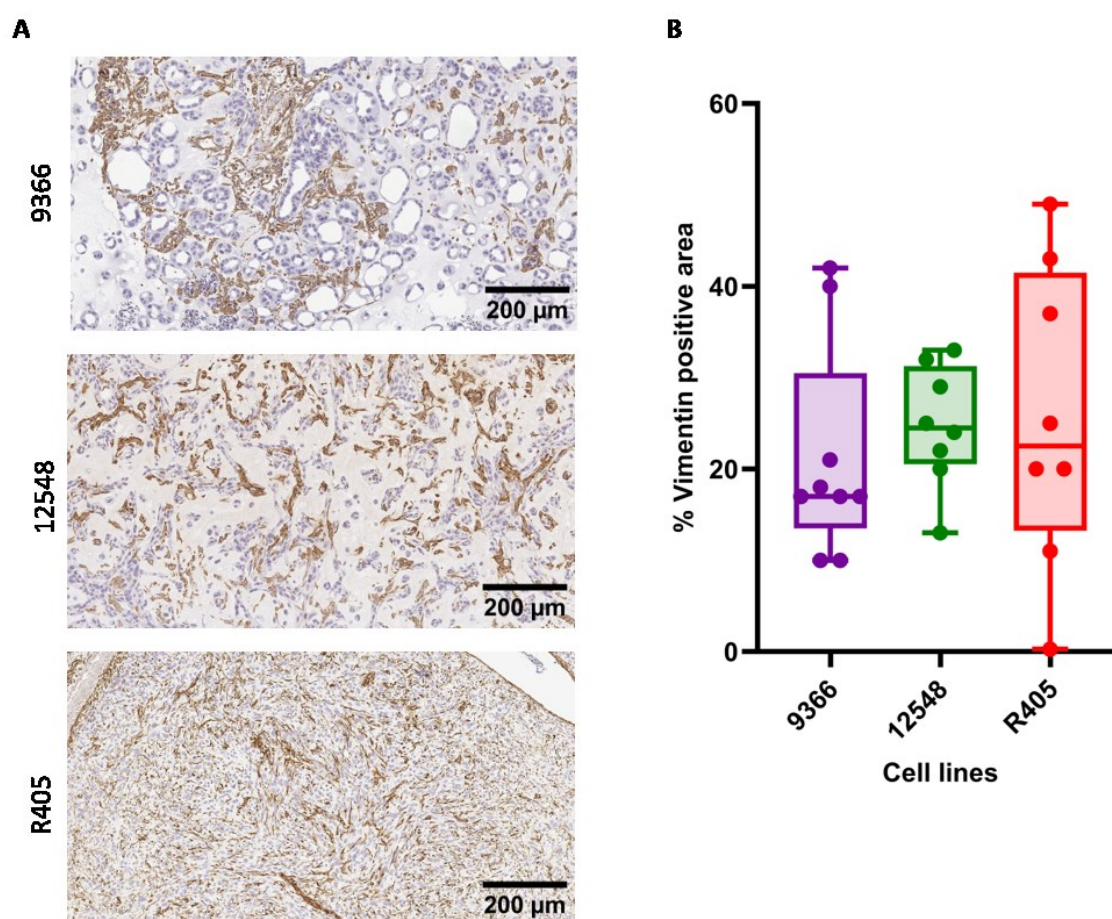


Figure 20: Vimentin staining showing the pan-CAF population in CAM xenografts.

A) Representative Vimentin-stained 9366, 12548, and R405 CAM xenograft sections under 20X magnification, B) Quantification of the percentage Vimentin positive area of 9366 (N = 9), 12548 (N = 8), and R405 (N = 8) CAM xenografts. The percentage of Vimentin positive area was calculated by dividing the number of Vimentin positive pixels by the total number of pixels. The data were collected from three independent experiments (n = 3), and the Kruskal-Wallis test was performed to evaluate the statistical significance.

In order to determine the differences in the CAF infiltration in the CAM xenografts derived from the cell lines 9366, 12548, and R405, immunohistochemical quantification of Vimentin was performed. For this purpose, Vimentin-stained CAM xenograft sections were scanned using the Aperio Versa 8 digital scanner and analyzed using the Aperio Image Scope software (v.12.3.3.5048).

For the analysis, first, the tumor area was annotated on the digital scans of the CAM xenografts. Then, using the Positive Pixel Count v9 algorithm, Vimentin staining was quantified. Using the formula,

$$\frac{\text{Vimentin positive pixels}}{\text{Total pixels}} \times 100\%$$

percentage Vimentin positive area was calculated. According to the percentage Vimentin positive area, there were no statistically significant differences observed in the pan-CAF population between the cell lines (Figure 20B).

Studies have shown that activated CAFs that express α -SMA are involved in ECM remodeling and, thereby, in the desmoplastic stroma of PDAC (Han et al., 2020). Hence, to confirm the presence of α -SMA expressing CAFs and their infiltration into the tumor, CAM xenografts were co-stained for CK19 and α -SMA. Immunofluorescence imaging of the co-stained CAM xenografts showed CK 19 positive, α -SMA negative tumor cells and infiltrating α -SMA positive, CK 19 negative CAFs (Figure 21). Immunofluorescence microscopic analysis of CK 19 and α -SMA co-stained 9366, 12548, and R405 CAM xenografts revealed differences in the CK 19 intensity and the infiltration of α -SMA positive CAFs. 9366 CAM xenografts representing the classical PDAC subtype showed a strong CK 19 positive tumor cell population with minimal infiltration of α -SMA positive CAFs. 12548 CAM xenografts representing the quasi-mesenchymal PDAC subtype showed a mixed tumor cell population composed of strong CK 19 positive epithelial tumor cells and weak CK 19 positive mesenchymal cells. In addition, infiltration of α -SMA positive CAFs was observed surrounding both tumor populations. R405 CAM xenografts representing the basal PDAC subtype showed weak CK 19 positive tumor cells infiltrated by α -SMA positive CAFs. Compared to 9366 CAM xenografts, more α -SMA positive CAF infiltration was observed in the 12548 and R405 CAM xenografts (Figure 21).

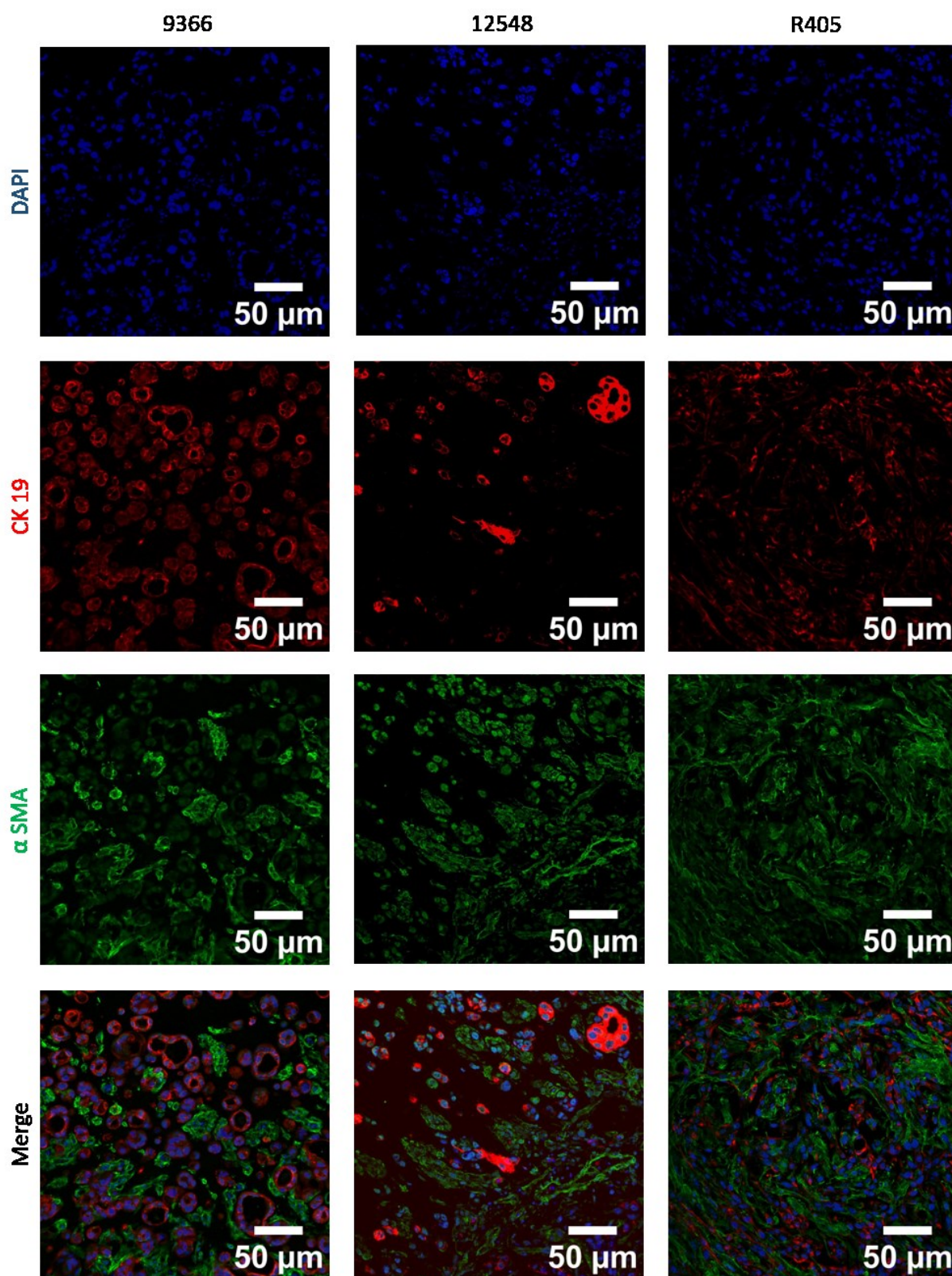


Figure 21: α -SMA and CK 19 co-staining showing the presence of α -SMA positive fibroblast infiltration in CAM xenografts.

Immunofluorescence microscopic analysis of representative α -SMA and CK 19 co-stained 9366, 12548, and R405 CAM xenograft sections shows the infiltration of α -SMA positive CAFs under 40X magnification.

In the desmoplastic PDAC stroma, fibrillar collagens such as Collage type I and III are the abundant acellular components that constitute a significant part of the ECM, thereby involved in PDAC progression (Maneshi et al., 2021). Sirius red staining was performed on the CAM xenografts to determine the fibrillar collagen deposition. For this purpose, CAM xenograft tissue sections were obtained from paraffin-embedded blocks of CAM primary tumors, and Sirius red staining was performed (Figure 22A). Sirius red-stained slides were then scanned using the Aperio Versa 8 digital scanner, and the images were documented. Using a DMI8 Leica Thunder microscope, polarized imaging of Sirius red-stained slides was performed, and the birefringence was measured. Positive pixels in each tissue section were quantified using Image J software, and the percentage of Sirius red positive area was calculated.

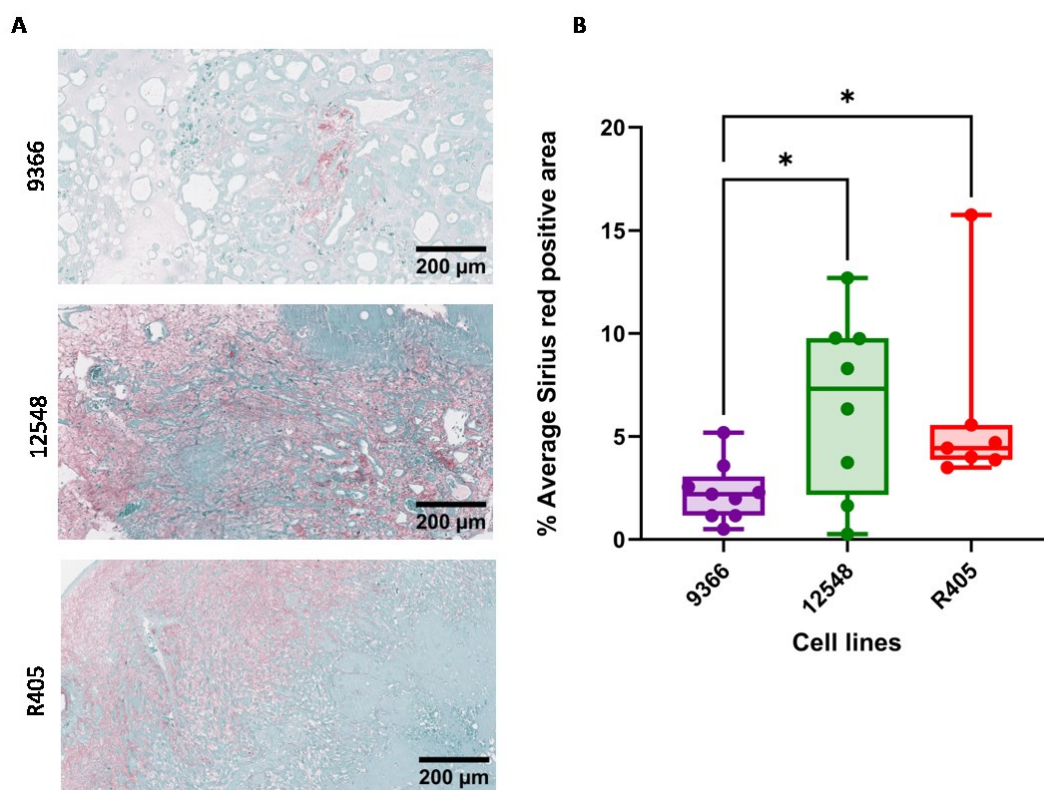


Figure 22: Sirius red staining showing fibrillar collagen deposition in CAM xenografts.

A) Representative Sirius red-stained 9366, 12548, and R405 CAM xenograft sections under 20X magnification, B) Quantification of the percentage Sirius red positive area of 9366 (N = 9), 12548 (N = 8), and R405 (N = 7) CAM xenografts. The percentage of Sirius red positive area was calculated by dividing the number of Sirius red positive pixels by the total number of pixels. The data were collected from three independent experiments (n = 3), and the Kruskal-Wallis test was performed to evaluate the statistical significance (*p-value = 0.0210, (*p-value = 0.0203).

Using the formula,

$$\frac{\text{Sirius red positive pixels}}{\text{Total pixels}} \times 100\%$$

percentage Sirius red positive area was calculated (Figure 22B). According to the percentage of Sirius red positive area, high fibrillar collagen deposition was observed in the CAM xenografts derived from the cell lines 12548 and R405, representing the quasi-mesenchymal and basal PDAC subtypes, respectively. The lowest fibrillar collagen deposition was observed in the TME of the CAM xenografts derived from cell line 9366, representing the classical PDAC subtype. Statistically significant differences were observed in the fibrillar collagen deposition between the 9366 CAM xenografts and the 12548 CAM xenografts. Similarly, statistically significant differences were observed in fibrillar collagen deposition between the 9366 CAM xenografts and the R405 CAM xenografts. However, no statistically significant difference in fibrillar collagen deposition was observed between the 12548 and R405 CAM xenografts.

Similar to fibrillar collagens, hyaluronan is another major component of the desmoplastic stroma of PDAC, which is involved in PDAC progression. Hence, immunohistochemical staining of hyaluronan binding protein (HABP) was performed (Figure 23A) on the CAM xenografts. For this purpose, CAM xenograft tissue sections were obtained from paraffin-embedded blocks of CAM primary tumors, and HABP staining was performed. HABP-stained slides were then scanned and analyzed using the Aperio Versa 8 digital scanner and analyzed using the Aperio Image Scope software (v.12.3.3.5048). For the analysis, first, the tumor area was annotated on the digital scans of the CAM xenografts. Then, using the Positive Pixel Count v9 algorithm, HABP staining was quantified. Using the formula,

$$\frac{\text{HABP positive pixels}}{\text{Total pixels}} \times 100\%$$

percentage HABP positive area was calculated (Figure 23B). According to the percentage HABP positive area, high hyaluronan deposition was observed in the CAM xenografts derived from the cell lines 12548 and R405, representing the quasi-mesenchymal and basal PDAC subtypes, respectively.

The lowest hyaluronan deposition was observed in the 9366 CAM xenografts. Statistically significant differences were observed in the hyaluronan deposition between the 9366 CAM xenografts and the 12548 CAM xenografts. However, there was no statistically significant difference in hyaluronan deposition observed between the 9366 and R405 CAM xenografts. Similarly, no statistically significant difference in hyaluronan deposition was observed between the 12548 R405 CAM xenografts.

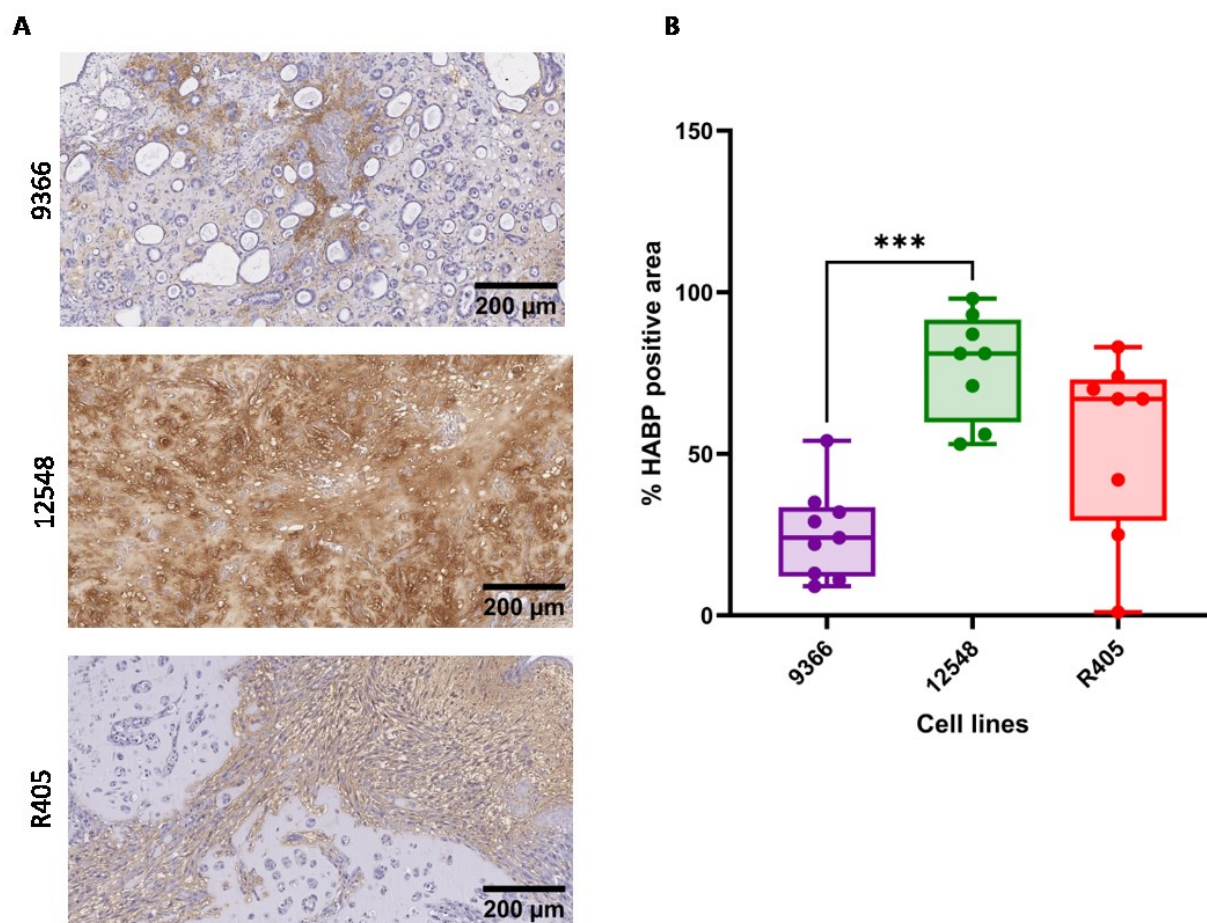


Figure 23: HABP staining showing the hyaluronan deposition in CAM xenografts.

A) Representative HABP-stained 9366, 12548, and R405 CAM xenograft sections under 20X magnification, B) Quantification of the percentage HABP positive area of 9366 (N = 9), 12548 (N = 8), and R405 (N = 8) CAM xenografts. The percentage of HABP positive area was calculated by dividing the number of HABP positive pixels by the total number of pixels. The data were collected from three independent experiments (n = 3), and the Kruskal-Wallis test was performed to evaluate the statistical significance (***) (p-value = 0.0003).

5.3 Establishment of CAM as a patient-derived xenograft (PDX) model

The study aimed to establish the CAM as an alternative PDX model using PDOs and to characterize the tumor growth, invasion, metastasis, and tumor microenvironment. For this purpose, first the PDOs were phenotypically, genetically, and transcriptomically characterized.

5.3.1 Morphological characterization of the selected PDOs

PDOs were isolated from endoscopic ultrasound-guided fine needle aspirations/biopsies (EUS-FNA/B) or surgical resections. Once the PDOs were successfully expanded *in vitro*, *KRAS* mutational status was determined by Sanger sequencing. Wild-type and tumor organoids were identified based on the mutational status of *KRAS*. This study used well-established PDOs characterized as tumor organoids due to either *KRAS* G12D or *KRAS* G12V mutations, selectively B188, B250, B290, and B339 (Table 18).

Table 18: Sample of origin and *KRAS* mutational status of selected PDOs

| PDOs | Sample of origin | <i>KRAS</i> mutation |
|------|--------------------|----------------------|
| B188 | Fine-needle biopsy | G12D |
| B250 | Surgical resection | G12D |
| B290 | Surgical resection | G12V |
| B339 | Surgical resection | G12D |

Selected PDOs were morphologically characterized by phase contrast microscope imaging. Morphologically, the PDO lines B250, B290, and B339 appeared as hollow cystic organoids forming a lumen with a polarized epithelial lining. In contrast, the PDO line B188 appeared as filled lumen organoids (Figure 24).

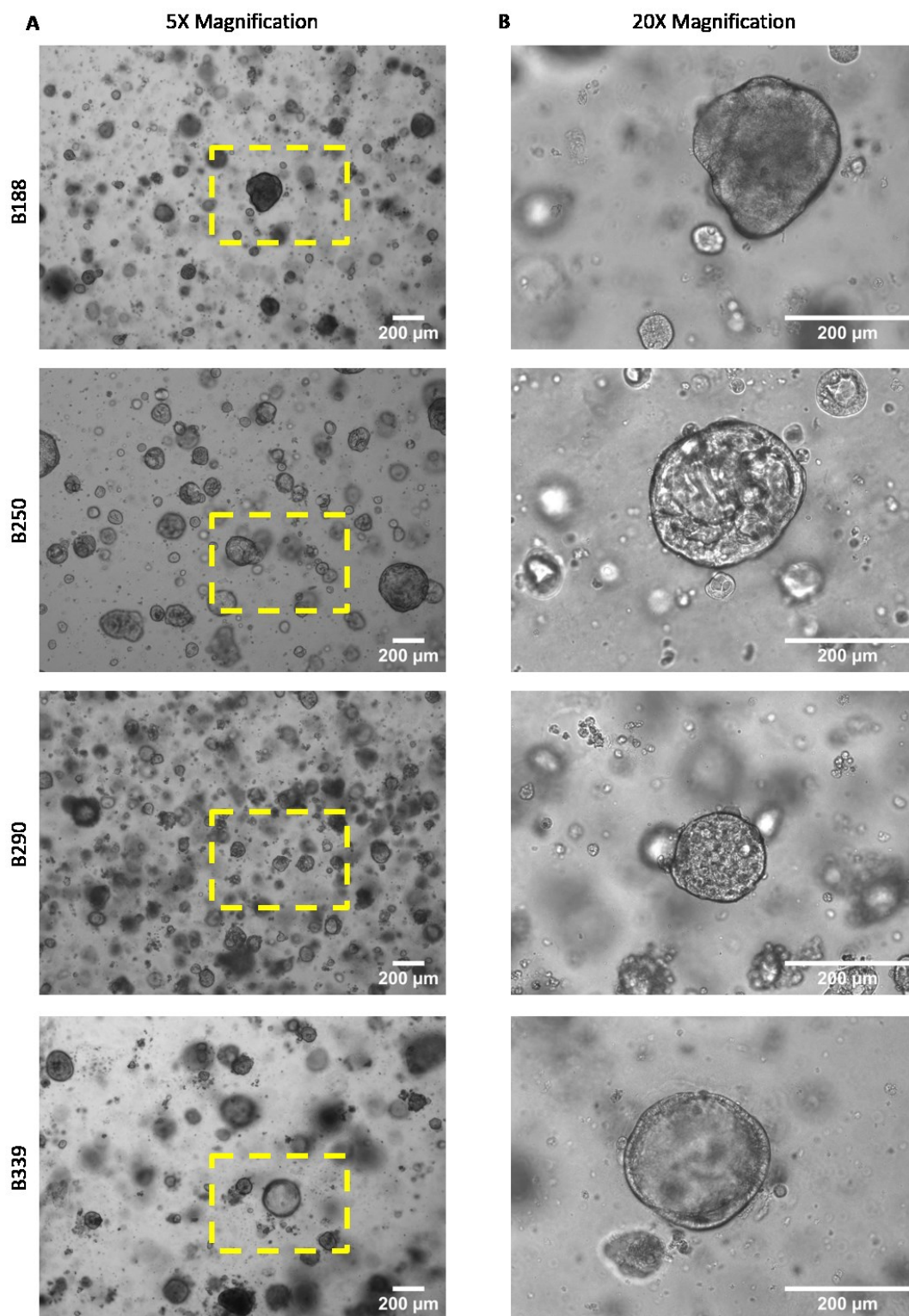


Figure 24: Morphological characterization of PDOs by phase contrast microscopy.

Phase contrast images of the PDOs. A) 5X magnification, B) 20X magnification of the highlighted field shows the PDO lines B188, B250, B290, and B339, respectively.

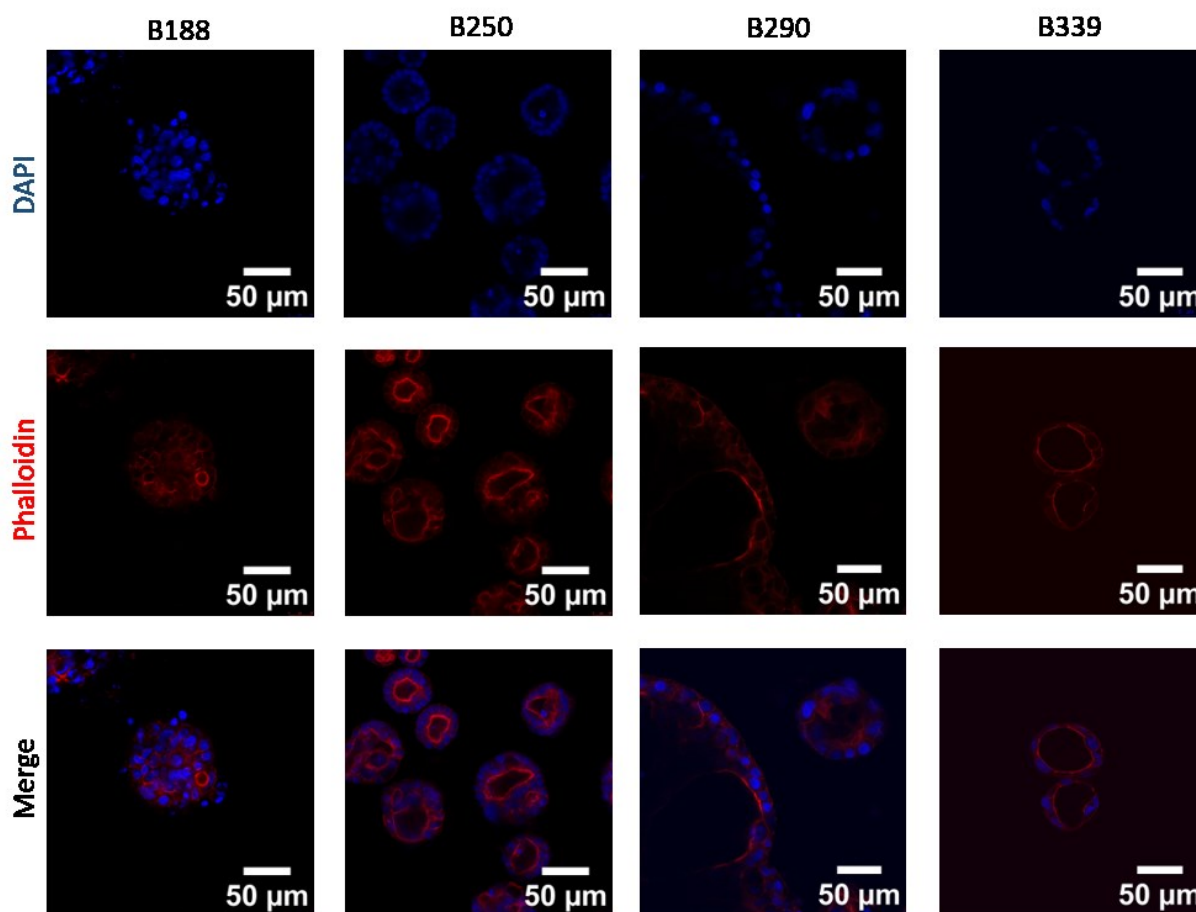


Figure 25: Morphological characterization of PDOs by F-actin staining.

Immunofluorescence staining of F-actin in the PDOs B188, B250, B290, and B339 under 40X magnification. The image panel shows the nuclei staining (DAPI), F-actin staining (Phalloidin), and the merged images. Distinct F-actin organization and cytoskeleton structure of the hollow lumen PDOs B250, B290, and B339, as well as filled lumen PDOs B188, were observed.

Further morphological characterization was done through the visualization of the cytoskeleton structure of the organoids by staining for F-actin filaments. As observed by the phase contrast microscopy, the PDO lines B250, B290, and B339 appeared as hollow lumen organoids in which strong Phalloidin staining was observed facing the lumen, indicating the rich F-actin polymerization (Figure 25). In contrast, filled lumen PDO line B188 showed Phalloidin-rich areas between the cells that fill the lumen (Figure 25).

5.3.2 Mutation profile of the PDOs

Whole exome sequencing was performed to check the mutation profiles of the PDOs, and the 30 most frequently mutated genes in PDAC according to the cBioPortal platform (<https://www.cbioportal.org/>) were checked (Figure 26). All the PDO lines have a missense mutation of *KRAS*, the only mutation found in the PDO line B188. In addition to *KRAS*, a missense mutation in *LRP1B* and a nonsense mutation in the *RYR2* genes were found in the PDO line B339. The PDO line B290 has the most mutations, which include missense mutations of the genes *KRAS*, *TP53*, *TTN*, *KMT2D*, *SYNE1*, *MUC16*, and *CDH10*. The PDO line B250 has the 2nd most mutations, which include missense mutations of *KRAS* and *TP53*, both frameshift insertion and inframe insertion of *CDKN2A*, and nonsense mutations of *GLI3*.

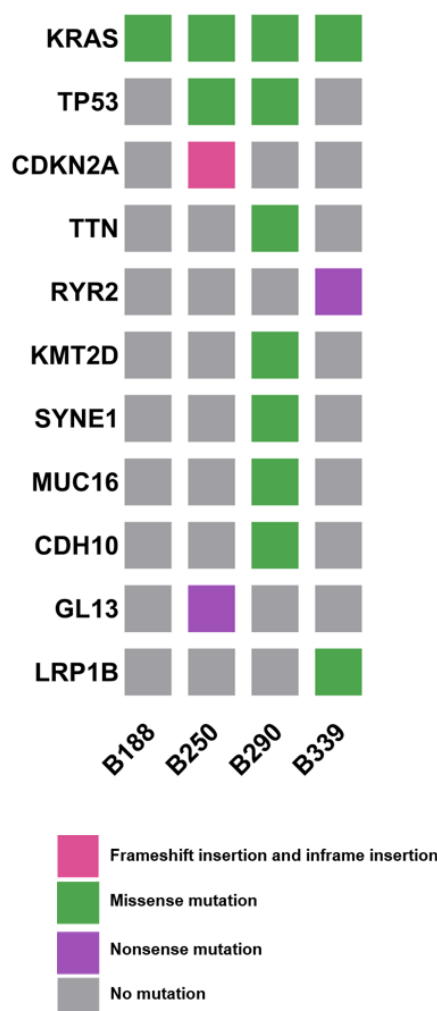


Figure 26: Mutation profile of the PDO lines.

The mutation profile of the PDO lines according to the 30 most frequently mutated genes in PDAC. The data were retrieved from cBioPortal.

5.3.3 Transcriptomic characterization of the PDO lines

The underlying molecular features of the PDO lines attributable to the well-known PDAC subtypes were investigated similarly to the endogenous mouse-derived cell lines. For this purpose, on the bulk RNA seq data from the PDO lines B188, B250, B290, and B339, the PurIST (purity-independent subtyping of tumors) score was applied.

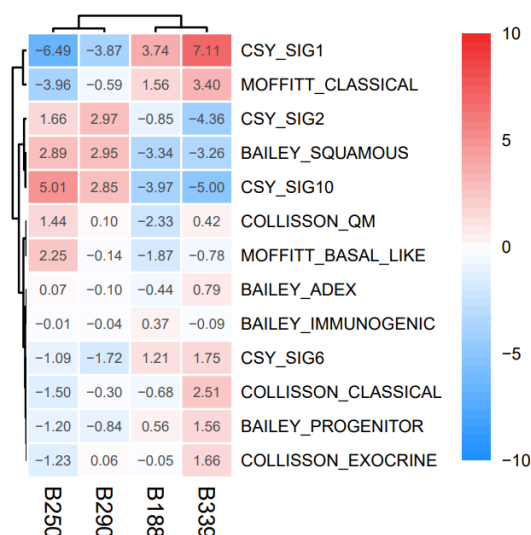


Figure 27: Transcriptomic characterization of PDOs.

By applying the PurIST single sample classifier based on the well-known PDAC subtyping schemas, the PDO lines B188, B250, B290, and B339 were transcriptomically characterized.

When the PurIST single sample classifier was applied, the PDO line B250 scored high for quasi-mesenchymal molecular signatures of Collisson's, basal molecular signatures of Moffitt's, squamous molecular signatures of Bailey's, and basal molecular signatures of CSY's PDAC subtyping (Figure 27). Similarly, the PDO line B290 scored high for squamous molecular signatures of Bailey's and basal molecular signatures of CSY's PDAC subtyping. Hence, the PDO lines B250 and B290 were transcriptomically characterized as basal-like PDAC subtypes. On the other hand, the PDO line B188 scored high for classical molecular signatures of Moffitt's and CSY's PDAC subtyping. Similarly, the PDO line B339 scored high for classical molecular signatures of Collisson's and Moffitt's PDAC subtyping. B339 also scored high for the classical molecular signatures of CSY's and Bailey's PDAC subtyping. Hence, the PDO lines B188 and B339 were transcriptomically characterized as classical-like PDAC subtypes.

5.3.4 Establishment of the CAM workflow as an alternative PDX model using PDOs.

PDOs were isolated from endoscopic ultrasound-guided fine needle aspirations/biopsies (EUS-FNA/B), and surgical resections, expanded, and quality control were performed. Once the PDO lines were established, the morphological and transcriptomic characterization of the PDO lines was done. For successful transplantation and tumor growth, the eggs were prepared carefully. The prick made on the eggshell on EDD 4 allowed the CAM to detach from the eggshell membrane, thereby facilitating the growth of CAM. The second opening on the eggshell on EDD 7 allowed access to a larger area of CAM for transplantation. On EDD 9, when the CAM was completely grown, PDOs embedded in Matrigel domes were transplanted. To transplant organoids of the same cell number for each PDO line, growth rates of the PDO lines were determined by the CellTiter-Glo® 3D Cell Viability Assay over ten days (Figure 28). The PDO line B250 showed the highest growth rate, whereas the PDO line B188 showed the lowest growth rate. Except for the PDO lines B250 and B188, no significant differences were observed between the other PDO lines. To optimize the seeding density of the PDO lines, Matrigel-embedded organoids containing different numbers of cells were transplanted on CAM, and tumor take rates were documented (Figure 29). For this purpose, the PDO lines B250 and B188, with the highest and lowest growth rates, were used. For the transplantation, single cells were isolated from organoids and seeded according to their growth rates to achieve 25×10^3 , 50×10^3 , 75×10^3 , and 100×10^3 cells at the end of ten days. The ten-day window was chosen considering the time required to form organoids from single cells for the slowest-growing PDO line, B188. At least 100×10^3 cells were required to achieve a 75% take rate for the PDO line B188. Hence, Matrigel-embedded organoids containing 100×10^3 cells were optimized as a seeding density for all the PDO lines.

Once the seeding density was determined, the PDO lines were seeded according to their growth curves to achieve organoids containing 100×10^3 cells ten days before transplantation. On EDD 9, the PDOs were transplanted on the CAM as Matrigel-embedded organoids. Successful tumor engraftment was determined five days after transplantation (EDD 14) by the macroscopic tumor growth on the CAM. On EDD14, primary tumors established on the CAM were harvested together with chick embryo organs, selectively the brain, heart, and liver (Figure 30).

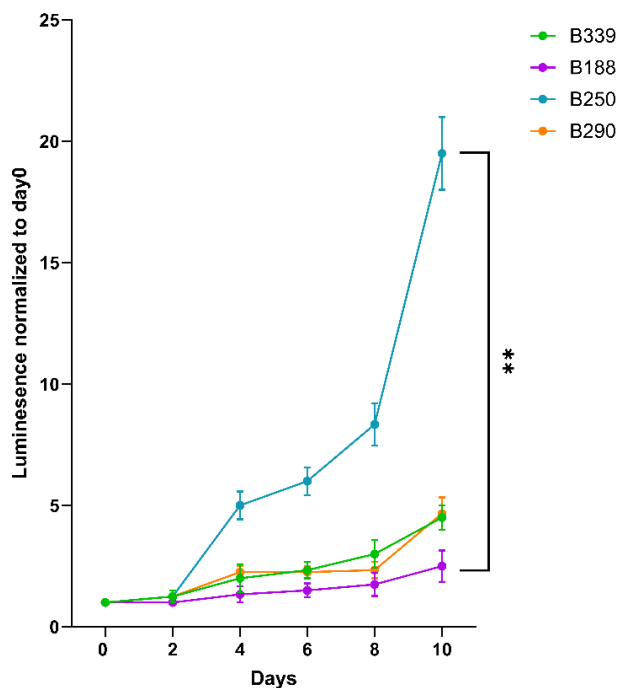


Figure 28: Growth rates of the PDO lines.

In vitro proliferation was measured every other day for ten days and calculated by normalizing the Day 2-Day 10 luminescence to the Day 0 luminescence. The data were collected from three independent experiments ($n = 3$, $N = 6$), and the Friedman test was performed to evaluate the statistical significance (** p -value = 0.0017). The mean and SEM are shown in the graph.

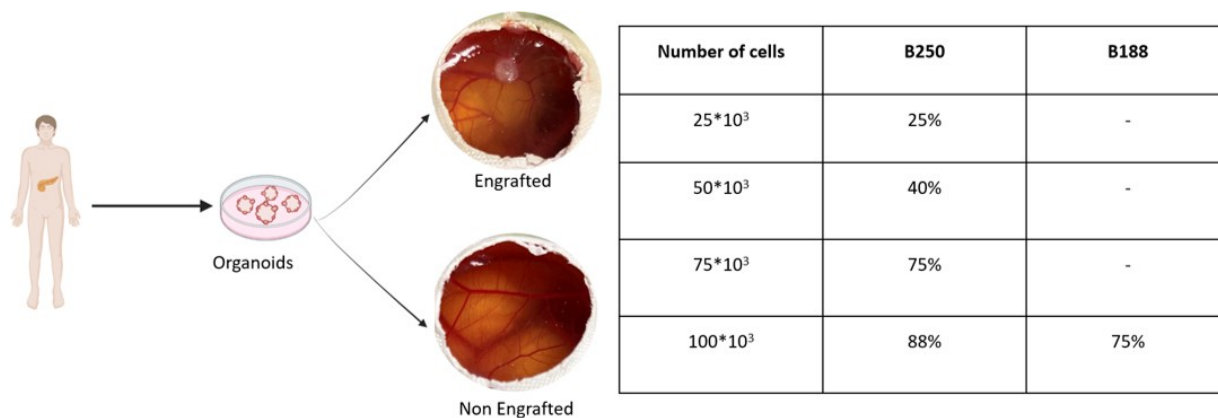


Figure 29: Optimization of PDO seeding density on CAM.

At least organoids containing $100 \cdot 10^3$ cells were required to achieve a 75% tumor take rate for the slowest growing PDO line, B188.

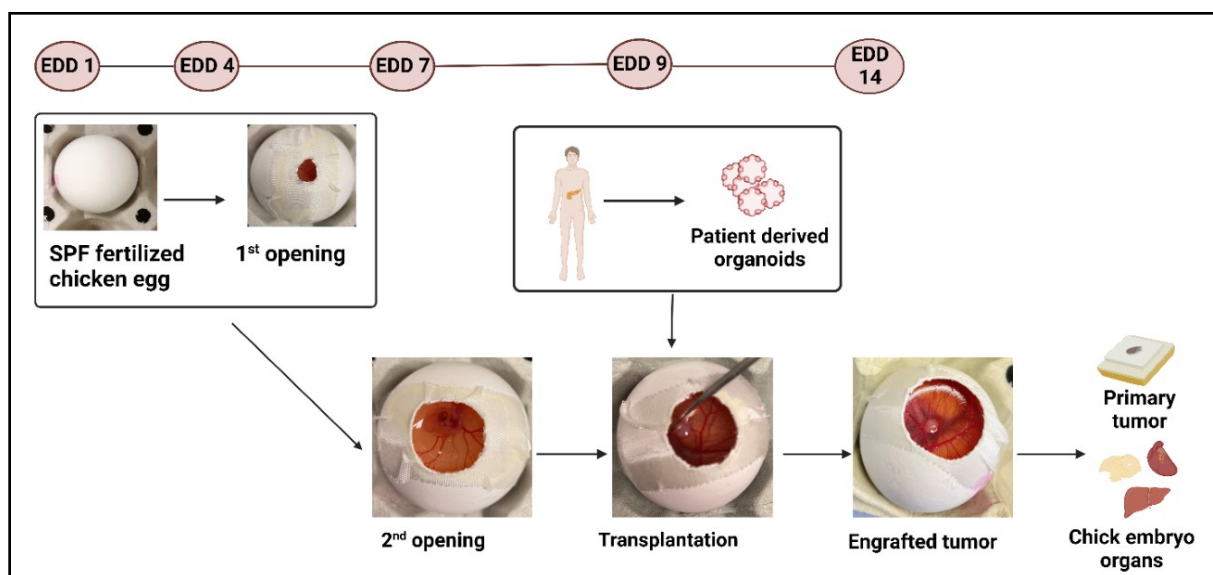


Figure 30: Establishment of the workflow using PDOs.

To achieve successful tumor engraftment, fertilized chicken eggs were prepared, facilitating the complete growth of CAM. For this purpose, as soon as the eggs were received, they were appropriately stored, and embryogenesis was initiated by providing 37 °C temperature and 70%-80% humidity. 1st and 2nd openings were made on EDD 4 and 7, respectively, allowing for the detachment of CAM from the eggshell membrane and growth. On EDD 9, PDOs embedded in Matrigel domes were transplanted on the CAM. Upon transplantation of organoids containing 100×10^3 cells, successful engraftment was achieved for the PDO lines B188, B250, B290, and B339 on EDD 14. Successfully engrafted primary tumors were harvested together with chick embryo organs, selectively the brain, heart, and liver.

5.3.5 Tumor take rates of PDO lines in the CAM model

To compare the tumor take rates, on EDD 9, the total number of transplanted eggs was noted for each cell line. On EDD 14, at the time of harvest, the number of eggs showed successful tumor engraftment, no tumor engraftment, and non-viable eggs were noted for each PDO line. Successful tumor engraftment was determined by observing macroscopic tumor growth on the CAM (Figure 31A).

Using the formula,

$$\frac{\text{Number of successfully engrafted eggs}}{\text{Number of transplanted Eggs} - \text{Number of non viable eggs}} \times 100\%$$

tumor take rates of PDO lines on CAM were determined. In contrast to the endogenous mouse-derived cell lines, there were no statistically significant differences observed in the tumor take rates between the PDO lines. All four PDO lines showed approximately 80% of the tumor take rate on CAM (Figure 31B).

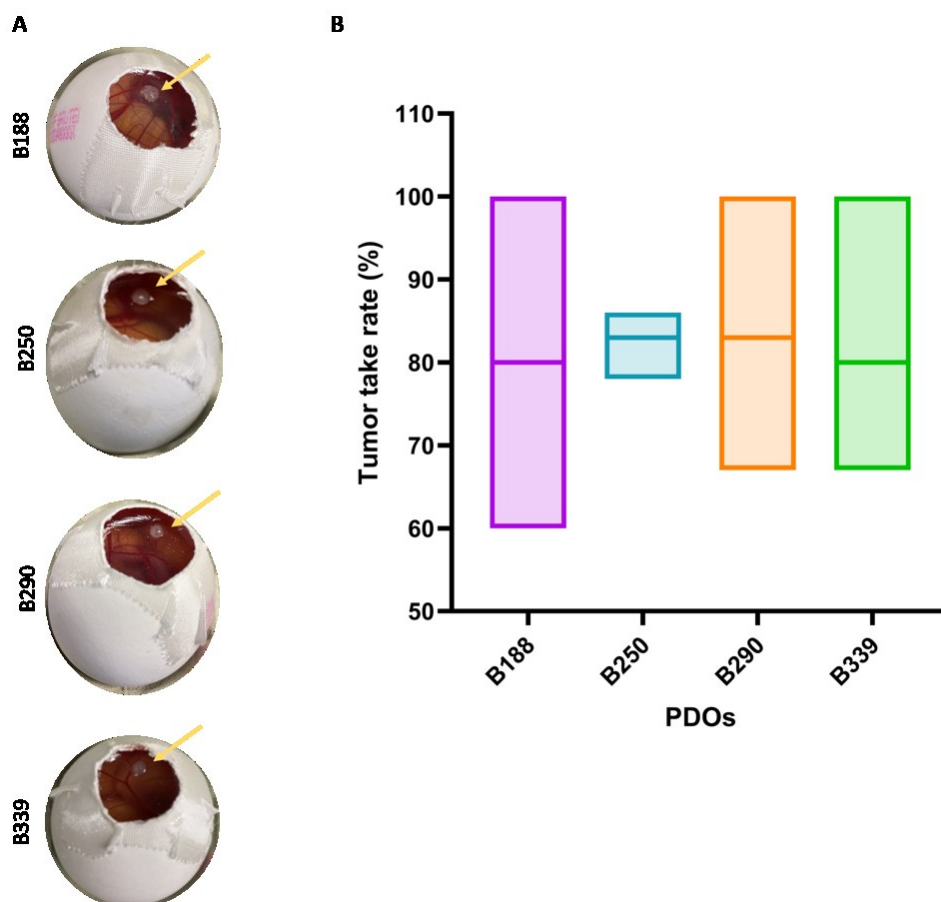


Figure 31: Tumor take rates of PDO lines on CAM.

A) Representative macroscopic tumors of the PDO lines B188, B250, B290, and B339 on CAM (indicated by yellow arrows), B) Tumor take rates of the PDO lines B188, B250, B290, and B339 on CAM. Tumor take rates were calculated by dividing the number of eggs that showed successful engraftment by the total number of viable eggs at the time of harvest. The total number of viable eggs at the time of harvest was calculated by subtracting the non-viable eggs at the time of harvest from the total number of transplanted eggs. The data were collected from three independent experiments ($n = 3$), and the Kruskal-Wallis test was performed to evaluate the statistical significance.

5.4 Characterization of selected cancer hallmarks in PDAC using the CAM PDX model

5.4.1 Characterization of primary tumor histology of PDOs-derived CAM xenografts

To investigate the histomorphological features of the CAM xenografts, tissue sections were obtained from paraffin-embedded blocks of CAM primary tumors, and H&E staining was performed according to a standard routine protocol. H&E-stained slides were then scanned using the Aperio Versa 8 digital scanner, and images were documented using Aperio Image Scope software (v.12.3.3.5048).

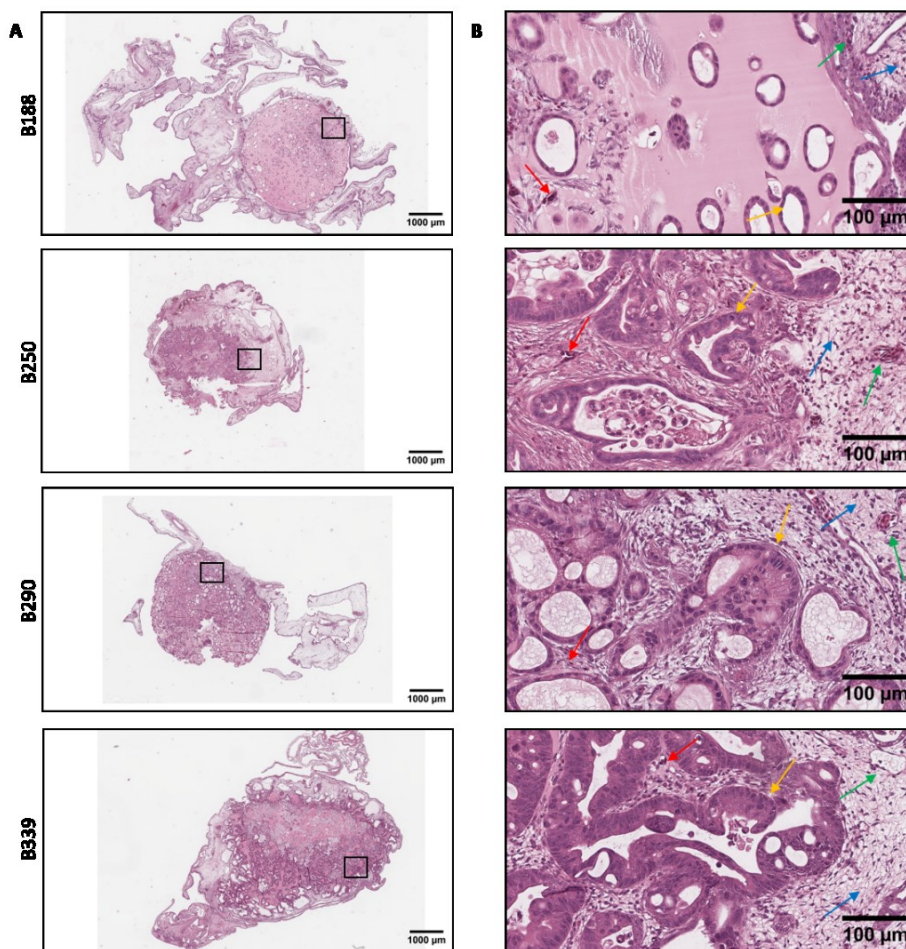


Figure 32: General histology of the CAM tumors, in which the tumor area, CAM, and blood vessels within the tumor area and CAM were easily distinguished.

A) Overview of representative H&E-stained B188, B250, B290, and B339 CAM tumor sections under 2X magnification, B) Representative H&E-stained B188, B250, B290, and B339 CAM tumor sections under 40X magnification. The tumor area (indicated in orange arrows), CAM (indicated in blue arrows), blood vessels within the tumor area (indicated in red arrows), and CAM (indicated in green arrows) were easily distinguished in the H&E-stained CAM xenografts.

In the H&E-stained sections of the CAM xenografts of the PDO lines B188, B250, B290, and B339, the tumor area and CAM were easily distinguished. The tumor area appeared as a solid mass of tumor cells (indicated by orange arrows in Figure 32) embedded in the Matrigel matrix, which was used to culture and prepare PDOs for transplantation. CAM appeared as a thin membrane surrounding the solid tumor (indicated by blue arrows in Figure 32). Blood vessels containing nucleated erythrocytes in light pink were seen both in the solid tumor area (indicated by red arrows in Figure 32) and CAM (indicated by green arrows in Figure 32).

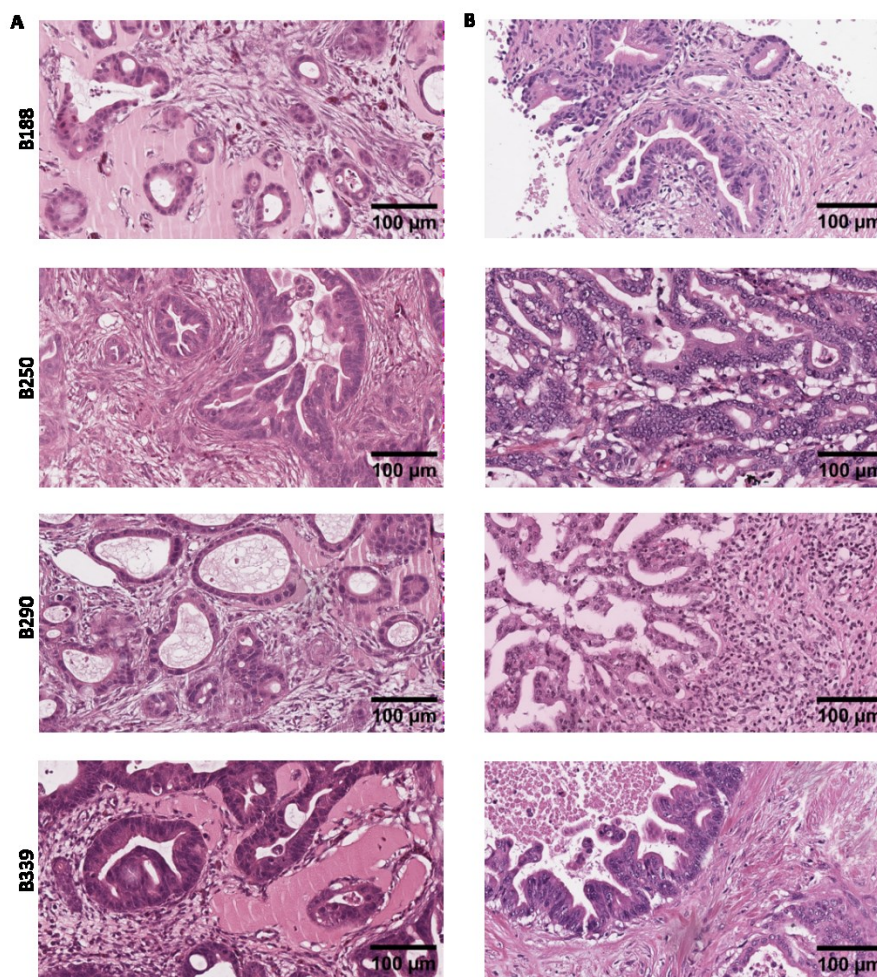


Figure 33: Comparison of the histomorphological features of CAM and patient tumors.

A) Representative H&E-stained B188, B250, B290, and B339 CAM tumor sections under 40X magnification, B) representative H&E-stained B188, B250, B290, and B339 patient tumor sections under 40X magnification.

The histomorphological features of the CAM tumors and the respective patient tumors were compared (Figure 33). For this purpose, similar to the CAM sections, patient tumor sections were obtained from paraffin-embedded blocks, and H&E staining was performed according to a standard routine protocol. H&E-stained slides were then scanned using the Aperio Versa 8 digital scanner, and images were documented using the Aperio Image Scope software (v.12.3.3.5048).

The PDO line B188 showed multifocal ductal neoplastic growth in the CAM xenografts. Tumor cells showed a growth pattern of flat to cuboidal morphology, and stromal infiltration was observed in around 10% of the tumor with a myxoid appearance. In the corresponding patient's primary tumor, mainly columnar growth patterns of tumor cells were seen. In addition, moderately differentiated ductal and cuboidal growth patterns of tumor cells were seen with moderate ECM deposition.

The PDO line B250 showed tumor cells with ductal to cribriform growth patterns in the CAM xenografts. The myxoid growth pattern was observed surrounding ductal-like tumor cells with a moderate amount of ECM components. In addition, columnar tumor cells with papillary to micropapillary growth patterns were also seen in the B250 CAM xenografts. Whereas the corresponding patient tumor was rich in tumor cells growing in ductal and tubular growth patterns in multilayer. In addition, scarce stromal reactions and extensive necrosis were observed in the corresponding patient tumor.

The PDO line B290 showed mainly a ductal pattern of tumor cells in the CAM xenografts. In addition, flat to cuboidal growth patterns of tumor cells were observed along with stromal infiltration. The corresponding patient tumor showed papillary, cuboidal, and columnar growth patterns of tumor cells along with high stromal infiltration and moderate amounts of ECM.

The PDO line B339 showed tumor cells with tubular to cribriform growth patterns in multilayers in the CAM xenografts. In addition, stromal infiltration was observed along with myxoid appearance. In the corresponding patient tumor, large ductal-like growth patterns with papillary projections into the ductal lumen were observed. Moderately differentiated tumor cells showing mainly columnar and partly cuboidal growth patterns were seen, along with moderate to high stromal infiltration. The comparison of CAM xenografts with the respective patient tumors revealed similarities in histomorphological features to a certain extent.

5.4.2 Characterization of tumor proliferation in PDOs-derived CAM xenografts

To characterize the *in ovo* tumor proliferation and growth, the CAM xenograft tissue sections were obtained from paraffin-embedded blocks of CAM primary tumors. Immunohistochemical staining was performed for Ki 67, a well-known marker for proliferation (Figure 34A). Ki 67 stained slides were scanned and analyzed using the Aperio Versa 8 digital scanner using the Aperio Image Scope software (v.12.3.3.5048).

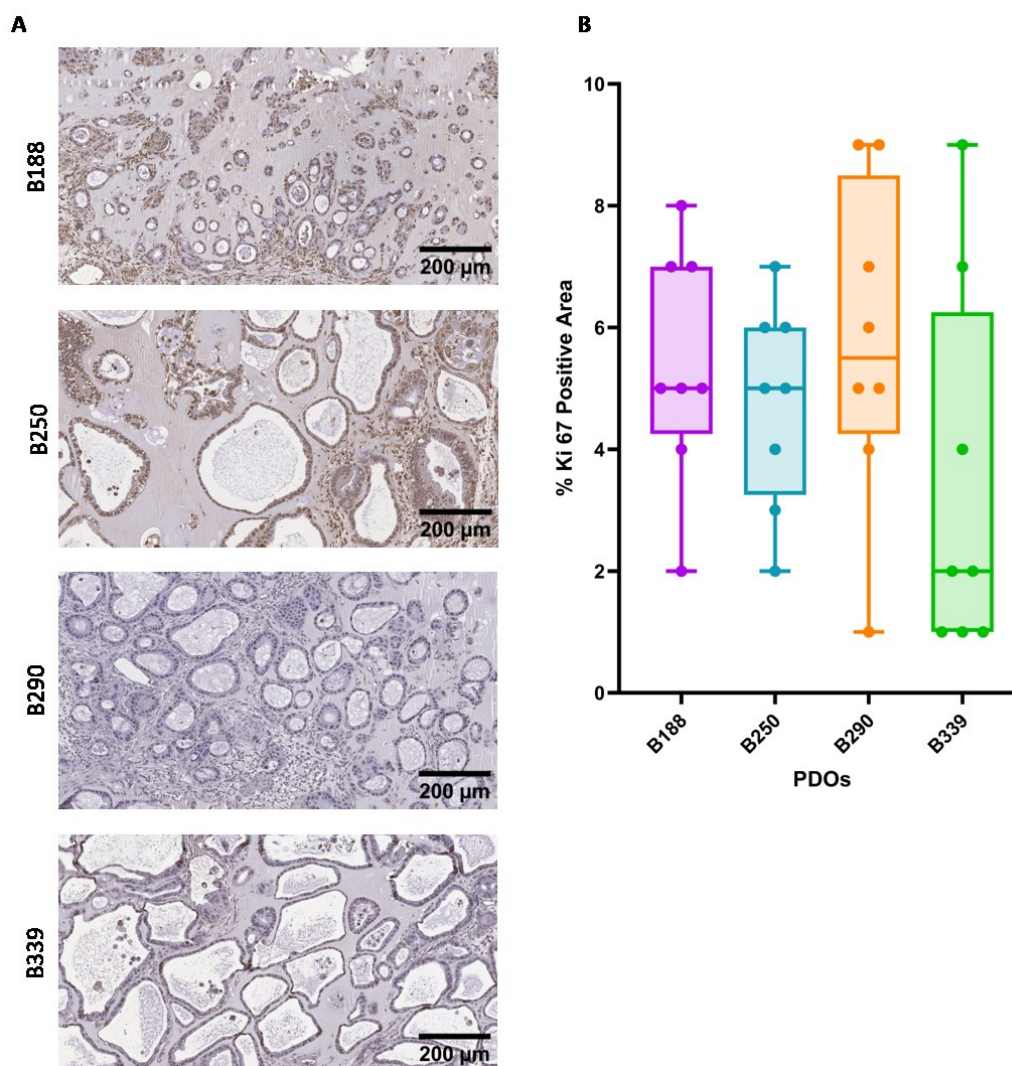


Figure 34: Characterization of tumor proliferation in CAM xenografts.

A) Representative Ki 67 stained B188, B250, B290, and B339 CAM xenograft sections under 20X magnification, B) Quantification of the percentage Ki 67 positive area of B188 (N = 8), B250 (N = 8), B290 (N = 8), and 339 (N = 8) CAM xenografts. The percentage Ki 67 positive area was calculated by dividing the Ki 67 positive pixels by the total number of pixels. The data were collected from three independent experiments (n = 3), and the Kruskal-Wallis test was performed to evaluate the statistical significance.

For the analysis, first, the tumor area was annotated on the digital scans of the CAM xenografts. Then, using the Positive Pixel Count v9 algorithm, Ki 67 staining was quantified. Using the formula,

$$\frac{\text{Ki 67 positive pixels}}{\text{Total pixels}} \times 100\%$$

percentage Ki 67 positive area was calculated. According to the percentage Ki 67 positive area, no statistically significant differences were observed in the proliferation of the PDOs *in ovo* (Figure 34B).

To check the *in vitro* proliferation of the PDOs, a CellTiter-Glo® 3D Cell Viability Assay was performed as mentioned in 5.3.4. The luminescence was measured every other day for ten days. Proliferation rates were calculated by normalizing the Day 2-Day 10 luminescence to the Day 0 luminescence. In contrast to *in ovo* proliferation, a statistically significant difference was observed between the PDOs B188 and B250 in *in vitro* proliferation (Figure 28).

5.4.3 Evaluation of metastatic dissemination of the PDOs using the CAM model

To determine the metastatic potential of the PDOs B188, B250, B290, and B339 by *Alu* qPCR, chick embryo organs, selectively the brain, heart, and liver, were collected on EDD 14. Genomic DNA isolation and *Alu* qPCR were performed to amplify the *Alu* sequences in the human DNA that could be found in the chick embryo organs due to metastatic dissemination. The expression of the *Alu* sequence was normalized to control chick embryo DNA, in which no transplantation was performed.

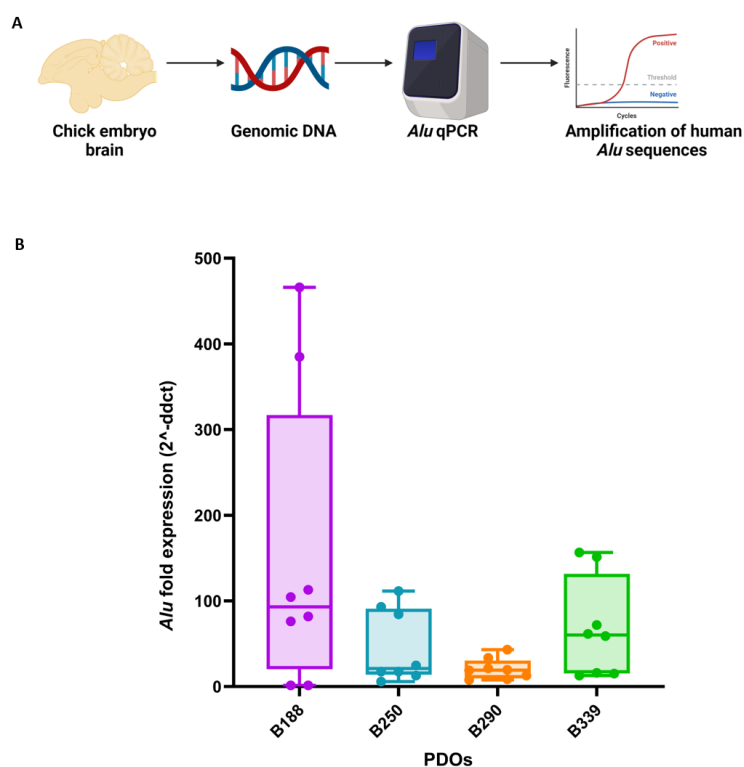


Figure 35: Metastatic dissemination in the chick embryo brain.

A) Schematic illustration of metastatic dissemination determination of the PDOs B188, B250, B290, and B339 in chick embryo brain using *Alu* qPCR, B) Quantification of metastatic dissemination of the PDOs B188 (N = 8), B250 (N = 8), B290 (N = 8), and 339 (N = 8) normalized to controls. The data were collected from three independent experiments (n = 3), and the Kruskal-Wallis test was performed to evaluate the statistical significance.

Based on the amplification of *Alu* sequences in chick embryo brain genomic DNA, the PDOs B188, B250, B290, and B339 showed metastatic dissemination. However, no statistically significant differences were observed in the metastatic dissemination of the PDOs to the chick embryo brain (Figure 35).

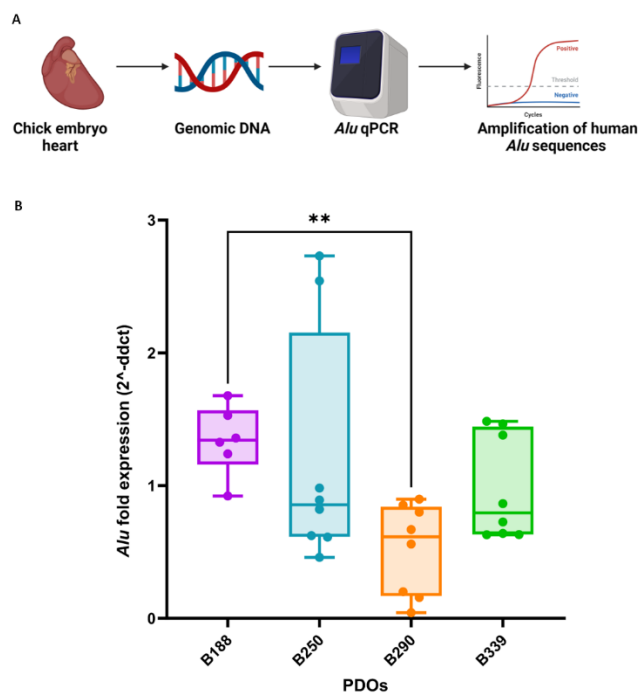


Figure 36: Metastatic dissemination in chick embryo heart.

A) Schematic illustration of metastatic dissemination determination of the PDOs B188, B250, B290, and B339 in chick embryo heart using *Alu* qPCR, B) Quantification of metastatic dissemination of the PDOs B188 (N = 8), B250 (N = 8), B290 (N = 8), and 339 (N = 8) normalized to controls. The data were collected from three independent experiments (n = 3), and the Kruskal-Wallis test was performed to evaluate the statistical significance (**p-value = 0.0018).

Based on the amplification of *Alu* sequences in chick embryo heart genomic DNA, the PDOs B188, B250, B290, and B339 showed metastatic dissemination. A statistically significant difference was observed between the PDOs B188 and B290 in the metastatic dissemination of the PDOs to the chick embryo heart (Figure 36).

Based on the amplification of *Alu* sequences in chick embryo liver genomic DNA, the PDOs B188, B250, B290, and B339 showed metastatic dissemination. A statistically significant difference was observed between the PDOs B250 and B290 in the metastatic dissemination of the PDOs to chick embryo liver (Figure 37).

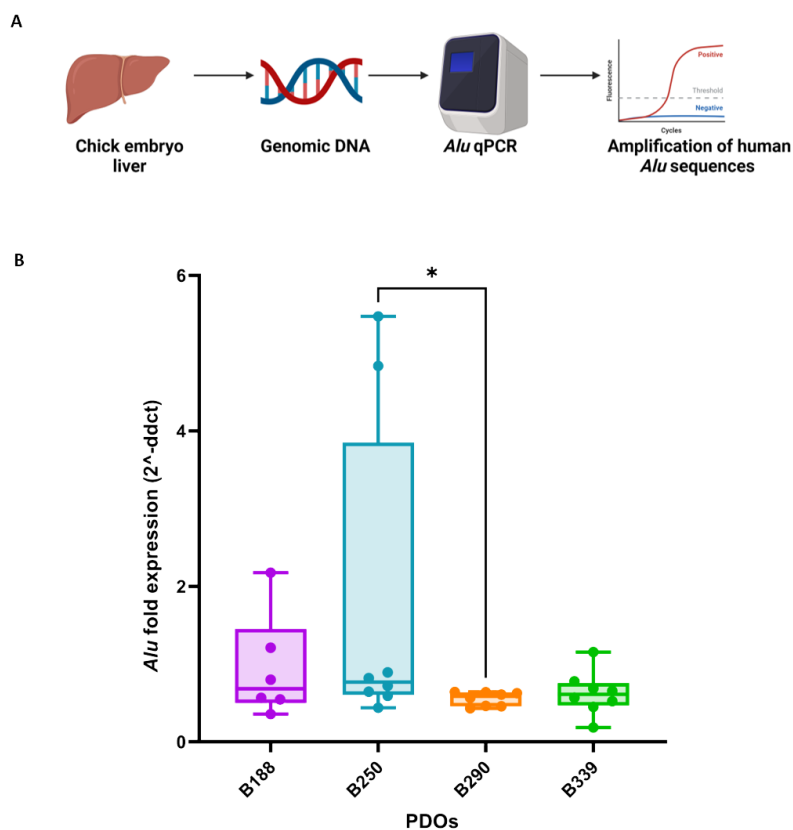


Figure 37: Metastatic dissemination in chick embryo liver.

A) Schematic illustration of metastatic dissemination determination of the PDOs B188, B250, B290, and B339 in chick embryo liver using *Alu* qPCR, B) Quantification of metastatic dissemination of the PDOs B188 (N = 8), B250 (N = 8), B290 (N = 8), and 339 (N = 8) normalized to controls. The data were collected from three independent experiments (n = 3), and the Kruskal-Wallis test was performed to evaluate the statistical significance (*p-value = 0.0332).

In vitro, the migration potential of the PDOs was determined by performing a scratch assay. For this purpose, the first 2D cell lines were generated and established from the PDOs B188, B250, B290, and B339. In a confluent monolayer of the cells, a scratch was made, and the closure of the scratch was documented at 0, 4, 8, and 24 hours by imaging (Figure 38A). B188 demonstrated a mesenchymal mode of migration during the early course of scratch closure, with single cells at the leading edge of the scratch. However, after the first 8 hours, small clusters of cells were observed at the leading edge of the scratch, showing a collective mode of migration as well. B250 and B290 showed a collective mode of migration, as a uniform sheet of epithelial cells maintaining the contact between the adjacent cells during the entire course of scratch closure. B339 demonstrated a mixed mode of migration where both mesenchymal and collective modes of migration were observed during scratch closure.

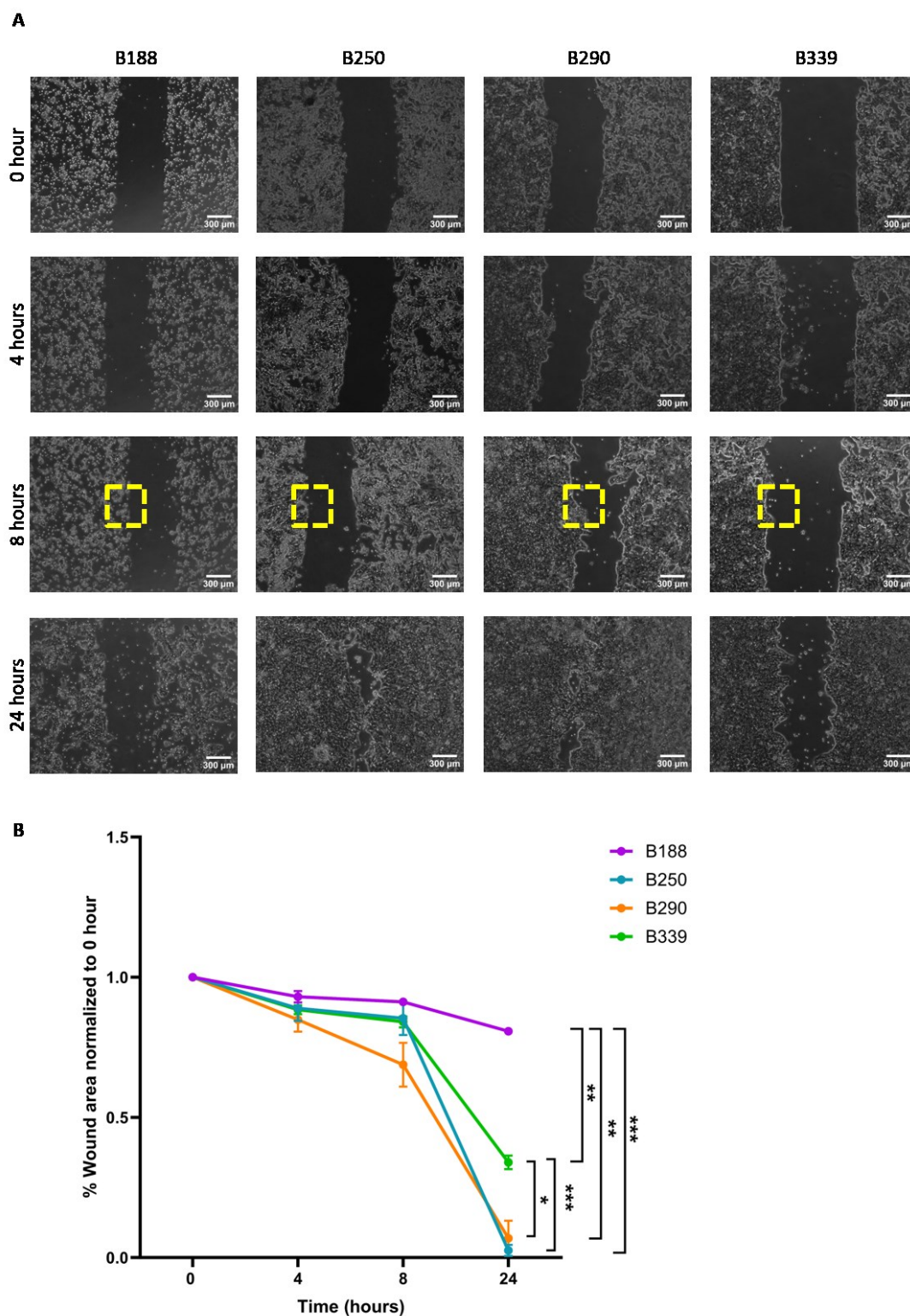


Figure 38: *In vitro* migration potential of the B188, B250, B290, and B339 2D cell lines.

A) Representative phase contrast images of the scratches in B188, B250, B290, and B339 monolayers at 0, 4, 8, and 24 hours, B) Quantification of the percentage wound area of B188, B250, B290, and B339 monolayers normalized to 0 hours. The data were collected from three independent experiments ($n = 3$, $N = 3$), and the Two-way ANOVA test was performed to evaluate the statistical significance (* p -value = 0.0362, ** p -value = 0.0012, 0.0065, *** p -value = 0.0001, 0.0007). The mean and SEM are shown in the graph.

Further, the *in vitro* migration potential was quantified as a percentage of wound area on the phase contrast images obtained using Image J wound healing size tool plugin software (Figure 38B). B250 and B290 showed the highest *in vitro* migratory potential, whereas B188 showed the lowest *in vitro* migratory potential in 24 hours. B339 showed intermediate *in vitro* migratory potential. However B250, B90, and B339 showed statistically significant differences in the *in vitro* migration potential compared to B188. In addition, statistically significant differences were observed in the *in vitro* migration potential of B339 compared to B250 and B290. B250 and B290 with the highest *in vitro* migration potential, did not show any statistically significant difference between them.

5.4.4 Characterization of the stroma in CAM xenografts

The histological analysis of B188, B250, B290, and B339 CAM xenografts using H&E-stained sections showed different degrees of stromal infiltration (Figure 39). Minimal stromal infiltration was observed in the B188 CAM xenografts, surrounding a few tumor cells growing in a ductal pattern. B250, B290, and B339 CAM xenografts showed moderate to high stromal infiltration in the H&E-stained sections. To confirm the stromal infiltration from the host, immunohistochemical staining for human-specific CK 19, a PDAC marker, was performed on the CAM xenografts (Figure 39). Tumor cells in the CAM xenografts showed positive CK 19 staining. In contrast, the stroma showed negative CK 19 staining, confirming the stromal infiltration from the host. Similar to the CAM xenografts derived from murine cells, the characterization of the pan-CAF population in PDOs-derived CAM xenografts was done by staining for a pan-CAF marker, Vimentin (Elyada et al., 2019).

Hence, the CAM xenografts from the PDO lines B188, B250, B290, and B339 have been stained for chicken-specific Vimentin. For this purpose, CAM xenograft tissue sections were obtained from paraffin-embedded blocks of CAM primary tumors, and immunohistochemical staining for chicken-specific Vimentin was performed on the CAM xenografts derived from the PDO lines B188, B250, B290, and B339. Vimentin-stained CAM xenografts confirmed the presence of CAFs in the CAM xenografts derived from the PDO lines B188, B250, B290, and B339 (Figure 40A).

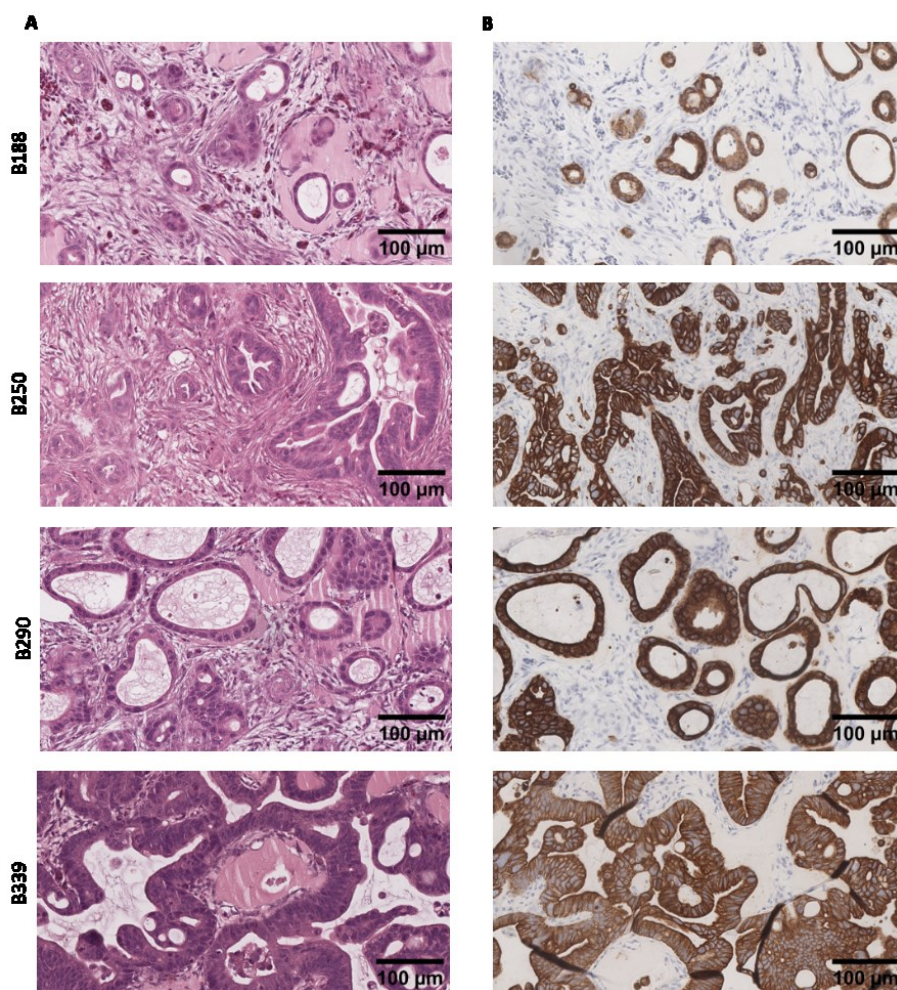


Figure 39: Stromal infiltration in CAM xenografts

A) Representative H&E-stained B188, B250, B290, and B339 CAM xenograft sections showing stromal infiltration under 40X magnification, B) Representative CK19-stained B188, B250, B290, and B339 CAM xenograft sections showing CK19 negative stromal cells under 40X magnification.

Immunohistochemical quantification of Vimentin was performed to determine the differences in CAF infiltration in the CAM xenografts derived from the PDO lines B188, B250, B290, and B339. For this purpose, Vimentin-stained CAM xenograft sections were scanned using the Aperio Versa 8 digital scanner and analyzed using the Aperio Image Scope software (v.12.3.3.5048). For the analysis, the tumor area was first annotated on the digital scans of the CAM xenografts. Then, using the Positive Pixel Count v9 algorithm, Vimentin staining was quantified. Using the formula,

$$\frac{\text{Vimentin positive pixels}}{\text{Total pixels}} \times 100\%$$

percentage Vimentin positive area was calculated. According to the percentage Vimentin positive area, no statistically significant differences were observed in the pan-CAF population between the PDO lines (Figure 40B).

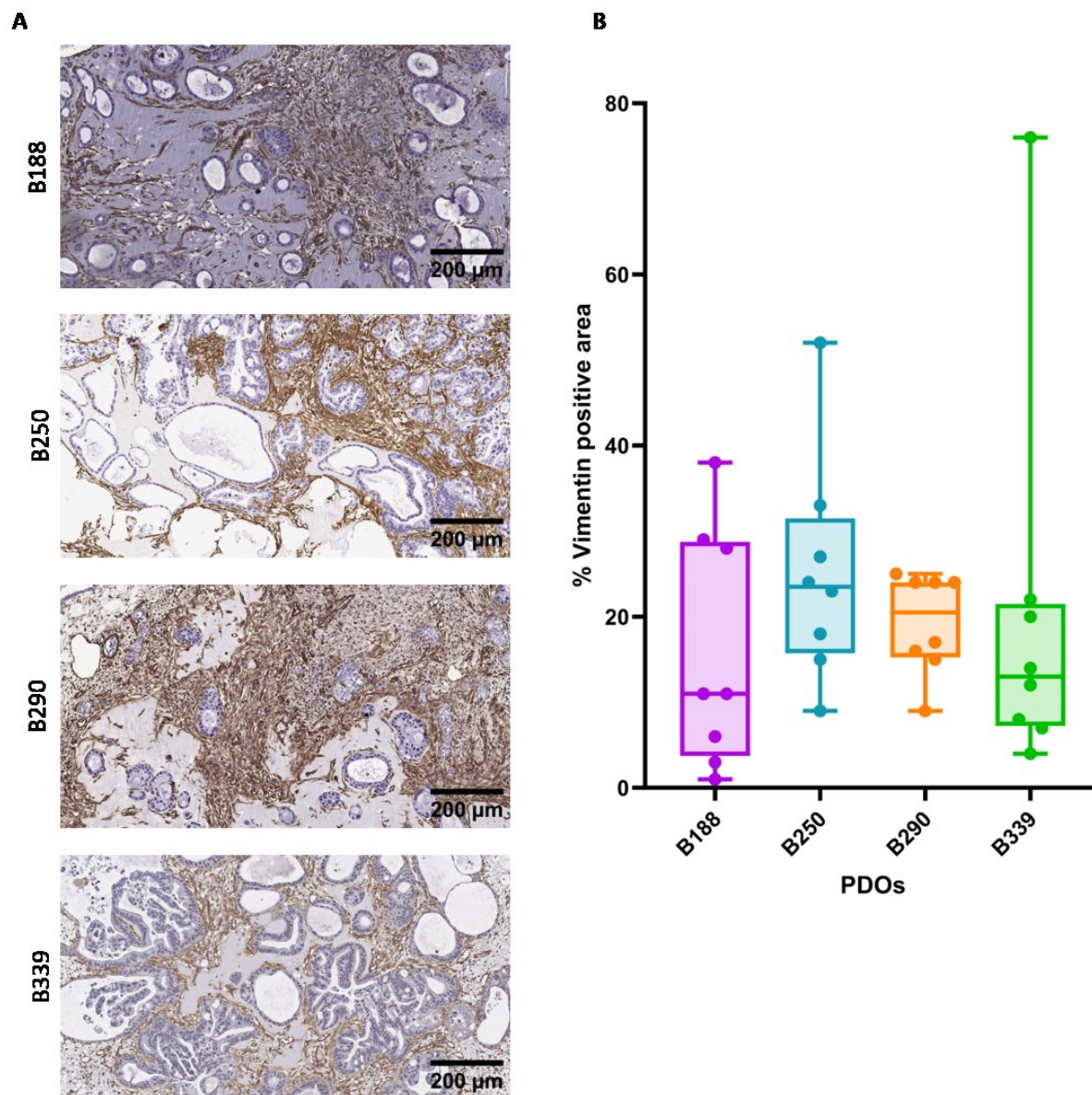


Figure 40: Vimentin staining showing the pan-CAF population in CAM xenografts

A) Representative Vimentin-stained B188, B250, B290, and B339 CAM xenograft sections under 20X magnification, B) Quantification of the percentage Vimentin positive area of B188 (N = 8), B250 (N = 8), B290 (N = 8), and 339 (N = 8) CAM xenografts. The percentage of Vimentin positive area was calculated by dividing the Vimentin positive pixels by the total number of pixels. The data were collected from three independent experiments (n = 3), and the Kruskal-Wallis test was performed to evaluate the statistical significance.

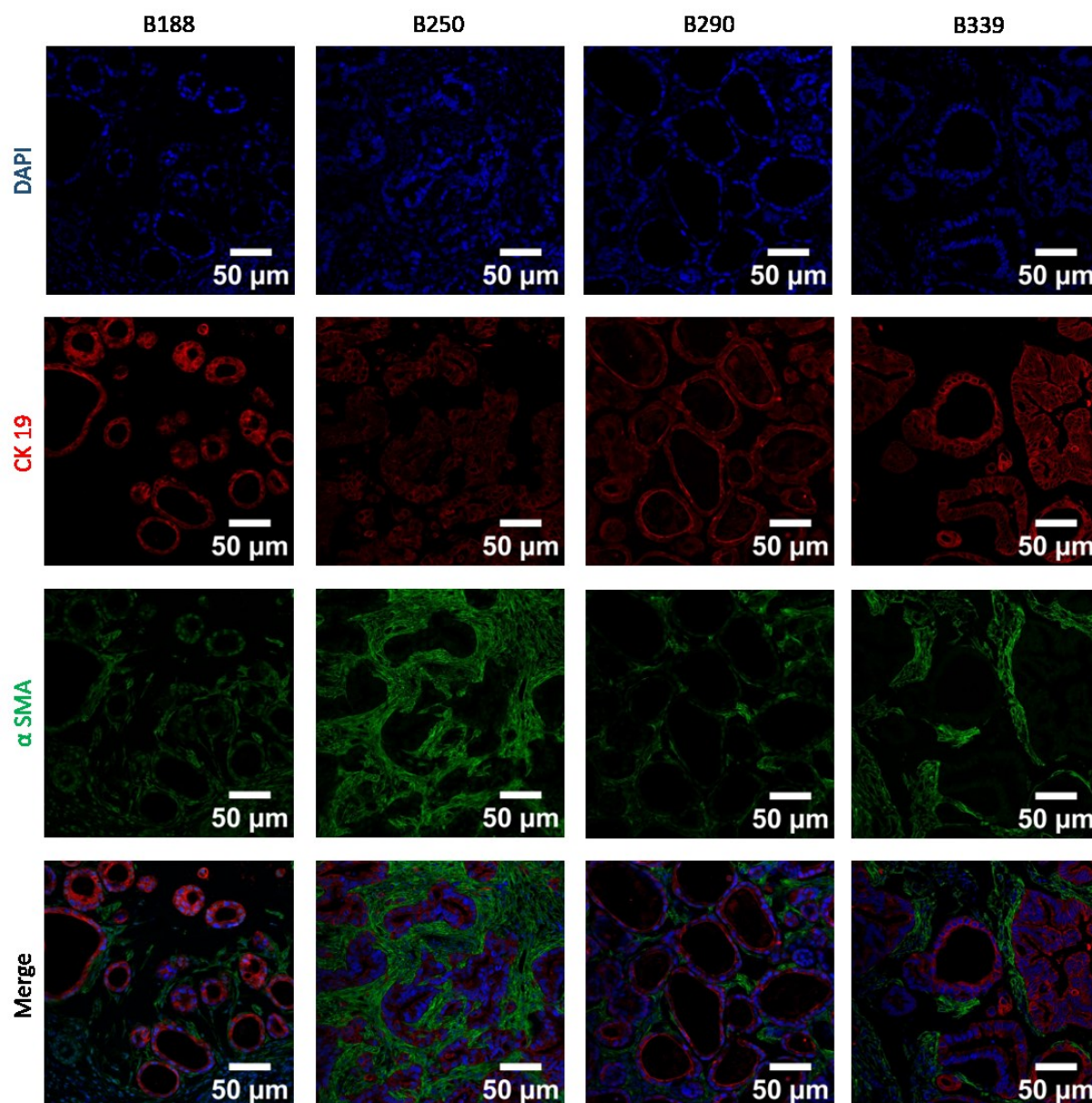


Figure 41: α -SMA and CK 19 co-staining shows the presence of α -SMA positive fibroblast infiltration in CAM xenografts

Immunofluorescence microscopic analysis of representative α -SMA and CK 19 co-stained B188, B250, B290, and B339 CAM xenograft sections shows the infiltration of α -SMA positive CAFs under 40X magnification.

Like murine cells-derived CAM xenografts, to characterize activated CAFs that express α -SMA involved in ECM remodeling of PDAC, PDOs-derived CAM xenografts were co-stained for CK 19 and α -SMA. (Han et al., 2020). Immunofluorescence imaging of the co-stained CAM xenografts showed CK 19 positive, α -SMA negative tumor cells and infiltrating α -SMA positive, CK 19 negative CAFs (Figure 41). Immunofluorescence microscopic analysis of CK 19 and α -SMA co-stained B188, B250,

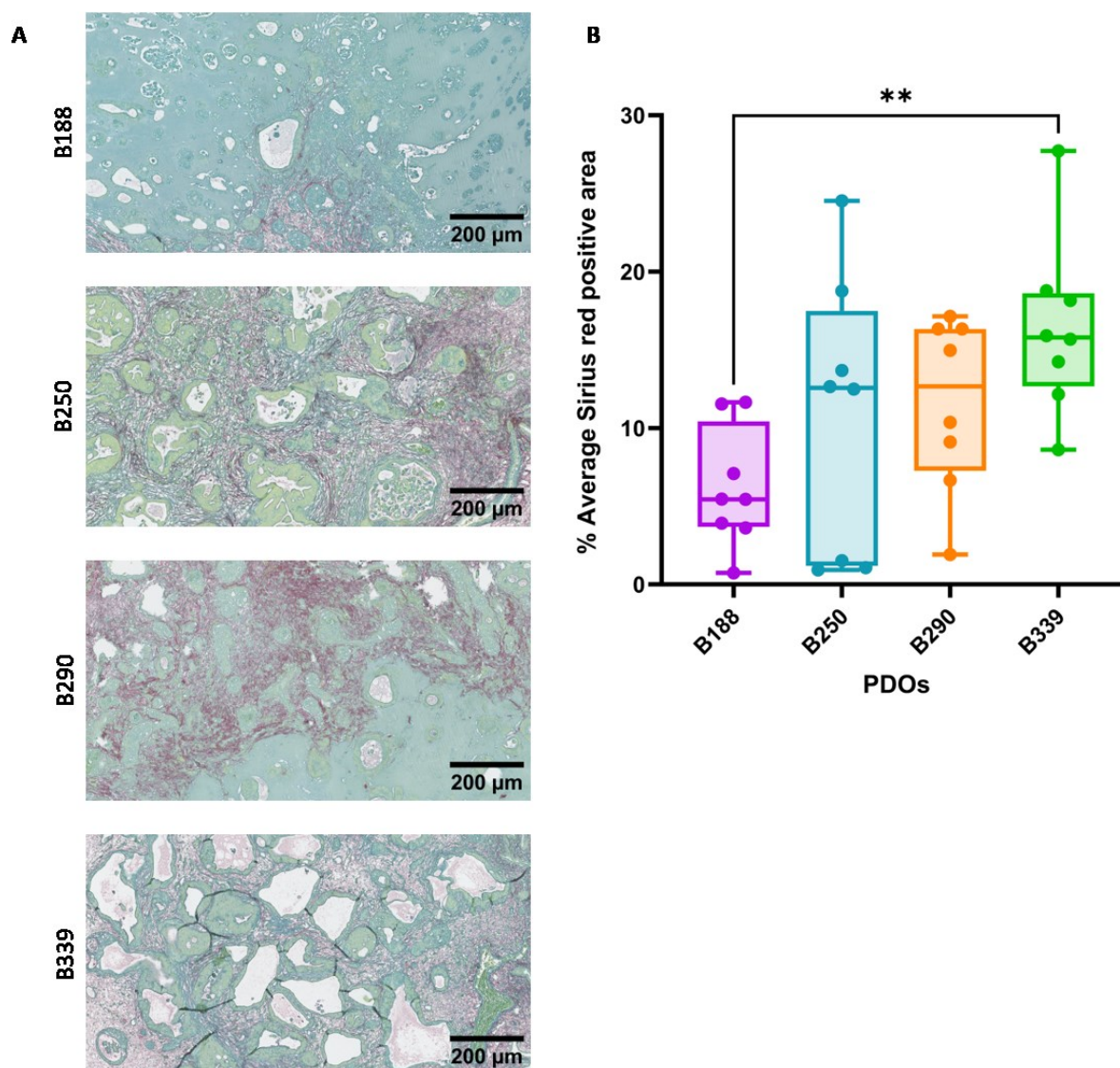


Figure 42: Sirius red staining showing fibrillar collagen deposition in CAM xenografts

A) Representative B188, B250, B290, and B339 CAM xenograft sections under 20X magnification, B) Quantification of the percentage Sirius red positive area of B188 (N = 8), B250 (N = 8), B290 (N = 8), and 339 (N = 8). The percentage of the Sirius red positive area was calculated by dividing the Sirius red positive pixels by the total number of pixels. The data were collected from three independent experiments (n = 3), and the Kruskal-Wallis test was performed to evaluate the statistical significance (*p-value = 0.0210, **p-value = 0.0024).

B290, and B339 CAM xenografts revealed differences in the infiltration of α -SMA positive CAFs. B188 CAM xenografts showed a CK-19 positive tumor cell population growing in a ductal pattern surrounded by α -SMA positive CAFs. B250, B290, and B339 CAM xenografts showed a CK 19 positive tumor cell population with moderate to high infiltration of α -SMA positive CAFs (Figure 41).

Like murine cells-derived CAM xenografts, to characterize fibrillar collagens in the stroma, Sirius red staining was performed on PDOs-derived CAM xenografts. Collagen types I and III constitute fibrillar collagens, the abundant acellular component of the ECM that makes the desmoplastic PDAC stroma, thereby being involved in PDAC progression (Maneshi et al., 2021). To determine the fibrillar collagen deposition, Sirius red staining was performed on the CAM xenografts. For this purpose, CAM xenograft tissue sections were obtained from paraffin-embedded blocks of CAM primary tumors, and Sirius red staining was performed (Figure 42A). Sirius red-stained slides were then scanned using the Aperio Versa 8 digital scanner, and the images were documented.

Using a DMI8 Leica Thunder microscope, polarized imaging of Sirius red-stained slides was performed, and the birefringence was measured. Using Image J software, positive pixels in each tissue section were quantified, and the percentage of Sirius red positive area was calculated. Using the formula,

$$\frac{\text{Sirius red positive pixels}}{\text{Total pixels}} \times 100\%$$

percentage Sirius red positive area was calculated (Figure 42B). According to the percentage of Sirius red positive area, high fibrillar collagen deposition was observed in the CAM xenografts derived from the PDO line B339. The lowest fibrillar collagen deposition was observed in the CAM xenografts derived from the PDO line B188. In addition, fibrillar collagen deposition between the PDO lines B188 and B339 showed a statistically significant difference.

Similar to fibrillar collagens, hyaluronan is another major component of the desmoplastic stroma of PDAC, which is involved in PDAC progression. Hence, to determine the hyaluronan deposition, immunohistochemical staining of hyaluronan binding peptide (HABP) was performed (Figure 43A) on the CAM xenografts. For this purpose, CAM xenograft tissue sections were obtained from paraffin-embedded blocks of CAM primary tumors, and HABP staining was performed. HABP-stained slides were then scanned using the Aperio Versa 8 digital scanner and analyzed using the Aperio Image Scope software (v.12.3.3.5048). For the analysis, first, the tumor area was annotated on the digital scans of the CAM xenografts. Then, using the Positive Pixel Count v9 algorithm, HABP staining was quantified.

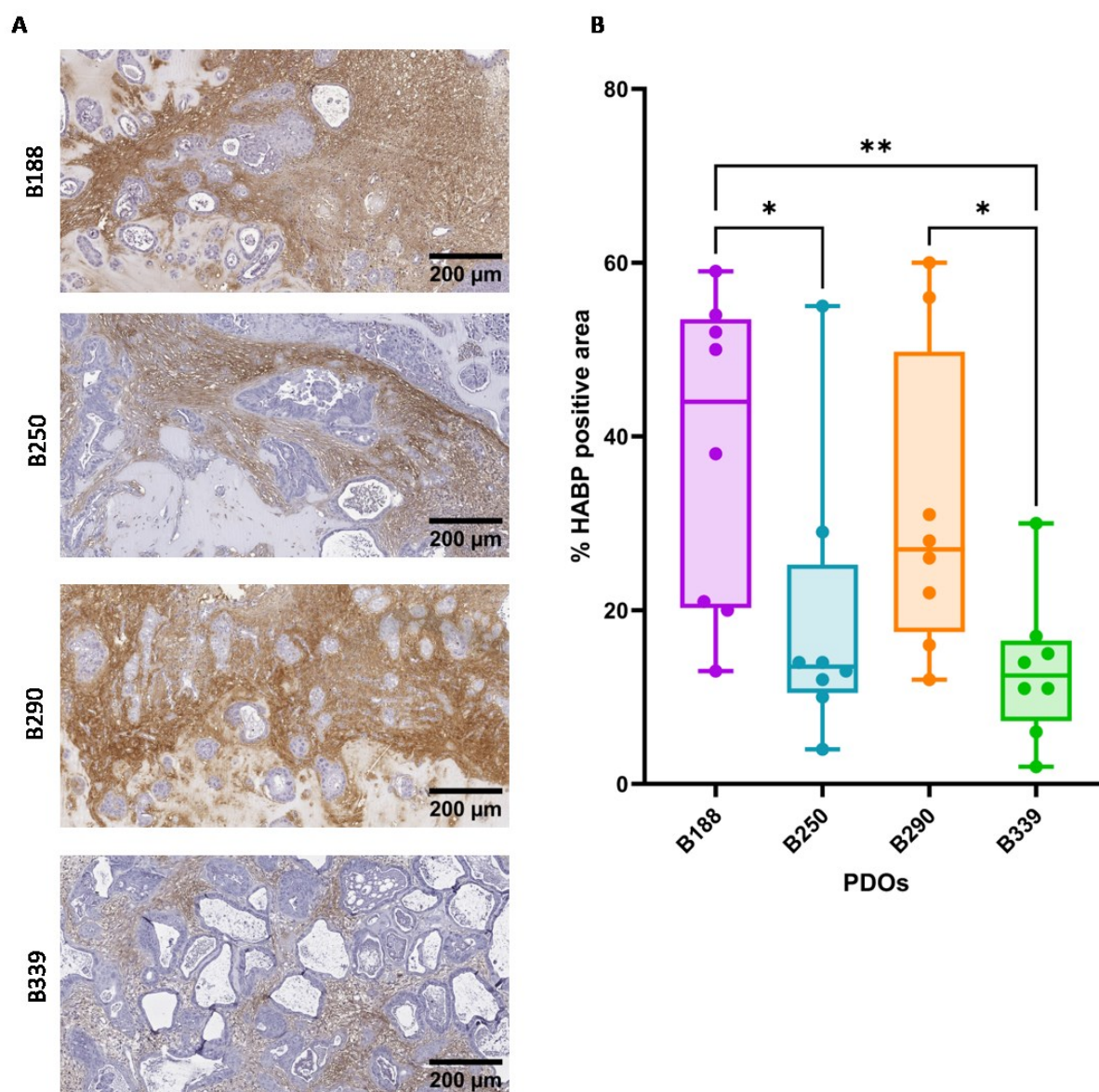


Figure 43: HABP staining showing the hyaluronan deposition in CAM xenografts

A) Representative HABP-stained B188, B250, B290, and B339 CAM xenograft sections under 20X magnification, B) Quantification of the percentage HABP positive area of B188 (N = 8), B250 (N = 8), B290 (N = 8), and B339 (N = 8) CAM xenografts. The percentage of HABP positive area was calculated by dividing the HABP positive pixels by the total number of pixels. The data were collected from three independent experiments (n = 3), and the Kruskal-Wallis test was performed to evaluate the statistical significance (*p-value = 0.0183, 0.0260, **p-value = 0.0068).

Using the formula,

$$\frac{\text{HABP positive pixels}}{\text{Total pixels}} \times 100\%$$

percentage HABP positive area was calculated (Figure 43B). According to the percentage HABP positive area, different degrees of hyaluronan deposition were observed in the CAM xenografts derived from the PDO lines B188, B250, B290, and B339. Similar to fibrillar collagen deposition, a significant difference in hyaluronan deposition was observed between the PDO lines B188 and B339. In addition, hyaluronan deposition observed in B188 CAM xenografts also significantly differed from that observed in B250 CAM xenografts. On the other hand, a significant difference in hyaluronan deposition was observed between the PDO lines B339 and B290 CAM xenografts.

6. Discussion

The complex and huge heterogeneity of PDAC challenges efforts to understand the disease and develop novel therapeutic approaches. To better understand the complex disease mechanism and to develop optimal therapeutic options, establishing suitable *in vivo* models is an essential step. Murine models are the most popular *in vivo* models used in PDAC research. However, murine models have raised ethical concerns and are expensive and time-consuming (Chu et al., 2022). According to Directive 2010/63, at the European level, animals should be used for scientific purposes only when there is no alternative. In addition, according to the 3R principle of replacement, reduction, and refinement, animals should be replaced by fewer sentient beings. Considering the ethical issues, cost, and large time frame associated with the rodent models, the CAM may be an alternative *in vivo* model for cancer studies. So far, CAM has been used to study several cancers, including gastrointestinal cancers such as colon cancer, hepatocellular carcinoma, and pancreatic cancer. Rovithi et al. successfully developed a bioluminescent CAM model for PDAC by engrafting luciferase-transduced primary human PDAC cells onto the CAM to evaluate tumor growth (Rovithi et al., 2017). In addition, this study showed that the histomorphological and genetic characterization of original tumors and CAM xenografts were comparable (Rovithi et al., 2017).

Emerging PDAC molecular subtyping studies have shown the complex and vast heterogeneity of PDAC and associated clinical outcomes (Bailey et al., 2016; Chan-Seng-Yue et al., 2020; Collisson et al., 2011; Moffitt et al., 2015). So far, the applicability of the CAM model to functionally study the PDAC subtypes has not been explored. Therefore, the present study aimed to establish CAM as an alternative model to functionally study PDAC subtypes, focusing on tumor growth, metastatic dissemination, and the tumor microenvironment.

Further, this study aimed to establish CAM as an alternative PDX model to study PDAC by successfully engrafting PDOs onto the CAM. PDOs retain the molecular and functional architecture of the original patient tumors more efficiently when compared to 2D cells, even after several passages (Miebach et al., 2022). However, to explore complex cancer hallmarks such as invasiveness, metastatic dissemination, and interaction with the tumor microenvironment, *in vivo* models are required (Jian et al., 2020). Hence,

PDX models have been developed by orthotopically transplanting PDOs into immunocompromised mice. Considering the advantages that the CAM model offers in regards to ethical concerns, cost, and experimental time frame, the CAM model could be a useful alternative. Considering the clinical predictive value of PDOs and their ability to recapitulate the molecular profiles of patient tumors, in this study, CAM has been employed as an alternative PDX model by engrafting PDOs. Furthermore, complex cancer hallmarks such as metastatic dissemination and cross-talk with the tumor microenvironment have been explored using the CAM model.

6.1 Establishment of the CAM model and the workflow

The workflow of the CAM assay was established based on previous literature with few adaptations. Due to the high survival rate associated with *in ovo* CAM assays compared to *ex ovo* assays, in this study we used the *in ovo* approach (Meijlink et al., 2021; Naik et al., 2018). As previously described, the first and second openings of the SPF eggs were made on EDD4 and EDD7, respectively (Hu et al., 2019; Kunz et al., 2019; Pawlikowska et al., 2020). Similar to previous studies, transplantation of both murine cells and PDOs was performed on EDD 9 on the CAM. CAM model for various human cancer entities has been successfully developed by transplanting 1×10^6 cells resuspended in Matrigel on EDD 9 (Kunz et al., 2019; Power et al., 2022; Ranjan et al., 2023). In this study, the same approach was employed for the transplantation of murine cells on the CAM, which resulted in successful tumor engraftment on EDD 14.

In order to achieve successful tumor engraftment upon transplantation of the PDOs, the seeding density and method were modified. Once trypsinized, it takes 10 days for single cells to again form PDOs. Hence, 10 days prior to transplantation, on CAM PDOs were cultured *in vitro*. In contrast to murine cells, PDOs with a high *in vitro* proliferation rate, such as B250, demonstrated successful tumor engraftment on EDD 14, even when 25×10^3 cells were transplanted. PDOs with a low *in vitro* proliferation rate, such as B188, required at least 1×10^5 cells to be transplanted in order to develop tumors on the CAM at the end of EDD 14. Hence, for the transplantation of PDOs, 1×10^5 cells/ egg was optimized as seeding density. This optimized transplantation protocol resulted in successful tumor engraftment on EDD 14. Since chick embryos are unable to experience pain until EDD 14, many

countries do not require ethical approval until EDD 14 (Augustine et al., 2020). Besides, some of the studies have reported the occurrence of a non-specific inflammatory reaction when the CAM assay extends after EDD 14 (Mangir et al., 2018). In addition, cell-mediated immunity is not completely developed until EDD 14. (Kunz et al., 2019). Considering these issues, EDD 14 was chosen as the end point for the CAM assay in this study.

6.2 Characterization of selected cancer hallmarks in PDAC using the endogenous mouse cells-derived CAM model

Endogenous KPC mouse-derived PDAC cells characterized transcriptomically and morphologically were used to establish CAM as an alternative model to study PDAC subtypes. So far, several schemes of PDAC subtype classification have been proposed. Based on the subtyping schemes proposed, PDAC is transcriptomically stratified into classical, quasi-mesenchymal, and basal subtypes (Bailey et al., 2016; Chan-Seng-Yue et al., 2020; Collisson et al., 2011; Moffitt et al., 2015; Puleo et al., 2018). Using PurIST, a single sample classifier based on a meta-analysis of the clinical utility of existing PDAC subtypes (Rashid et al., 2020), the KPC murine cell lines were transcriptomically subtyped. Morphological characterization of the KPC murine cells by phase contrast microscopy also supported the transcriptomic subtyping of the murine PDAC cell lines 9366, 12548, and R405. The cytoskeleton architecture of the murine PDAC cells by Phalloidin staining clearly showed the epithelial morphology of the cell line 9366, which was transcriptomically characterized as a classical PDAC subtype. Similarly, the cell line R405 transcriptomically subtyped as basal PDAC subtype, showed mesenchymal morphology. The cell line 12548, transcriptomically characterized as a quasi-mesenchymal PDAC subtype, showed clusters of cells with mixed phenotypes of both epithelial and mesenchymal morphology. Using the morphologically and transcriptomically characterized murine PDAC cell lines 9366, 12548, and R405, the CAM model was optimized to study the PDAC subtypes.

Even though the cell lines 9366, 12548, and R405 developed tumors on the CAM, differences in the take rates were observed. The highest and lowest tumor take rates were achieved by 9366 and R405 cell lines, respectively. Even though the basal PDAC subtype is more aggressive than the classical PDAC subtype, it was not reflected by the tumor take rates (Lomberk et al., 2018). The possible explanation

for this could be the matrix used for transplantation. Several studies have shown that different matrices favor different morphological phenotypes (Franchi et al., 2023; Ruud et al., 2020; Wahbi et al., 2020). Matrigel supports polarization of the cells, thereby favoring epithelial growth of the cells (Kakni et al., 2022). Since the tumor cells are transplanted as Matrigel droplets on the CAM, the cell line 9366 showing epithelial morphology has a growth advantage in Matrigel compared to the cell lines 12548 and R405 representing the quasi-mesenchymal and basal PDAC subtypes, respectively.

Only a few studies have shown the histomorphological comparison of CAM xenografts with murine xenografts. Hu et al. showed that CAM xenografts recapitulated the same growth pattern and histomorphological features as the clear cell subtype of the renal carcinoma mouse model (Hu et al., 2019). Another study compared the histomorphological features of the breast cancer cell lines MCF-7 and MDA-MB-231, representing the HR+ (luminal) and triple negative breast cancer (TNBC) subtypes in the CAM and murine xenografts (Ranjan et al., 2023). This study showed that MCF-7 and MDA-MB-231 cell lines were presented as invasive breast cancers of no special subtype in both CAM and murine xenografts (Ranjan et al., 2023). This study also showed that the tumor grades were comparable in CAM and murine xenografts for both the cell lines MCF-7 and MDA-MB-231. In addition, the triple negative status of MDA-MB-231 was confirmed in both CAM and murine xenografts by immunohistochemical analyses (Ranjan et al., 2023). Similarly, a luminal B-like phenotype with ER/PR positive and HER2 negative status was predominantly observed for the MCF-7 cell line in both CAM and murine xenografts (Ranjan et al., 2023). Similarly, the current study showed that CAM xenografts from the cell lines 9266, 12548, and R405 showed distinct histomorphological features associated with the PDAC subtypes represented by each cell line. In addition, CAM xenografts recapitulated the histomorphological features of the primary tumors derived from endogenous mouse models. However, these comparisons were made based on the H&E-stained primary tumor sections. Further validation by immunohistochemical subtyping using KRT81, HNF1A, and GATA6 expression is required to compare the subtypes represented in the CAM and murine xenografts (Muckenhuber et al., 2018; O'Kane et al., 2020). In addition, grading the murine and CAM xenografts also allows us to check if the murine tumors are recapitulated by CAM tumors.

Even though the cell lines 9366, 12548, and R405 represent classical, quasi-mesenchymal, and basal PDAC subtypes, they were associated with different pathological features and clinical outcomes; no differences were observed in the *in vitro* proliferation of the cell lines. However, *in ovo* proliferation of the cell line 9366, characterized by Ki 67 staining showed significantly higher *in ovo* proliferation when compared to the cell lines 12548 and R405. Several studies showed that Ki 67 is an independent prognostic factor in PDAC and is used to evaluate the proliferation index by immunohistochemical staining (Andriesi-Rusu et al., 2019; Pergolini et al., 2019). However, the role of Ki 67 as an independent prognostic factor remains unclear. Some studies showed that a high proliferation index correlates to poor survival and adverse clinical features, whereas other studies could not confirm this correlation (Andriesi-Rusu et al., 2019). In addition, some studies suggest that a high proliferation index detected by Ki 67 staining is associated with successful tumor engraftment in the PDX models (Tanaka et al., 2020). Since the CAM model favors the engraftment of epithelial cells more, a higher *in ovo* proliferation index for the cell line 9366 was expected.

CAM has been used as a model to study both experimental and spontaneous metastases in several cancer entities (Ranjan et al., 2023; Ribatti, 2021). Several studies use *Alu* qPCR to detect metastatic dissemination of human cells in chick embryo organs (DeBord et al., 2018; Guller et al., 2021; Miquel et al., 2021). However, no studies have used the CAM model to detect the metastatic potential of murine cells. Since the *Alu* elements are unique for humans, *Alu* qPCR cannot be used to detect murine cell metastases in the chick embryo organs. Hence, in this study, *BI* qPCR was established to evaluate the metastatic potential of the murine cell lines. *BI* qPCR was sensitive enough to detect the presence of murine DNA as low as 0.0001 ng. However, in the presence of chick embryo DNA ≥ 0.1 ng, mild non-specific *BI* amplification was observed. Hence, for the evaluation of metastatic dissemination, the *BI* amplification from tumor-transplanted chick embryo organs was normalized to the *BI* amplification of the control chick embryo organs in which no transplantation was performed.

In this study, metastatic dissemination of the murine PDAC cells to chick embryo organs, selectively the brain, heart, and liver, was detected using *BI* qPCR. In the chick embryo brain, the cell line 12548, representing the quasi-mesenchymal PDAC subtype, showed significantly higher metastasis than the

cell lines 9366 and R405, representing the classical and basal PDAC subtypes. However, in the chick embryo liver, a significant difference in metastatic dissemination was observed between the cell lines 12548 and R405 representing the quasi-mesenchymal and basal PDAC subtypes, respectively. This observation was consistent with previous studies that showed that the quasi-mesenchymal and mesenchymal PDAC subtypes are associated with poor prognosis and worse clinical outcomes when compared to classical PDAC subtypes (Mueller et al., 2018; Orth et al., 2019; Zhou et al., 2021). However, in the chick embryo hearts, no significant differences in the metastatic dissemination were observed between the cell lines. Indicatively, there were no differences between the cell lines 9366, 12548, and R405 in intravasating into the microcirculatory system of the chick embryo. Intravasation is one of the important initial stages in metastatic dissemination, during which tumor cells detach from the primary tumor and enter blood vessels. This process is influenced by the migration potential of the tumor cells (Yamamoto et al., 2023). Even though the cell lines 9366, 12548, and R405 showed different modes of cell migration, no significant differences were observed between the *in vitro* migration potentials of the cell lines, confirming the intravasation observed *in ovo*.

PDAC is a desmoplastic cancer in which the majority of the tumor mass is composed of stroma containing various cellular and acellular components. CAFs being the major player in the desmoplastic stroma of PDAC, this study exploited the CAM model to study the infiltration of CAFs in CAM xenografts. With this aim, immunohistochemical characterization of the stroma was performed in CAM xenografts derived from the cell lines 9366, 12548, and R405. Immunohistochemical staining for chicken-specific Vimentin indicated the presence of CAFs in CAM xenografts. In addition, α -SMA and CK 19 co-staining confirmed the presence of α -SMA-positive myofibroblasts in CAM xenografts, which play a major role in ECM remodeling in PDAC stroma. Even though a similar degree of CAF infiltration was observed, as indicated by Vimentin staining, a significantly high amount of fibrillar collagen and hyaluronan deposition were observed in the CAM xenografts derived from the cell lines 12548 and R405, representing the quasi-mesenchymal and mesenchymal PDAC subtypes. Previous studies showed that fibrillar collagens predominantly restrain PDAC progression (Y. Chen et al., 2021; Madsen, 2021; Su et al., 2022). Similarly, the cell line 12548, showing the highest fibrillar collagen,

showed the lowest metastatic dissemination in chick embryo liver, whereas the cell line 9366, with the lowest fibrillar collagen deposition, showed the highest metastatic dissemination.

Several studies showed that hyaluronan promotes tumor progression and results in poor survival (Ho et al., 2020; Placencio-Hickok et al., 2022; Tahkola et al., 2021). The highest and lowest hyaluronan deposition were observed in the CAM xenografts derived from the cell lines 12548 and 9366, respectively. In correlation, the highest metastatic dissemination in the chick embryo brain was observed for the cell line 12548, whereas the lowest metastatic dissemination was observed for the cell line 9366 in the chick embryo brain. These observations suggest that the CAM model could be exploited to study the functional influence of the stroma on PDAC progression.

6.3 Characterization of selected cancer hallmarks in PDAC using the CAM PDX model

The PDO lines B250, B290, and B339, generated from surgical resections, and the PDO line B188, generated from endoscopic ultrasound-guided fine needle biopsy (EUS-FNB), were characterized genomically, transcriptomically, and morphologically and were used to establish CAM as an alternative PDX model. The PDO lines B188, B250, B290, and B339 harbor the most predominant *KRAS* G12D mutation in PDAC, whereas the PDO line B290 has the less predominant *KRAS* G12V mutation (He et al., 2022). According to the 30 most frequently mutated genes listed by the cBioPortal platform, the four PDO lines used in this study showed unique mutational profiles. Similar to murine PDAC cell lines, using PurIST, a single sample classifier based on a meta-analysis of the clinical utility of existing PDAC subtypes, the PDO lines were transcriptomically subtyped (Rashid et al., 2020). The PDO lines B250 and B290 were transcriptomically characterized as basal-like PDAC subtypes, whereas the PDO lines B188 and B339 were transcriptomically characterized as classical PDAC subtypes (Bailey et al., 2016; Chan-Seng-Yue et al., 2020; Collisson et al., 2011; Moffitt et al., 2015; Puleo et al., 2018). In contrast to the murine PDAC cell lines, the transcriptomic subtyping of the PDOs was not reflected in the morphology observed by phase contrast microscopy. Similarly, the cytoskeleton architecture of the PDO lines, as determined by Phalloidin staining, also did not reflect the transcriptomic subtyping. Using the morphologically, genomically, and transcriptomically characterized PDO lines B188, B250, B290, and B339, the CAM model was optimized as an alternative PDX model to study PDAC. Compared to the

murine PDAC cell lines, PDOs showed better engraftment on CAM, approximately 80% for all four PDO lines. PDOs are cultured in Matrigel *in vitro* and transplanted on CAM as Matrigel-embedded organoids. Since Matrigel supports polarization of the cells, thereby favoring epithelial growth of the cells, PDOs better engraft on CAM compared to the murine PDAC cell lines (Kakni et al., 2022). However, in contrast to the murine PDAC cell lines, no differences in tumor take rates were observed for the PDO lines B188, B250, B290, and B339.

PDOs retain the phenotype, genotype, and molecular and drug response profiles of the primary tumors (Romero-Calvo et al., 2019). Hence, several studies have developed PDX models by transplanting PDOs onto immune-compromised murine models for various cancer entities, including PDAC (Sereti et al., 2023). In addition, these studies showed that PDOs-derived xenografts recapitulated the histomorphological, molecular, and functional characteristic features of the primary tumors (E. Wang et al., 2022). Similarly, the transplantation of PDOs onto CAM gave rise to PDOs-derived xenografts, which recapitulated the histomorphological features of the primary tumors. However, these comparisons were made based on analyses of the H&E-stained primary tumor sections. Further validation by immunohistochemical subtyping using KRT81, HNF1A, and GATA6 expression is required to compare the subtypes represented in the CAM xenografts and patient tumors (Muckenhuber et al., 2018; O'Kane et al., 2020). In addition, grading the patient primary tumors and CAM xenografts also helps to check if the histomorphological features of the patient tumors are recapitulated in CAM xenografts. Even though transcriptomically the PDOs were subtyped as classical (B188 and B339) and basal (B250 and B290), the H&E-stained sections of the primary tumors did not show any morphologically distinct features based on the subtype characterization observed for the murine cells-derived CAM xenografts and endogenous mouse tumors.

Even though no significant differences in tumor take rates were observed between the PDO lines, significant differences in *in vitro* proliferation were observed for the PDO lines B188 and B250. However, *in ovo* proliferation of the PDO lines B188, B250, B290, and B339 characterized by Ki 67 staining did not show any significant differences, similar to the tumor take rates. This observation is

supported by previous studies that suggest that the proliferation index detected by Ki 67 staining is associated with successful tumor engraftment in PDX models (Tanaka et al., 2020).

CAM has been used as a model to study both experimental and spontaneous metastases of human cells in several cancer entities (Ranjan et al., 2023; Ribatti, 2021). Several studies use *Alu* qPCR to detect metastatic dissemination of human cells in chick embryo organs (DeBord et al., 2018; Guller et al., 2021; Miquel et al., 2021). Since the *Alu* elements are unique to the human genome, human cells that metastasize to chick embryo organs can be detected by *Alu* qPCR. Hence, using *Alu* qPCR, the metastatic dissemination of PDOs to chick embryo organs, selectively the brain, heart, and liver, was determined. Similar to *Bl* qPCR, the amplification of *Alu* elements from tumor-transplanted chick embryo organs was normalized to that of the control chick embryo organs in which no transplantation was performed. Though metastatic dissemination of all the PDO lines was detected in the chick embryo brain, no significant differences were observed between the PDO lines. Similarly, metastatic dissemination of all the PDO lines was detected in the chick embryo liver. However, significant differences were observed only between the PDO lines B250 and B290. Similar to the chick embryo brain and liver, metastatic dissemination of all the PDO lines was detected in the chick embryo heart as well. A significant difference was observed only between the PDO lines B188 and B290, indicating the difference in the intravasation potential of these PDO lines into the microcirculatory system of the chick embryo. Intravasation is one of the important initial stages in metastatic dissemination, during which tumor cells detach from the primary tumor and enter blood vessels. This process is influenced by the migration potential of the tumor cells (Yamamoto et al., 2023). Even though the PDO lines B188, B250, B290, and B339 showed a collective mode of migration *in vitro*, significant differences in the *in vitro* migration potential were observed between the PDO lines. In contrast to the *in ovo* intravasation observed, the PDO line B188 showed significantly low *in vitro* migratory potential compared to the other PDO lines, whereas PDO lines B250 and B290 showed significantly high *in vitro* migratory potential compared to other PDO lines in 24 hours. The PDO line B339 showed an intermediate *in vitro* migratory potential, which was significantly higher than the PDO line B188 but lower than the PDO lines B250 and B290. The differences in *in vitro* migration and *in ovo* intravasation potential could be

explained by the influence of the stroma recruited by each PDO line in the *in ovo* model. The stroma recruited by B188 in the CAM xenografts might have promoted the *in ovo* intravasation potential of the PDO line B188. In contrast, the stroma recruited by the PDO lines B250, B290, and B339 in the CAM xenografts might have restrained the *in ovo* intravasation potential.

Similar to the CAM xenografts derived from murine cells, stromal characterization was performed on the PDOs-derived CAM xenografts. Immunohistochemical staining for chicken-specific Vimentin indicated the presence of CAFs in CAM xenografts derived from the PDO lines. In addition, α -SMA and CK 19 co-staining confirmed the presence of α -SMA positive myofibroblasts in the PDOs-derived CAM xenografts, which play a significant role in ECM remodeling in PDAC stroma. Even though a similar degree of CAF infiltration was observed, as indicated by Vimentin staining, each PDO line showed different degrees of fibrillar collagen and hyaluronan deposition. The highest amount of fibrillar collagen deposition was observed in B339 CAM xenografts, whereas the lowest fibrillar collagen deposition was observed in B188 CAM xenografts.

On the other hand, the highest hyaluronan deposition was observed in the CAM xenografts derived from the PDO line B188. In contrast, the lowest hyaluronan deposition was observed in the CAM xenografts derived from the PDO line B339. These observations correlated with the lowest *in vitro* migration potential and the highest *in ovo* intravasation potential of the PDO line B188. Similarly, the hyaluronan deposition was also associated with increased *in vitro* migration potential and low *in ovo* intravasation of the PDO line B290. Even though a similar degree of fibrillar collagen and hyaluronan deposition was observed for the PDO lines B250 and B290, a significant difference was observed in the metastatic dissemination to chick embryo liver. This observation showed the complexity of ECM deposition beyond fibrillar collagen and hyaluronan content in PDAC stroma. These observations suggest that the CAM model could be used as a personalized platform to study the functional influence of the stroma on PDAC progression.

7. Conclusion and Future Perspectives

In conclusion, this study optimized the CAM model to study major hallmarks of PDAC, focusing on the subtypes using KPC mouse-derived cells. In addition, this study also optimized CAM as an alternative PDX model to study PDAC in a personalized manner. To further strengthen the application of the model, more cell lines representing each PDAC subtype have to be included. Similarly, increasing the PDO cohort will also enhance the application of CAM as an alternative PDX model. The transplantation method using the Matrigel droplet approach favored tumor engraftment and growth of epithelial PDAC cell lines compared to the quasi-mesenchymal and mesenchymal PDAC cell lines. Injecting tumor cells directly into CAM circulation might be an alternative transplantation approach to test tumor engraftment and growth on CAM without favoring epithelial PDAC cell line engraftment. Histological studies and comparisons of the CAM xenografts with respective endogenous mouse tumors or patient tumors were made based on the H&E staining. More detailed histological analyses by comparing the tumor grades as well as immunohistochemical subtyping will further validate the histomorphological features observed in the CAM xenografts. Even though *B1* and *Alu* qPCR allowed the detection of murine cells and PDOs that metastasized to chick embryo organs, histological validation is required to confirm colony formation in the distant organs. In addition to metastatic dissemination, tumor invasion can also be studied in CAM xenografts by quantifying the tumor buds.

This study showed that the CAM model can also be used to study the stroma, focusing on CAFs, a functionally crucial cellular component of the PDAC stroma. However, the focus of the study was limited to myCAF, a significant ECM-producing subpopulation of CAFs. Detailed characterization of the stroma, including other CAF subpopulations such as iCAF and apCAF in CAM xenografts, will further validate the application of CAM to study the stroma and its functional role in PDAC progression. In summary, this study showed that CAM can be used as a reliable alternative model to study the major hallmarks of PDAC. In the future, the CAM model can be exploited further to perform antimetastatic drug testing and genetic screens in a scalable fashion.

8. Acknowledgment

This doctoral thesis project has been a great experience in my academics. With the support and guidance of the following people, this project was completed. It is to them that I owe my deepest gratitude.

Firstly, I would like to thank Prof. Dr. Maximilian Reichert for allowing me to join his research group and to conduct research on such an exciting topic for my PhD thesis. His constant guidance, support, and ideas provided new perspectives for the thesis. My sincere thanks to Prof. Dr. Dieter Saur and PD. Dr. Roman Nawroth, who kindly accepted to be my thesis committee members and provided valuable feedback for this project.

My special thanks to Aashreya for her great support in not just finishing the project successfully but also for valuable scientific discussions and all the fun times in the lab. Many thanks to Valentina for her support and for providing helpful suggestions that helped the project a lot. I am very grateful to Aashreya and Valentina for creating a healthy and friendly atmosphere in the lab, which led to open discussions about the projects and sharing each other's experiences and knowledge.

I want to thank all my colleagues, Laura, Sabrina, Akul, Aurora, Aris, and Martin from AG Reichert, for their support. I am also thankful to all the collaborators for their help in successfully finishing this project.

I want to express my special thanks to all the fantastic friends I made during this journey: Aashreya, Steffi, Saumya, Sruthi, and Hilansi, who have always been helpful whenever I needed support and made this PhD journey more pleasant.

Last but not least, I want to express my deepest gratitude to my parents, sisters, Conny, Oma, Saaron, and his family for their constant support and encouragement, without whom this achievement is impossible.

Publications, presentations, and awards

8.1 Publications

- The Chorioallantoic Membrane Xenograft Assay as a Reliable Model for Investigating the Biology of Breast Cancer. *Cancers* 2023, 15, 1704.
Raphela A. Ranjan, Julienne K. Muenzner, Philipp Kunze, Carol I. Geppert, Matthias Ruebner, Hanna Huebner, Peter A. Fasching, Matthias W. Beckmann, Tobias Bäuerle, Arndt Hartmann, Wolfgang Walther, Markus Eckstein, Ramona Erber and Regine Schneider-Stock (2023).
- Mesenchymal Plasticity Regulated by Prrx1 Drives Aggressive Pancreatic Cancer Biology. *Gastroenterology*; 160:346–385.
Feldmann K, Maurer C, Peschke K, Teller S, Schuck K, Steiger K, Engleitner T, Öllinger R, Nomura A, Wirges N, Papargyriou A, Sarker RSJ, **Ranjan RA**, Dantes Z, Weichert W, Rustgi AK, Schmid RM, Rad R, Schneider G, Saur D, Reichert M. (2021).
- Implementing cell-free DNA of pancreatic cancer patient-derived organoids for personalized oncology. *JCI Insight* 5 (15): e137809.
Dantes Z, Yen HY, Pfarr N, Winter C, Steiger K, Muckenhuber A, Hennig A, Lange S, Engleitner T, Öllinger R, Maresch R, Orben F, Heid I, Georgios Kaissis, Shi K, Topping G, Stögbauer F, Wirth M, Peschke K, Papargyriou A, Rezaee-Oghazi M, Feldmann K, Schäfer APG, **Ranjan R**, Lubeseder-Martellato C, Stange DE, Welch T, Martingnoni M, Ceyhan GO, Friess H, Herner A, Liotta L, Treiber M, von Figura G, Abdelhafez M, Klare P, Schlag C, Algül H, Siveke J, Braren R, Weirich G, Weichert W, Saur D, Rad R, Schmid RM, Schneider G, Reichert M. (2020).

8.2 Oral presentations

- An *in ovo* model to study tumor morphogenesis and metastatic dissemination of PDAC (DPC 2023).
R. Ranjan, A. Ravichandra, P.H. Heuschneider, S. Bärthel, K. Steiger, W. Weichert, D. Saur, M. Reichert
- Engrafting patient-derived organoids on chick embryo chorioallantoic membranes—an alternative *in vivo* model system for human pancreatic adenocarcinoma (Med II retreat 2019).
Raphela Ranjan, Katja Steiger, Wilko Weichert, Dieter Saur, Maximilian Reichert.

8.3 Poster presentations

- An *in ovo* model to study tumor morphogenesis and metastatic dissemination of PDAC (EPC 2023).
Raphela Ranjan, Aashreya Ravichandra, Peer Heuschneider, Stefanie Bärthel, Katja Steiger, Wilko Weichert, Dieter Saur, Carlo Maurer, Anna Melissa Schlitter, Maximilian Reichert.
- Cancer-associated fibroblast plasticity in intrahepatic cholangiocarcinoma (EASL ILC 2023).

A. Ravichandra, **R. Ranjan**, N. B. Khaled, D. Hartmann, N. H. Hüser, C. Maurer, R. Rad, J. Mayerle, K. Steiger, R. Schmid, M. Reichert.

- Modeling functional heterogeneity using branched pancreatic cancer-derived organoids reveals contractile phenotypes independent of driver mutation (DDW 2023).
Sophia S. Schirmer, Aristeidis Papargyriou, Laura Schmidleitner, **Raphela A. Ranjan**, Sebastian Mueller, Roland, Dieter Saur, Maximilian Reichert.
- An *in ovo* system to study tumor morphogenesis and metastatic dissemination of pancreatic cancer patient-derived organoids (DPC 2022).
R. Ranjan, K. Steiger, R. Schmid, M. Reichert.
- Engrafting pancreatic cancer patient-derived organoids on chick embryo chorioallantoic membranes—an *in ovo* system to study tumor morphogenesis and metastatic dissemination of organoids (MGC 2021).
R. Ranjan, K. Steiger, R. Schmid, M. Reichert.
- Engrafting patient-derived organoids on chick embryo chorioallantoic membranes—an alternative *in vivo* model system for human pancreatic adenocarcinoma (DPC 2020).
R. Ranjan, K. Steiger, R. Schmid, M. Reichert.

8.4 Awards

- Poster Award: An *in ovo* system to study tumor morphogenesis and metastatic dissemination of pancreatic cancer patient-derived organoids (MGC Science Day, 2021).

9. List of figures

| | |
|---|----|
| Figure 1: Stepwise progression model of PDAC. | 3 |
| Figure 2: Formation and growth of CAM during chick embryo development..... | 12 |
| Figure 3: <i>In ovo</i> and <i>ex ovo</i> CAM models..... | 13 |
| Figure 4: CAM assay workflow. | 47 |
| Figure 5: Morphological characterization of KPC mouse-derived cell lines by phase contrast microscopy. | 56 |
| Figure 6: Morphological characterization of KPC mouse-derived cell lines by F-actin staining. | 57 |
| Figure 7: Transcriptomic characterization of KPC mouse-derived cell lines based on the PurIST single sample classifier. | 58 |
| Figure 8: Establishment of the workflow using KPC mouse-derived cell lines representing distinct PDAC subtypes. | 59 |
| Figure 9: Tumor take rates of KPC mouse-derived cell lines on CAM. | 61 |
| Figure 10: General histology of the CAM tumors in which the tumor area, CAM, and blood vessels within the tumor area and CAM were easily distinguished..... | 62 |
| Figure 11: Comparison of the histomorphological features in CAM and endogenous mouse tumors.. | 63 |
| Figure 12: Characterization of tumor proliferation in CAM xenografts. | 64 |
| Figure 13: <i>In vitro</i> proliferation of the cell lines 9366, 12548, and R405..... | 65 |
| Figure 14: <i>BI</i> qPCR establishment..... | 66 |
| Figure 15: Metastatic dissemination in the chick embryo brain..... | 67 |
| Figure 16: Metastatic dissemination in the chick embryo heart. | 68 |
| Figure 17: Metastatic dissemination in chick embryo liver. | 69 |
| Figure 18: <i>In vitro</i> migration potential of the cell lines..... | 70 |
| Figure 19: Stromal infiltration in CAM xenografts..... | 71 |
| Figure 20: Vimentin staining showing the pan-CAF population in CAM xenografts. | 72 |
| Figure 21: α -SMA and CK 19 co-staining showing the presence of α -SMA positive fibroblast infiltration in CAM xenografts..... | 74 |

| | |
|--|-----|
| Figure 22: Sirius red staining showing fibrillar collagen deposition in CAM xenografts..... | 75 |
| Figure 23: HABP staining showing the hyaluronan deposition in CAM xenografts. | 77 |
| Figure 24: Morphological characterization of PDOs by phase contrast microscopy. | 79 |
| Figure 25: Morphological characterization of PDOs by F-actin staining..... | 80 |
| Figure 26: Mutation profile of the PDO lines. | 81 |
| Figure 27: Transcriptomic characterization of PDOs..... | 82 |
| Figure 28: Growth rates of the PDO lines. | 84 |
| Figure 29: Optimization of PDO seeding density on CAM. | 84 |
| Figure 30: Establishment of the workflow using PDOs. | 85 |
| Figure 31: Tumor take rates of PDO lines on CAM..... | 86 |
| Figure 32: General histology of the CAM tumors, in which the tumor area, CAM, and blood vessels within the tumor area and CAM were easily distinguished..... | 87 |
| Figure 33: Comparison of the histomorphological features of CAM and patient tumors. | 88 |
| Figure 34: Characterization of tumor proliferation in CAM xenografts. | 90 |
| Figure 35: Metastatic dissemination in the chick embryo brain..... | 91 |
| Figure 36: Metastatic dissemination in chick embryo heart..... | 92 |
| Figure 37: Metastatic dissemination in chick embryo liver. | 93 |
| Figure 38: <i>In vitro</i> migration potential of the B188, B250, B290, and B339 2D cell lines..... | 94 |
| Figure 39: Stromal infiltration in CAM xenografts..... | 96 |
| Figure 40: Vimentin staining showing the pan-CAF population in CAM xenografts | 97 |
| Figure 41: α -SMA and CK 19 co-staining shows the presence of α -SMA positive fibroblast infiltration in CAM xenografts..... | 98 |
| Figure 42: Sirius red staining showing fibrillar collagen deposition in CAM xenografts..... | 99 |
| Figure 43: HABP staining showing the hyaluronan deposition in CAM xenografts | 101 |

10. List of tables

| | |
|--|----|
| Table 1: Equipments used in the study..... | 18 |
| Table 2: Consumables used in the study | 20 |
| Table 3: Consumables and reagents used in the study | 23 |
| Table 4: Buffers and solutions used in the study..... | 26 |
| Table 5: Antibodies used in the study | 26 |
| Table 6: Commercial kits used in the study | 27 |
| Table 7: Cell culture media and composition used in the study..... | 29 |
| Table 8: Cell lines used in the study..... | 30 |
| Table 9: Software used in the study | 31 |
| Table 10: Reaction mix for human <i>KRAS</i> amplification | 36 |
| Table 11: PCR protocol for human <i>KRAS</i> amplification..... | 37 |
| Table 12: PCR reaction mix for mycoplasma contamination test..... | 39 |
| Table 13: PCR protocol for mycoplasma contamination test..... | 39 |
| Table 14: qPCR reaction mix for metastasis quantification..... | 53 |
| Table 15: <i>Alu</i> and <i>chGAPDH</i> qPCR protocol | 53 |
| Table 16: <i>BI</i> qPCR protocol..... | 55 |
| Table 17: Symbols denoting p-value ranges | 55 |
| Table 18: Sample of origin and <i>KRAS</i> mutational status of selected PDOs..... | 78 |

11. References

- Alhobayb, T., Peravali, R., & Ashkar, M. (2021). The Relationship between Acute and Chronic Pancreatitis with Pancreatic Adenocarcinoma: Review. *Diseases*, *9*(4). doi:10.3390/diseases9040093
- Alvarez, M. J., Shen, Y., Giorgi, F. M., Lachmann, A., Ding, B. B., Ye, B. H., & Califano, A. (2016). Functional characterization of somatic mutations in cancer using network-based inference of protein activity. *Nat Genet*, *48*(8), 838-847. doi:10.1038/ng.3593
- Ames, J. J., Henderson, T., Liaw, L., & Brooks, P. C. (2016). Methods for Analyzing Tumor Angiogenesis in the Chick Chorioallantoic Membrane Model. *Methods Mol Biol*, *1406*, 255-269. doi:10.1007/978-1-4939-3444-7_22
- Ando, R., Sakai, A., Iida, T., Kataoka, K., Mizutani, Y., & Enomoto, A. (2022). Good and Bad Stroma in Pancreatic Cancer: Relevance of Functional States of Cancer-Associated Fibroblasts. *Cancers (Basel)*, *14*(14). doi:10.3390/cancers14143315
- Andriesi-Rusu, F.-D., Trofin, A. M., Cianga-Spiridon, I. A., Vlad, N., Vasilescu, A. M., Târcoveanu, E., & Lupaşcu, C. (2019). Ki 67 as Prognostic Factor in Surgically Resected Pancreatic Ductal Adenocarcinoma. *The Journal of Surgery*, *15*, 1-3.
- Augustine, R., Alhussain, H., Hasan, A., Badie Ahmed, M., H, C. Y., & Al Moustafa, A. E. (2020). A novel in ovo model to study cancer metastasis using chicken embryos and GFP expressing cancer cells. *Bosn J Basic Med Sci*, *20*(1), 140-148. doi:10.17305/bjbms.2019.4372
- Bailey, P., Chang, D. K., Nones, K., Johns, A. L., Patch, A. M., Gingras, M. C., Grimmond, S. M. (2016). Genomic analyses identify molecular subtypes of pancreatic cancer. *Nature*, *531*(7592), 47-52. doi:10.1038/nature16965
- Barbosa, M. A. G., Xavier, C. P. R., Pereira, R. F., Petrikaite, V., & Vasconcelos, M. H. (2021). 3D Cell Culture Models as Recapitulators of the Tumor Microenvironment for the Screening of Anti-Cancer Drugs. *Cancers (Basel)*, *14*(1). doi:10.3390/cancers14010190
- Barnett, S. E., Herrmann, A., Shaw, L., Gash, E. N., Poptani, H., Sacco, J. J., & Coulson, J. M. (2022). The Chick Embryo Xenograft Model for Malignant Pleural Mesothelioma: A Cost and Time Efficient 3Rs Model for Drug Target Evaluation. *Cancers (Basel)*, *14*(23). doi:10.3390/cancers14235836
- Biankin, A. V., Kench, J. G., Colvin, E. K., Segara, D., Scarlett, C. J., Nguyen, N. Q., Network, N. S. W. P. C. (2009). Expression of S100A2 calcium-binding protein predicts response to pancreatectomy for pancreatic cancer. *Gastroenterology*, *137*(2), 558-568, 568 e551-511. doi:10.1053/j.gastro.2009.04.009
- Biffi, G., Oni, T. E., Spielman, B., Hao, Y., Elyada, E., Park, Y., Tuveson, D. A. (2019). IL1-Induced JAK/STAT Signaling Is Antagonized by TGFbeta to Shape CAF Heterogeneity in Pancreatic Ductal Adenocarcinoma. *Cancer Discov*, *9*(2), 282-301. doi:10.1158/2159-8290.CD-18-0710
- Bleijns, M., van de Wetering, M., Clevers, H., & Drost, J. (2019). Xenograft and organoid model systems in cancer research. *EMBO J*, *38*(15), e101654. doi:10.15252/embj.2019101654
- Boyd, L. N. C., Andini, K. D., Peters, G. J., Kazemier, G., & Giovannetti, E. (2022). Heterogeneity and plasticity of cancer-associated fibroblasts in the pancreatic tumor microenvironment. *Semin Cancer Biol*, *82*, 184-196. doi:10.1016/j.semcancer.2021.03.006

- Butler, K. S., Brinker, C. J., & Leong, H. S. (2022). Bridging the In Vitro to In Vivo gap: Using the Chick Embryo Model to Accelerate Nanoparticle Validation and Qualification for In Vivo studies. *ACS Nano*, *16*(12), 19626-19650. doi:10.1021/acsnano.2c03990
- Cancer Genome Atlas Research Network. Electronic address, a. a. d. h. e., & Cancer Genome Atlas Research, N. (2017). Integrated Genomic Characterization of Pancreatic Ductal Adenocarcinoma. *Cancer Cell*, *32*(2), 185-203 e113. doi:10.1016/j.ccell.2017.07.007
- Chan-Seng-Yue, M., Kim, J. C., Wilson, G. W., Ng, K., Figueroa, E. F., O'Kane, G. M., Notta, F. (2020). Author Correction: Transcription phenotypes of pancreatic cancer are driven by genomic events during tumor evolution. *Nat Genet*, *52*(4), 463. doi:10.1038/s41588-020-0588-3
- Chen, L., Wang, S., Feng, Y., Zhang, J., Du, Y., Zhang, J., Li, Y. (2021). Utilisation of Chick Embryo Chorioallantoic Membrane as a Model Platform for Imaging-Navigated Biomedical Research. *Cells*, *10*(2). doi:10.3390/cells10020463
- Chen, Y., Kim, J., Yang, S., Wang, H., Wu, C. J., Sugimoto, H., Kalluri, R. (2021). Type I collagen deletion in alphaSMA(+) myofibroblasts augments immune suppression and accelerates progression of pancreatic cancer. *Cancer Cell*, *39*(4), 548-565 e546. doi:10.1016/j.ccell.2021.02.007
- Chu, P. Y., Koh, A. P., Antony, J., & Huang, R. Y. (2022). Applications of the Chick Chorioallantoic Membrane as an Alternative Model for Cancer Studies. *Cells Tissues Organs*, *211*(2), 222-237. doi:10.1159/000513039
- Collisson, E. A., Bailey, P., Chang, D. K., & Biankin, A. V. (2019). Molecular subtypes of pancreatic cancer. *Nat Rev Gastroenterol Hepatol*, *16*(4), 207-220. doi:10.1038/s41575-019-0109-y
- Collisson, E. A., Sadanandam, A., Olson, P., Gibb, W. J., Truitt, M., Gu, S., Gray, J. W. (2011). Subtypes of pancreatic ductal adenocarcinoma and their differing responses to therapy. *Nat Med*, *17*(4), 500-503. doi:10.1038/nm.2344
- Connor, A. A., & Gallinger, S. (2022). Pancreatic cancer evolution and heterogeneity: integrating omics and clinical data. *Nat Rev Cancer*, *22*(3), 131-142. doi:10.1038/s41568-021-00418-1
- DeBord, L. C., Pathak, R. R., Villaneuva, M., Liu, H. C., Harrington, D. A., Yu, W., Sikora, A. G. (2018). The chick chorioallantoic membrane (CAM) as a versatile patient-derived xenograft (PDX) platform for precision medicine and preclinical research. *Am J Cancer Res*, *8*(8), 1642-1660.
- Diaz, K. E., & Lucas, A. L. (2019). Familial Pancreatic Ductal Adenocarcinoma. *Am J Pathol*, *189*(1), 36-43. doi:10.1016/j.ajpath.2018.06.026
- Digiacomio, G., Volta, F., Garajova, I., Balsano, R., & Cavazzoni, A. (2021). Biological Hallmarks and New Therapeutic Approaches for the Treatment of PDAC. *Life (Basel)*, *11*(8). doi:10.3390/life11080843
- Doke, S. K., & Dhawale, S. C. (2015). Alternatives to animal testing: A review. *Saudi Pharm J*, *23*(3), 223-229. doi:10.1016/j.jsps.2013.11.002
- Dombre, C., Guyot, N., Moreau, T., Monget, P., Da Silva, M., Gautron, J., & Rehault-Godbert, S. (2017). Egg serpins: The chicken and/or the egg dilemma. *Semin Cell Dev Biol*, *62*, 120-132. doi:10.1016/j.semcdb.2016.08.019

- Dreyer, S. B., Pinese, M., Jamieson, N. B., Scarlett, C. J., Colvin, E. K., Pajic, M., Glasgow Precision Oncology, L. (2020). Precision Oncology in Surgery: Patient Selection for Operable Pancreatic Cancer. *Ann Surg*, 272(2), 366-376. doi:10.1097/SLA.0000000000003143
- Eckrich, J., Kugler, P., Buhr, C. R., Ernst, B. P., Mendler, S., Baumgart, J., Wiesmann, N. (2020). Monitoring of tumor growth and vascularization with repetitive ultrasonography in the chicken chorioallantoic-membrane-assay. *Sci Rep*, 10(1), 18585. doi:10.1038/s41598-020-75660-y
- Ehlen, L., Arndt, J., Treue, D., Bischoff, P., Loch, F. N., Hahn, E. M., Kamphues, C. (2020). Novel methods for in vitro modeling of pancreatic cancer reveal important aspects for successful primary cell culture. *BMC Cancer*, 20(1), 417. doi:10.1186/s12885-020-06929-8
- Elyada, E., Bolisetty, M., Laise, P., Flynn, W. F., Courtois, E. T., Burkhart, R. A., Tuveson, D. A. (2019). Cross-Species Single-Cell Analysis of Pancreatic Ductal Adenocarcinoma Reveals Antigen-Presenting Cancer-Associated Fibroblasts. *Cancer Discov*, 9(8), 1102-1123. doi:10.1158/2159-8290.CD-19-0094
- Fahmy, K., Gonzalez, A., Arafa, M., Peixoto, P., Bellahcene, A., Turtoi, A., Peulen, O. (2016). Myoferlin plays a key role in VEGFA secretion and impacts tumor-associated angiogenesis in human pancreas cancer. *Int J Cancer*, 138(3), 652-663. doi:10.1002/ijc.29820
- Faihs, L., Firouz, B., Slezak, P., Slezak, C., Weissensteiner, M., Ebner, T., Dungel, P. (2022). A Novel Artificial Intelligence-Based Approach for Quantitative Assessment of Angiogenesis in the Ex Ovo CAM Model. *Cancers (Basel)*, 14(17). doi:10.3390/cancers14174273
- Feldmann, K., Maurer, C., Peschke, K., Teller, S., Schuck, K., Steiger, K., Reichert, M. (2021). Mesenchymal Plasticity Regulated by Prrx1 Drives Aggressive Pancreatic Cancer Biology. *Gastroenterology*, 160(1), 346-361 e324. doi:10.1053/j.gastro.2020.09.010
- Ferreira, R. M. M., Sancho, R., Messal, H. A., Nye, E., Spencer-Dene, B., Stone, R. K., Behrens, A. (2017). Duct- and Acinar-Derived Pancreatic Ductal Adenocarcinomas Show Distinct Tumor Progression and Marker Expression. *Cell Rep*, 21(4), 966-978. doi:10.1016/j.celrep.2017.09.093
- Fischer, C. G., & Wood, L. D. (2018). From somatic mutation to early detection: insights from molecular characterization of pancreatic cancer precursor lesions. *J Pathol*, 246(4), 395-404. doi:10.1002/path.5154
- Flowers, B. M., Xu, H., Mulligan, A. S., Hanson, K. J., Seoane, J. A., Vogel, H., Attardi, L. D. (2021). Cell of Origin Influences Pancreatic Cancer Subtype. *Cancer Discov*, 11(3), 660-677. doi:10.1158/2159-8290.CD-20-0633
- Franchi, M., Karamanos, K. A., Cappadone, C., Calonghi, N., Greco, N., Franchi, L., Masola, V. (2023). Colorectal Cancer Cell Invasion and Functional Properties Depend on Peri-Tumoral Extracellular Matrix. *Biomedicines*, 11(7). doi:10.3390/biomedicines11071788
- Garcia-Gareta, E., Binkowska, J., Kohli, N., & Sharma, V. (2020). Towards the Development of a Novel Ex Ovo Model of Infection to Pre-Screen Biomaterials Intended for Treating Chronic Wounds. *J Funct Biomater*, 11(2). doi:10.3390/jfb11020037
- Garcia, P. L., Miller, A. L., & Yoon, K. J. (2020). Patient-Derived Xenograft Models of Pancreatic Cancer: Overview and Comparison with Other Types of Models. *Cancers (Basel)*, 12(5). doi:10.3390/cancers12051327

- Goto, T. (2020). Patient-Derived Tumor Xenograft Models: Toward the Establishment of Precision Cancer Medicine. *J Pers Med*, *10*(3). doi:10.3390/jpm10030064
- Guller, A., Kuschnerus, I., Rozova, V., Nadort, A., Yao, Y., Khabir, Z., Zvyagin, A. V. (2021). Chick Embryo Experimental Platform for Micrometastases Research in a 3D Tissue Engineering Model: Cancer Biology, Drug Development, and Nanotechnology Applications. *Biomedicines*, *9*(11). doi:10.3390/biomedicines9111578
- Gundel, B., Liu, X., Lohr, M., & Heuchel, R. (2021). Pancreatic Ductal Adenocarcinoma: Preclinical in vitro and ex vivo Models. *Front Cell Dev Biol*, *9*, 741162. doi:10.3389/fcell.2021.741162
- Halgrain, M., Bernardet, N., Crepeau, M., Meme, N., Narcy, A., Hincke, M., & Rehault-Godbert, S. (2022). Eggshell decalcification and skeletal mineralization during chicken embryonic development: defining candidate genes in the chorioallantoic membrane. *Poult Sci*, *101*(2), 101622. doi:10.1016/j.psj.2021.101622
- Han, C., Liu, T., & Yin, R. (2020). Biomarkers for cancer-associated fibroblasts. *Biomark Res*, *8*(1), 64. doi:10.1186/s40364-020-00245-w
- He, Q., Liu, Z., & Wang, J. (2022). Targeting KRAS in PDAC: A New Way to Cure It? *Cancers (Basel)*, *14*(20). doi:10.3390/cancers14204982
- Heitmeir, B., Deniz, M., Janni, W., Rack, B., Schochter, F., & Wiesmuller, L. (2022). Circulating Tumor Cells in Breast Cancer Patients: A Balancing Act between Stemness, EMT Features and DNA Damage Responses. *Cancers (Basel)*, *14*(4). doi:10.3390/cancers14040997
- Herting, C. J., Karpovsky, I., & Lesinski, G. B. (2021). The tumor microenvironment in pancreatic ductal adenocarcinoma: current perspectives and future directions. *Cancer Metastasis Rev*, *40*(3), 675-689. doi:10.1007/s10555-021-09988-w
- Hessmann, E., Buchholz, S. M., Demir, I. E., Singh, S. K., Gress, T. M., Ellenrieder, V., & Neesse, A. (2020). Microenvironmental Determinants of Pancreatic Cancer. *Physiol Rev*, *100*(4), 1707-1751. doi:10.1152/physrev.00042.2019
- Hingorani, S. R., Petricoin, E. F., Maitra, A., Rajapakse, V., King, C., Jacobetz, M. A., Tuveson, D. A. (2003). Preinvasive and invasive ductal pancreatic cancer and its early detection in the mouse. *Cancer Cell*, *4*(6), 437-450. doi:10.1016/s1535-6108(03)00309-x
- Hingorani, S. R., Wang, L., Multani, A. S., Combs, C., Deramaudt, T. B., Hruban, R. H., Tuveson, D. A. (2005). Trp53R172H and KrasG12D cooperate to promote chromosomal instability and widely metastatic pancreatic ductal adenocarcinoma in mice. *Cancer Cell*, *7*(5), 469-483. doi:10.1016/j.ccr.2005.04.023
- Ho, W. J., Jaffee, E. M., & Zheng, L. (2020). The tumour microenvironment in pancreatic cancer - clinical challenges and opportunities. *Nat Rev Clin Oncol*, *17*(9), 527-540. doi:10.1038/s41571-020-0363-5
- Hosein, A. N., Brekken, R. A., & Maitra, A. (2020). Pancreatic cancer stroma: an update on therapeutic targeting strategies. *Nat Rev Gastroenterol Hepatol*, *17*(8), 487-505. doi:10.1038/s41575-020-0300-1
- Hruban, R. H., Goggins, M., Parsons, J., & Kern, S. E. (2000). Progression model for pancreatic cancer. *Clin Cancer Res*, *6*(8), 2969-2972. Retrieved from <https://www.ncbi.nlm.nih.gov/pubmed/10955772>

- Hu, J., Ishihara, M., Chin, A. I., & Wu, L. (2019). Establishment of xenografts of urological cancers on chicken chorioallantoic membrane (CAM) to study metastasis. *Precis Clin Med*, 2(3), 140-151. doi:10.1093/pcmedi/pbz018
- Huang, B. Z., Stram, D. O., Le Marchand, L., Haiman, C. A., Wilkens, L. R., Pandol, S. J., Setiawan, V. W. (2019). Interethnic differences in pancreatic cancer incidence and risk factors: The Multiethnic Cohort. *Cancer Med*, 8(7), 3592-3603. doi:10.1002/cam4.2209
- Huang, H., Wang, Z., Zhang, Y., Pradhan, R. N., Ganguly, D., Chandra, R., Brekken, R. A. (2022). Mesothelial cell-derived antigen-presenting cancer-associated fibroblasts induce expansion of regulatory T cells in pancreatic cancer. *Cancer Cell*, 40(6), 656-673 e657. doi:10.1016/j.ccell.2022.04.011
- Javed, S., Soukhthezari, S., Fernandes, N., & Williams, K. C. (2022). Longitudinal bioluminescence imaging to monitor breast tumor growth and treatment response using the chick chorioallantoic membrane model. *Sci Rep*, 12(1), 17192. doi:10.1038/s41598-022-20854-9
- Jian, M., Ren, L., He, G., Lin, Q., Tang, W., Chen, Y., Xu, J. (2020). A novel patient-derived organoids-based xenografts model for preclinical drug response testing in patients with colorectal liver metastases. *J Transl Med*, 18(1), 234. doi:10.1186/s12967-020-02407-8
- Kakni, P., Lopez-Iglesias, C., Truckenmuller, R., Habibovic, P., & Giselbrecht, S. (2022). Reversing Epithelial Polarity in Pluripotent Stem Cell-Derived Intestinal Organoids. *Front Bioeng Biotechnol*, 10, 879024. doi:10.3389/fbioe.2022.879024
- Kleeff, J., Korc, M., Apte, M., La Vecchia, C., Johnson, C. D., Biankin, A. V., Neoptolemos, J. P. (2016). Pancreatic cancer. *Nat Rev Dis Primers*, 2, 16022. doi:10.1038/nrdp.2016.22
- Kolde, R. (2019). Pheatmap: pretty heatmaps. *R package version*, 1(2), 726.
- Komatsu, A., Higashi, Y., & Matsumoto, K. (2019). Various CAM tumor models. *Enzymes*, 46, 37-57. doi:10.1016/bs.enz.2019.10.001
- Kunz, P., Schenker, A., Sahr, H., Lehner, B., & Fellenberg, J. (2019). Optimization of the chicken chorioallantoic membrane assay as reliable in vivo model for the analysis of osteosarcoma. *PLoS One*, 14(4), e0215312. doi:10.1371/journal.pone.0215312
- Lattouf, R., Younes, R., Lutomski, D., Naaman, N., Godeau, G., Senni, K., & Changotade, S. (2014). Picrosirius red staining: a useful tool to appraise collagen networks in normal and pathological tissues. *J Histochem Cytochem*, 62(10), 751-758. doi:10.1369/0022155414545787
- LC, D., RR, P., Villaneuva M, L. H., & W, H. D. Y. (2018). The chick chorioallantoic membrane (CAM) as a versatile patient-derived xenograft (PDX) platform for precision medicine and preclinical research. *Am J Cancer Res*.
- Leupold, J. H., Patil, N., & Allgayer, H. (2021). The Chicken Egg Chorioallantoic Membrane (CAM) Model as an In Vivo Method for the Investigation of the Invasion and Metastasis Cascade of Malignant Tumor Cells. *Methods Mol Biol*, 2294, 17-26. doi:10.1007/978-1-0716-1350-4_2
- Li, S., & Xie, K. (2022). Ductal metaplasia in pancreas. *Biochim Biophys Acta Rev Cancer*, 1877(2), 188698. doi:10.1016/j.bbcan.2022.188698

- Lomberk, G., Blum, Y., Nicolle, R., Nair, A., Gaonkar, K. S., Marisa, L., Urrutia, R. (2018). Distinct epigenetic landscapes underlie the pathobiology of pancreatic cancer subtypes. *Nat Commun*, *9*(1), 1978. doi:10.1038/s41467-018-04383-6
- Macosko, E. Z., Basu, A., Satija, R., Nemesh, J., Shekhar, K., Goldman, M., McCarroll, S. A. (2015). Highly Parallel Genome-wide Expression Profiling of Individual Cells Using Nanoliter Droplets. *Cell*, *161*(5), 1202-1214. doi:10.1016/j.cell.2015.05.002
- Madsen, C. D. (2021). Pancreatic cancer is suppressed by fibroblast-derived collagen I. *Cancer Cell*, *39*(4), 451-453. doi:10.1016/j.ccell.2021.02.017
- Maina, J. N. (2017). Structure and Function of the Shell and the Chorioallantoic Membrane of the Avian Egg: Embryonic Respiration. *The Biology of the Avian Respiratory System*; Springer, 219–247.
- Makanya, A. N., Dimova, I., Koller, T., Styp-Rekowska, B., & Djonov, V. (2016). Dynamics of the Developing Chick Chorioallantoic Membrane Assessed by Stereology, Allometry, Immunohistochemistry and Molecular Analysis. *PLoS One*, *11*(4), e0152821. doi:10.1371/journal.pone.0152821
- Mallya, K., Gautam, S. K., Aithal, A., Batra, S. K., & Jain, M. (2021). Modeling pancreatic cancer in mice for experimental therapeutics. *Biochim Biophys Acta Rev Cancer*, *1876*(1), 188554. doi:10.1016/j.bbcan.2021.188554
- Maneshi, P., Mason, J., Dongre, M., & Ohlund, D. (2021). Targeting Tumor-Stromal Interactions in Pancreatic Cancer: Impact of Collagens and Mechanical Traits. *Front Cell Dev Biol*, *9*, 787485. doi:10.3389/fcell.2021.787485
- Mangir, N., Raza, A., Haycock, J. W., Chapple, C., & Macneil, S. (2018). An Improved In Vivo Methodology to Visualise Tumour Induced Changes in Vasculature Using the Chick Chorionic Allantoic Membrane Assay. *In Vivo*, *32*(3), 461-472. doi:10.21873/invivo.11262
- Mapanao, A. K., Che, P. P., Sarogni, P., Sminia, P., Giovannetti, E., & Voliani, V. (2021). Tumor grafted - chick chorioallantoic membrane as an alternative model for biological cancer research and conventional/nanomaterial-based theranostics evaluation. *Expert Opin Drug Metab Toxicol*, *17*(8), 947-968. doi:10.1080/17425255.2021.1879047
- McGuigan, A., Kelly, P., Turkington, R. C., Jones, C., Coleman, H. G., & McCain, R. S. (2018). Pancreatic cancer: A review of clinical diagnosis, epidemiology, treatment and outcomes. *World J Gastroenterol*, *24*(43), 4846-4861. doi:10.3748/wjg.v24.i43.4846
- Meijlink, B., Skachkov, I., van der Steen, A. F. W., de Jong, N., & Kooiman, K. (2021). The Preparation of Chicken Ex Ovo Embryos and Chorioallantoic Membrane Vessels as In Vivo Model for Contrast-Enhanced Ultrasound Imaging and Microbubble-Mediated Drug Delivery Studies. *J Vis Exp*(168). doi:10.3791/62076
- Menini, S., Iacobini, C., Vitale, M., Pesce, C., & Pugliese, G. (2021). Diabetes and Pancreatic Cancer-A Dangerous Liaison Relying on Carbonyl Stress. *Cancers (Basel)*, *13*(2). doi:10.3390/cancers13020313
- Merckx, G., Tay, H., Lo Monaco, M., van Zandvoort, M., De Spiegelaere, W., Lambrichts, I., & Bronckaers, A. (2020). Chorioallantoic Membrane Assay as Model for Angiogenesis in Tissue Engineering: Focus on Stem Cells. *Tissue Eng Part B Rev*, *26*(6), 519-539. doi:10.1089/ten.TEB.2020.0048

- Midha, S., Chawla, S., & Garg, P. K. (2016). Modifiable and non-modifiable risk factors for pancreatic cancer: A review. *Cancer Lett*, *381*(1), 269-277. doi:10.1016/j.canlet.2016.07.022
- Miebach, L., Berner, J., & Bekeschus, S. (2022). In ovo model in cancer research and tumor immunology. *Front Immunol*, *13*, 1006064. doi:10.3389/fimmu.2022.1006064
- Miquel, M., Zhang, S., & Pilarsky, C. (2021). Pre-clinical Models of Metastasis in Pancreatic Cancer. *Front Cell Dev Biol*, *9*, 748631. doi:10.3389/fcell.2021.748631
- Moffitt, R. A., Marayati, R., Flate, E. L., Volmar, K. E., Loeza, S. G., Hoadley, K. A., Yeh, J. J. (2015). Virtual microdissection identifies distinct tumor- and stroma-specific subtypes of pancreatic ductal adenocarcinoma. *Nat Genet*, *47*(10), 1168-1178. doi:10.1038/ng.3398
- Moreno-Jimenez, I., Hulsart-Billstrom, G., Lanham, S. A., Janeczek, A. A., Kontouli, N., Kanczler, J. M., . . . Oreffo, R. O. (2016). The chorioallantoic membrane (CAM) assay for the study of human bone regeneration: a refinement animal model for tissue engineering. *Sci Rep*, *6*, 32168. doi:10.1038/srep32168
- Muckenhuber, A., Berger, A. K., Schlitter, A. M., Steiger, K., Konukiewitz, B., Trumpp, A., Weichert, W. (2018). Pancreatic Ductal Adenocarcinoma Subtyping Using the Biomarkers Hepatocyte Nuclear Factor-1A and Cytokeratin-81 Correlates with Outcome and Treatment Response. *Clin Cancer Res*, *24*(2), 351-359. doi:10.1158/1078-0432.CCR-17-2180
- Mueller, S., Engleitner, T., Maresch, R., Zukowska, M., Lange, S., Kaltenbacher, T., Rad, R. (2018). Evolutionary routes and KRAS dosage define pancreatic cancer phenotypes. *Nature*, *554*(7690), 62-68. doi:10.1038/nature25459
- Murphy, K. J., Chambers, C. R., Herrmann, D., Timpson, P., & Pereira, B. A. (2021). Dynamic Stromal Alterations Influence Tumor-Stroma Crosstalk to Promote Pancreatic Cancer and Treatment Resistance. *Cancers (Basel)*, *13*(14). doi:10.3390/cancers13143481
- Naik, M., Brahma, P., & Dixit, M. (2018). A Cost-Effective and Efficient Chick Ex-Ovo CAM Assay Protocol to Assess Angiogenesis. *Methods Protoc*, *1*(2). doi:10.3390/mps1020019
- Nowak-Sliwinska, P., Segura, T., & Iruela-Arispe, M. L. (2014). The chicken chorioallantoic membrane model in biology, medicine and bioengineering. *Angiogenesis*, *17*(4), 779-804. doi:10.1007/s10456-014-9440-7
- O'Kane, G. M., Grunwald, B. T., Jang, G. H., Masoomian, M., Picardo, S., Grant, R. C., Fischer, S. E. (2020). GATA6 Expression Distinguishes Classical and Basal-like Subtypes in Advanced Pancreatic Cancer. *Clin Cancer Res*, *26*(18), 4901-4910. doi:10.1158/1078-0432.CCR-19-3724
- Ohlund, D., Handly-Santana, A., Biffi, G., Elyada, E., Almeida, A. S., Ponz-Sarvisé, M., Tuveson, D. A. (2017). Distinct populations of inflammatory fibroblasts and myofibroblasts in pancreatic cancer. *J Exp Med*, *214*(3), 579-596. doi:10.1084/jem.20162024
- Orth, M., Metzger, P., Gerum, S., Mayerle, J., Schneider, G., Belka, C., Lauber, K. (2019). Pancreatic ductal adenocarcinoma: biological hallmarks, current status, and future perspectives of combined modality treatment approaches. *Radiat Oncol*, *14*(1), 141. doi:10.1186/s13014-019-1345-6
- Ozdemir, B. C., Pentcheva-Hoang, T., Carstens, J. L., Zheng, X., Wu, C. C., Simpson, T. R., Kalluri, R. (2014). Depletion of carcinoma-associated fibroblasts and fibrosis induces immunosuppression and accelerates pancreas cancer with reduced survival. *Cancer Cell*, *25*(6), 719-734. doi:10.1016/j.ccr.2014.04.005

- Pang, Y., Holmes, M. V., Chen, Z., & Kartsonaki, C. (2019). A review of lifestyle, metabolic risk factors, and blood-based biomarkers for early diagnosis of pancreatic ductal adenocarcinoma. *J Gastroenterol Hepatol*, *34*(2), 330-345. doi:10.1111/jgh.14576
- Parekh, S., Ziegenhain, C., Vieth, B., Enard, W., & Hellmann, I. (2016). The impact of amplification on differential expression analyses by RNA-seq. *Sci Rep*, *6*, 25533. doi:10.1038/srep25533
- Park, W., Chawla, A., & O'Reilly, E. M. (2021). Pancreatic Cancer: A Review. *JAMA*, *326*(9), 851-862. doi:10.1001/jama.2021.13027
- Pawlikowska, P., Tayoun, T., Oulhen, M., Faugeron, V., Rouffiac, V., Aberlenc, A., Farace, F. (2020). Exploitation of the chick embryo chorioallantoic membrane (CAM) as a platform for anti-metastatic drug testing. *Sci Rep*, *10*(1), 16876. doi:10.1038/s41598-020-73632-w
- Peduzzi, G., Archibugi, L., Katzke, V., Gentiluomo, M., Capurso, G., Milanetto, A. C., Campa, D. (2022). Common variability in oestrogen-related genes and pancreatic ductal adenocarcinoma risk in women. *Sci Rep*, *12*(1), 18100. doi:10.1038/s41598-022-22973-9
- Pergolini, I., Crippa, S., Pagnanelli, M., Belfiori, G., Pucci, A., Partelli, S., Falconi, M. (2019). Prognostic impact of Ki-67 proliferative index in resectable pancreatic ductal adenocarcinoma. *BJS Open*, *3*(5), 646-655. doi:10.1002/bjs5.50175
- Pfaffl, M. W. (2001). A new mathematical model for relative quantification in real-time RT-PCR. *Nucleic Acids Res*, *29*(9), e45. doi:10.1093/nar/29.9.e45
- Pham, N. A., Radulovich, N., Ibrahimov, E., Martins-Filho, S. N., Li, Q., Pintilie, M., Tsao, M. S. (2021). Patient-derived tumor xenograft and organoid models established from resected pancreatic, duodenal and biliary cancers. *Sci Rep*, *11*(1), 10619. doi:10.1038/s41598-021-90049-1
- Pion, E., Karnosky, J., Boscheck, S., Wagner, B. J., Schmidt, K. M., Brunner, S. M., Haerteis, S. (2022). 3D In Vivo Models for Translational Research on Pancreatic Cancer: The Chorioallantoic Membrane (CAM) Model. *Cancers (Basel)*, *14*(15). doi:10.3390/cancers14153733
- Pittman, M. E., Rao, R., & Hruban, R. H. (2017). Classification, Morphology, Molecular Pathogenesis, and Outcome of Premalignant Lesions of the Pancreas. *Arch Pathol Lab Med*, *141*(12), 1606-1614. doi:10.5858/arpa.2016-0426-RA
- Placencio-Hickok, V. R., Lauzon, M., Moshayedi, N., Guan, M., Kim, S., Nissen, N., Osipov, A. (2022). Hyaluronan heterogeneity in pancreatic ductal adenocarcinoma: Primary tumors compared to sites of metastasis. *Pancreatology*, *22*(1), 92-97. doi:10.1016/j.pan.2021.09.015
- Pompella, L., Tirino, G., Pappalardo, A., Caterino, M., Ventriglia, A., Nacca, V., De Vita, F. (2020). Pancreatic Cancer Molecular Classifications: From Bulk Genomics to Single Cell Analysis. *Int J Mol Sci*, *21*(8). doi:10.3390/ijms21082814
- Power, E. A., Fernandez-Torres, J., Zhang, L., Yaun, R., Lucien, F., & Daniels, D. J. (2022). Chorioallantoic membrane (CAM) assay to study treatment effects in diffuse intrinsic pontine glioma. *PLoS One*, *17*(2), e0263822. doi:10.1371/journal.pone.0263822
- Puleo, F., Nicolle, R., Blum, Y., Cros, J., Marisa, L., Demetter, P., Marechal, R. (2018). Stratification of Pancreatic Ductal Adenocarcinomas Based on Tumor and Microenvironment Features. *Gastroenterology*, *155*(6), 1999-2013 e1993. doi:10.1053/j.gastro.2018.08.033

- Rahib, L., Wehner, M. R., Matrisian, L. M., & Nead, K. T. (2021). Estimated Projection of US Cancer Incidence and Death to 2040. *JAMA Netw Open*, 4(4), e214708. doi:10.1001/jamanetworkopen.2021.4708
- Randriamanantsoa, S., Papargyriou, A., Maurer, H. C., Peschke, K., Schuster, M., Zecchin, G., Bausch, A. R. (2022). Spatiotemporal dynamics of self-organized branching in pancreas-derived organoids. *Nat Commun*, 13(1), 5219. doi:10.1038/s41467-022-32806-y
- Ranjan, R. A., Muenzner, J. K., Kunze, P., Geppert, C. I., Ruebner, M., Huebner, H., Schneider-Stock, R. (2023). The Chorioallantoic Membrane Xenograft Assay as a Reliable Model for Investigating the Biology of Breast Cancer. *Cancers (Basel)*, 15(6). doi:10.3390/cancers15061704
- Rashid, N. U., Peng, X. L., Jin, C., Moffitt, R. A., Volmar, K. E., Belt, B. A., Yeh, J. J. (2020). Purity Independent Subtyping of Tumors (PurIST), A Clinically Robust, Single-sample Classifier for Tumor Subtyping in Pancreatic Cancer. *Clin Cancer Res*, 26(1), 82-92. doi:10.1158/1078-0432.CCR-19-1467
- Rhim, A. D., Oberstein, P. E., Thomas, D. H., Mirek, E. T., Palermo, C. F., Sastra, S. A., Stanger, B. Z. (2014). Stromal elements act to restrain, rather than support, pancreatic ductal adenocarcinoma. *Cancer Cell*, 25(6), 735-747. doi:10.1016/j.ccr.2014.04.021
- Ribatti, D. (2016). The chick embryo chorioallantoic membrane (CAM). A multifaceted experimental model. *Mech Dev*, 141, 70-77. doi:10.1016/j.mod.2016.05.003
- Ribatti, D. (2021). The CAM assay in the study of the metastatic process. *Exp Cell Res*, 400(2), 112510. doi:10.1016/j.yexcr.2021.112510
- Ribatti, D., Tamma, R., & Annese, T. (2021). Chorioallantoic membrane vascularization. A meta-analysis. *Exp Cell Res*, 405(2), 112716. doi:10.1016/j.yexcr.2021.112716
- Romero-Calvo, I., Weber, C. R., Ray, M., Brown, M., Kirby, K., Nandi, R. K., White, K. P. (2019). Human Organoids Share Structural and Genetic Features with Primary Pancreatic Adenocarcinoma Tumors. *Mol Cancer Res*, 17(1), 70-83. doi:10.1158/1541-7786.MCR-18-0531
- Rovithi, M., Avan, A., Funel, N., Leon, L. G., Gomez, V. E., Wurdinger, T., Giovannetti, E. (2017). Development of bioluminescent chick chorioallantoic membrane (CAM) models for primary pancreatic cancer cells: a platform for drug testing. *Sci Rep*, 7, 44686. doi:10.1038/srep44686
- Rupp, T., Legrand, C., Hunault, M., Genest, L., Babin, D., Froget, G., & Castagne, V. (2022). A Face-To-Face Comparison of Tumor Chicken Chorioallantoic Membrane (TCAM) In Ovo with Murine Models for Early Evaluation of Cancer Therapy and Early Drug Toxicity. *Cancers (Basel)*, 14(14). doi:10.3390/cancers14143548
- Ruud, K. F., Hiscox, W. C., Yu, I., Chen, R. K., & Li, W. (2020). Distinct phenotypes of cancer cells on tissue matrix gel. *Breast Cancer Res*, 22(1), 82. doi:10.1186/s13058-020-01321-7
- Sarogni, P., Mapanao, A. K., Gonnelli, A., Ermini, M. L., Marchetti, S., Kusmic, C., Voliani, V. (2022). Chorioallantoic membrane tumor models highlight the effects of cisplatin compounds in oral carcinoma treatment. *iScience*, 25(3), 103980. doi:10.1016/j.isci.2022.103980
- Schneider, T., Osl, F., Friess, T., Stockinger, H., & Scheuer, W. V. (2002). Quantification of human Alu sequences by real-time PCR--an improved method to measure therapeutic efficacy of anti-metastatic drugs in human xenotransplants. *Clin Exp Metastasis*, 19(7), 571-582. doi:10.1023/a:1020992411420

- Sereti, E., Papapostolou, I., & Dimas, K. (2023). Pancreatic Cancer Organoids: An Emerging Platform for Precision Medicine? *Biomedicines*, *11*(3). doi:10.3390/biomedicines11030890
- Shinkawa, T., Ohuchida, K., & Nakamura, M. (2022). Heterogeneity of Cancer-Associated Fibroblasts and the Tumor Immune Microenvironment in Pancreatic Cancer. *Cancers (Basel)*, *14*(16). doi:10.3390/cancers14163994
- Simoes, P. K., Olson, S. H., Saldia, A., & Kurtz, R. C. (2017). Epidemiology of pancreatic adenocarcinoma. *Chin Clin Oncol*, *6*(3), 24. doi:10.21037/cco.2017.06.32
- Sperb, N., Tsesmelis, M., & Wirth, T. (2020). Crosstalk between Tumor and Stromal Cells in Pancreatic Ductal Adenocarcinoma. *Int J Mol Sci*, *21*(15). doi:10.3390/ijms21155486
- Storz, P. (2017). Acinar cell plasticity and development of pancreatic ductal adenocarcinoma. *Nat Rev Gastroenterol Hepatol*, *14*(5), 296-304. doi:10.1038/nrgastro.2017.12
- Su, H., Yang, F., Fu, R., Trinh, B., Sun, N., Liu, J., Karin, M. (2022). Collagenolysis-dependent DDR1 signalling dictates pancreatic cancer outcome. *Nature*, *610*(7931), 366-372. doi:10.1038/s41586-022-05169-z
- Suri, R., Zimmerman, J. W., & Burkhart, R. A. (2020). Modeling human pancreatic ductal adenocarcinoma for translational research: current options, challenges, and prospective directions. *Ann Pancreat Cancer*, *3*. doi:10.21037/apc-20-29
- Tahkola, K., Ahtiainen, M., Mecklin, J. P., Kellokumpu, I., Laukkarinen, J., Tammi, M., Bohm, J. (2021). Stromal hyaluronan accumulation is associated with low immune response and poor prognosis in pancreatic cancer. *Sci Rep*, *11*(1), 12216. doi:10.1038/s41598-021-91796-x
- Takikawa, T., Kikuta, K., Hamada, S., Kume, K., Miura, S., Yoshida, N., Masamune, A. (2022). Clinical features and prognostic impact of asymptomatic pancreatic cancer. *Sci Rep*, *12*(1), 4262. doi:10.1038/s41598-022-08083-6
- Tanaka, R., Kageyama, K., Kimura, K., Eguchi, S., Tauchi, J., Shinkawa, H., Ohira, M. (2020). Establishment of a Liver Transplant Patient-derived Tumor Xenograft (PDX) Model Using Cryopreserved Pancreatic Ductal Adenocarcinoma. *Anticancer Res*, *40*(5), 2637-2644. doi:10.21873/anticancerres.14234
- Tiriach, H., Belleau, P., Engle, D. D., Plenker, D., Deschenes, A., Somerville, T. D. D., Tuveson, D. A. (2018). Organoid Profiling Identifies Common Responders to Chemotherapy in Pancreatic Cancer. *Cancer Discov*, *8*(9), 1112-1129. doi:10.1158/2159-8290.CD-18-0349
- Torres, C., & Grippo, P. J. (2018). Pancreatic cancer subtypes: a roadmap for precision medicine. *Ann Med*, *50*(4), 277-287. doi:10.1080/07853890.2018.1453168
- Truong, L. H., & Pauklin, S. (2021). Pancreatic Cancer Microenvironment and Cellular Composition: Current Understandings and Therapeutic Approaches. *Cancers (Basel)*, *13*(19). doi:10.3390/cancers13195028
- Vaish, U., Jain, T., Are, A. C., & Dudeja, V. (2021). Cancer-Associated Fibroblasts in Pancreatic Ductal Adenocarcinoma: An Update on Heterogeneity and Therapeutic Targeting. *Int J Mol Sci*, *22*(24). doi:10.3390/ijms222413408

- Vlachogiannis, G., Hedayat, S., Vatsiou, A., Jamin, Y., Fernandez-Mateos, J., Khan, K., Valeri, N. (2018). Patient-derived organoids model treatment response of metastatic gastrointestinal cancers. *Science*, 359(6378), 920-926. doi:10.1126/science.aao2774
- von Ahrens, D., Bhagat, T. D., Nagrath, D., Maitra, A., & Verma, A. (2017). The role of stromal cancer-associated fibroblasts in pancreatic cancer. *J Hematol Oncol*, 10(1), 76. doi:10.1186/s13045-017-0448-5
- Waddell, N., Pajic, M., Patch, A. M., Chang, D. K., Kassahn, K. S., Bailey, P., Grimmond, S. M. (2015). Whole genomes redefine the mutational landscape of pancreatic cancer. *Nature*, 518(7540), 495-501. doi:10.1038/nature14169
- Wahbi, W., Naakka, E., Tuomainen, K., Suleymanova, I., Arpalahiti, A., Miinalainen, I., Salo, T. (2020). The critical effects of matrices on cultured carcinoma cells: Human tumor-derived matrix promotes cell invasive properties. *Exp Cell Res*, 389(1), 111885. doi:10.1016/j.yexcr.2020.111885
- Wandmacher, A. M., Mehdorn, A. S., & Sebens, S. (2021). The Heterogeneity of the Tumor Microenvironment as Essential Determinant of Development, Progression and Therapy Response of Pancreatic Cancer. *Cancers (Basel)*, 13(19). doi:10.3390/cancers13194932
- Wang, C. F., & Shi, X. J. (2019). Generation and application of patient-derived xenograft models in pancreatic cancer research. *Chin Med J (Engl)*, 132(22), 2729-2736. doi:10.1097/CM9.0000000000000524
- Wang, E., Xiang, K., Zhang, Y., & Wang, X.-F. (2022). Patient-derived organoids (PDOs) and PDO-derived xenografts (PDOXs): New opportunities in establishing faithful pre-clinical cancer models. *Journal of the National Cancer Center*, 2(4), 263-276. doi:10.1016/j.jncc.2022.10.001
- Wang, K., & He, H. (2020). Pancreatic Tumor Microenvironment. *Adv Exp Med Biol*, 1296, 243-257. doi:10.1007/978-3-030-59038-3_15
- Waschkies, C. F., Pffnner, F. K., Heuberger, D. M., Schneider, M. A., Tian, Y., Wolint, P., Buschmann, J. (2020). Tumor grafts grown on the chicken chorioallantoic membrane are distinctively characterized by MRI under functional gas challenge. *Sci Rep*, 10(1), 7505. doi:10.1038/s41598-020-64290-z
- Welm, B. E., Vaklavas, C., & Welm, A. L. (2021). Toward improved models of human cancer. *APL Bioeng*, 5(1), 010901. doi:10.1063/5.0030534
- Xu, H., Jiao, D., Liu, A., & Wu, K. (2022). Tumor organoids: applications in cancer modeling and potentials in precision medicine. *J Hematol Oncol*, 15(1), 58. doi:10.1186/s13045-022-01278-4
- Yamamoto, A., Doak, A. E., & Cheung, K. J. (2023). Orchestration of Collective Migration and Metastasis by Tumor Cell Clusters. *Annu Rev Pathol*, 18, 231-256. doi:10.1146/annurev-pathmechdis-031521-023557
- Yang, Y. M., Nouredin, M., Liu, C., Ohashi, K., Kim, S. Y., Ramnath, D., Seki, E. (2019). Hyaluronan synthase 2-mediated hyaluronan production mediates Notch1 activation and liver fibrosis. *Sci Transl Med*, 11(496). doi:10.1126/scitranslmed.aat9284
- Yao, W., Maitra, A., & Ying, H. (2020). Recent insights into the biology of pancreatic cancer. *EBioMedicine*, 53, 102655. doi:10.1016/j.ebiom.2020.102655

- Yu, Y., Yang, G., Huang, H., Fu, Z., Cao, Z., Zheng, L., Zhang, T. (2021). Preclinical models of pancreatic ductal adenocarcinoma: challenges and opportunities in the era of precision medicine. *J Exp Clin Cancer Res*, 40(1), 8. doi:10.1186/s13046-020-01787-5
- Zhang, H., Zhang, S. B., Sun, W., Yang, S., Zhang, M., Wang, W., Zhang, L. (2009). B1 sequence-based real-time quantitative PCR: a sensitive method for direct measurement of mouse plasma DNA levels after gamma irradiation. *Int J Radiat Oncol Biol Phys*, 74(5), 1592-1599. doi:10.1016/j.ijrobp.2009.03.009
- Zhang, S., Wang, C., Huang, H., Jiang, Q., Zhao, D., Tian, Y., Chen, Y. (2017). Effects of alcohol drinking and smoking on pancreatic ductal adenocarcinoma mortality: A retrospective cohort study consisting of 1783 patients. *Sci Rep*, 7(1), 9572. doi:10.1038/s41598-017-08794-1
- Zhang, T., Ren, Y., Yang, P., Wang, J., & Zhou, H. (2022). Cancer-associated fibroblasts in pancreatic ductal adenocarcinoma. *Cell Death Dis*, 13(10), 897. doi:10.1038/s41419-022-05351-1
- Zhou, X., Hu, K., Bailey, P., Springfield, C., Roth, S., Kurilov, R., Neoptolemos, J. P. (2021). Clinical Impact of Molecular Subtyping of Pancreatic Cancer. *Front Cell Dev Biol*, 9, 743908. doi:10.3389/fcell.2021.743908